Boundary Layer Momentum Budgets as Determined from a Single Scanning Doppler Radar

by
Brad W. Orr

Department of Atmospheric Science
Colorado State University
Fort Collins, Colorado

Colorado
State
University

Department of
Atmospheric Science

Paper No. 477

BOUNDARY LAYER MOMENTUM BUDGETS AS DETERMINED FROM A SINGLE SCANNING DOPPLER RADAR

by

Brad W. Orr

Department of Atmospheric Science
Colorado State University
Fort Collins, CO 80523

This research was supported by the Wave Propagation Laboratory,
NOAA, Boulder, CO, and the National Science Foundation
under Grant No. ATM-8711649

Atmospheric Science Paper No. 477

February 1991

ABSTRACT

BOUNDARY LAYER MOMENTUM BUDGETS AS DETERMINED FROM A SINGLE SCANNING DOPPLER RADAR

The Velocity Azimuth Display (VAD) technique is extended to third-order turbulent velocity statistics. By applying this extended VAD technique to a single scanning Doppler radar a solution for the horizontal turbulent momentum flux budget is obtained. All terms excluding the buoyancy, pressure and eddy dissipation terms can be solved for directly. High resolution measurements of the momentum flux budget can then be studied in both space and time. Specifically the third-order turbulent transport term can be examined.

Three data sets characterized by hot, clear summertime planetary boundary layers (PBL) are analyzed using this extended VAD technique. These data show turbulent transport to be very significant throughout the day and night. Daytime values were observed to be of the same order or slightly larger than shear production. At night shear production dominated but turbulent transport was still of significant magnitude. Other notable features were the high degree of variability in all turbulent quantities in both space and time. The large contribution from turbulent transport and the high degree of nonstationarity in the turbulence field are in contrast to most other field measurements. Brief explanations are given for these differences. Comparisons with computer modeling studies are also made which agree more closely with the radar analysis than did the field studies.

ACKNOWLEDGEMENTS

Foremost in appreciation for his guidance and insight is Dr. A.S. Frisch. His enthusiasm in the area of atmospheric turbulence was a primary impetus for this research. Special thanks go to R.A. Kropfli and B.E. Martner who made many helpful suggestions and allocated the time to complete this work. J.S. Gibson, E. Ash and L. Church all provided valuable guidance during the software development process. My committee members were very helpful and accommodating with respect to the time constraints under which this study was completed. Also my wife and children for their support and endurance throughout this research effort. WPL's participation in the North Dakota Thunderstorm Project was sponsored by the NOAA Federal/State Cooperative Program in Atmospheric Modification Research. Funding for WPL's participation in the Cloud Chemistry Cloud Physics Organization project was provided by the Electric Power Research Institute through a subcontract with Battelle Pacific Northwest Laboratories.

TABLE OF CONTENTS

LIST OF FIGURES

LIST OF TABLES

Number Page

1. INTRODUCTION

The Planetary Boundary Layer (PBL) has been defined as that portion of the atmosphere which is directly influenced by surface forcings and responds to these forcings on a time scale of one hour or less (Stull, 1988). The PBL is therefore at the lowest levels of the atmosphere, typically the lowest kilometer, and is characterized by turbulent transport. Knowledge of the generation, dissipation and transport of turbulent processes are important to the understanding the structure and evolution of the PBL which, in turn, has implications to many disciplines including air pollution monitoring, engineering, agriculture, and climatological studies. An idealized daytime, convective PBL is illustrated in Fig. 1.

Three distinct layers can be discriminated within the PBL based on the profiles in Fig. 1. The layer immediately adjacent to the surface is referred to as the surface layer. This layer is characterized by strong gradients in wind, temperature and other passive quantities. Potential temperature (θ) is super- adiabatic due to strong surface heating. Wind speed profiles have a strong positive slope as a result of surface frictional effects. Water vapor and pollutant concentrations have strong negative gradients since their source is the surface under nonadvective conditions. Turbulence transfer within the surface layer has been well documented due to the ease of obtaining measurements within this layer whose depth is typically tens to hundreds of meters.

The central portion of the PBL is referred to as the mixed layer and as the name implies is characterized by strong turbulent mixing. Profiles of mean meteorological variables and atmospheric constituents are essentially linear

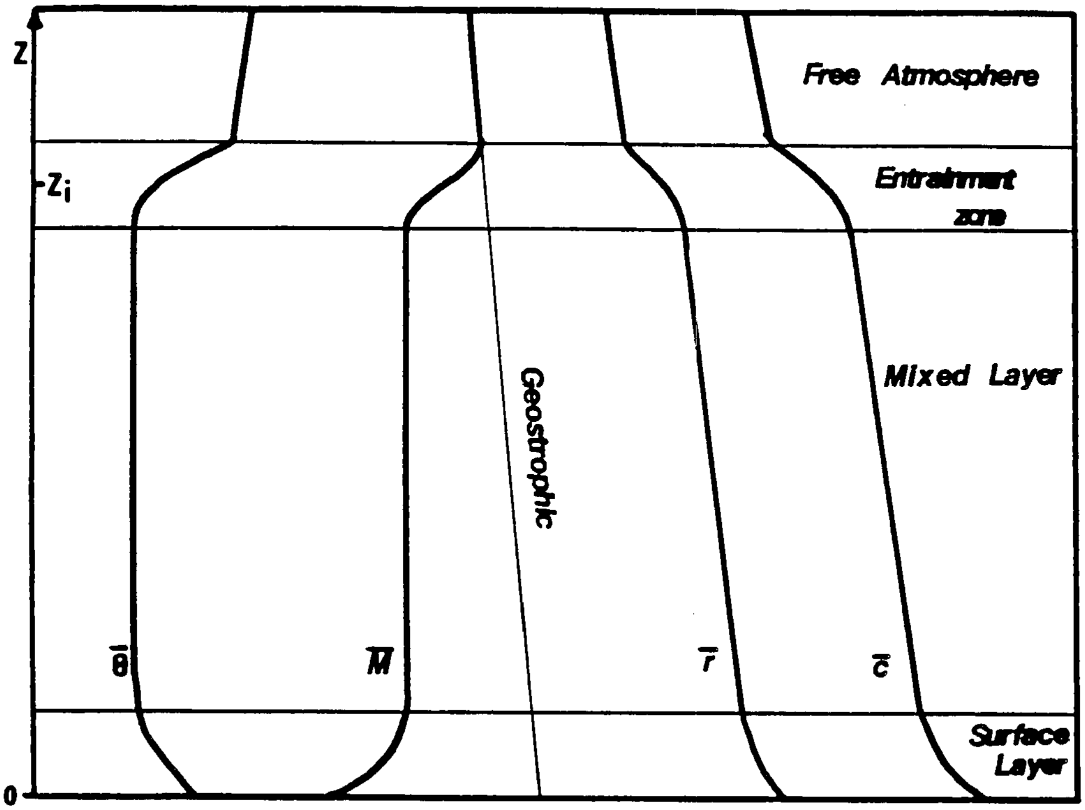

Fig. 1. Characteristic mean PBL profiles of potential temperature $\bar{\theta}$, mean wind speed $\overline{M}$, mixing ratio $\bar{r}$ and pollutant concentration $\bar{c}$ (after Stull, 1988).

throughout the mixed layer as a result of this mixing. Passive constituents such as water vapor and pollutants have a slightly negative slope indicating a net upward flux of high surface concentrations being entrained with relatively "clean" and dry upper atmosphere air. The mixed layer begins at the top of the surface layer and typically constitutes 50 to 80 percent of the PBL.

Separating the mixed layer from the free atmosphere (free atmosphere implying essentially "free" from surface influences) is the entrainment zone. This is the layer through which free atmosphere air is entrained into the mixed layer. Virtual potential temperature increases across this zone indicating a capping inversion. This inversion is used as a measure of the top of the PBL, denoted by z_i, which is typically about one kilometer above the surface. Wind speeds increase across this layer from their frictionally-slowed subgeostrophic values to geostrophic speeds. Passive constituents show a strong decrease in concentration.

Although there have been a number of field experiments for determining the structure and dynamics of the mixed layer and entrainment zone (Minnesota, Kaimal et. al. 1976; AMTEX, Lenchow et. al. 1980; MASEX, Atlas et. al. 1986; PHOENIX, Kropfli and Hildebrand 1980; BLX83, Stull and Eloranta 1984) the number is considerably less than those concerned with the surface layer. This is due to the difficulty and expense in obtaining detailed measurements over the entire depth of the PBL. Most data on the PBL have been obtained using aircraft or tethered balloons. Both of these measurement systems have some type of compromise in data resolution, either spatial or temporal. Also most field studies to date have only been concerned with the well-mixed, undisturbed, non-baroclinic PBL. On a global scale energy transfer under baroclinic conditions is extremely important. Under such conditions energy transfer budgets can be significantly different than in more barotropic situations.

Large-eddy simulations (LES) are beginning to play an important part in the understanding of turbulent processes within the PBL, primarily because of their high resolution and ability to extend current turbulence knowledge to situations for which there is little or no observational data. These models can also test the importance of various mechanisms (production, dissipation and transport) under a variety of atmospheric situations. Most boundary layer models now incorporate third-order closure schemes which allow them to fully solve most PBL turbulence budgets. The representativeness of these higher-order closures is difficult to estimate however since as mentioned above there is rather sparse atmospheric data on which they are based. Therefore one of the main advantages of a LES, namely the ability to obtain information about the PBL in situations where there is little observational data, is based on this same lack of information.

The above arguments point toward the need for additional high resolution atmospheric measurements, especially of higher-ordered turbulence quantities, throughout the depth of the boundary layer under a variety of meteorological conditions. The Velocity Azimuth Display (VAD) technique demonstrated by Browning and Wexler (1968) provides such a method utilizing remote sensors. They illustrate how a scanning Doppler radar can be used to derive first moment statistics about the mean wind field. The radar is scanned about a vertical axis at a constant elevation angle, the so called VAD scan. The geometry of this type of scan is illustrated in Fig. 2. A scan refers to a complete 360 degree revolution of the radar antenna.

By decomposing the radial velocities (V_r) into a Fourier series Browning and Wexler (1968) obtained expressions describing the mean wind components, two-dimensional horizontal divergence, stretching deformation and shearing deformation. Wilson (1970) extended this to include second moment quantities such as the covariance terms $\overline{u'w'}$, $\overline{v'w'}$, and $\overline{u'v'}$. A typical VAD scan showing

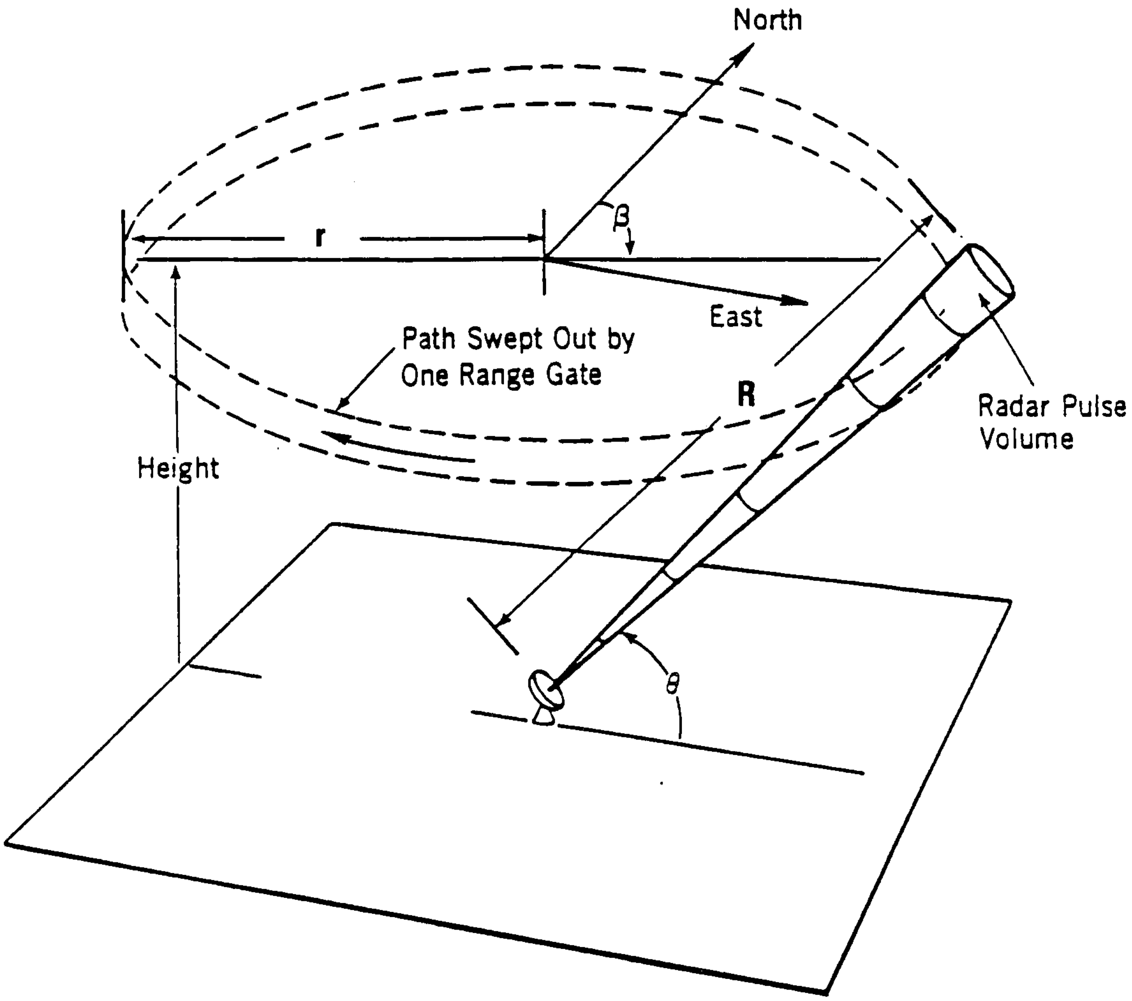

Fig. 2. Scanning geometry for the velocity azimuth display technique.

the variation due to turbulent fluctuations about the mean wind is shown in Fig. 3. Since these fluctuations are too large to be errors in the velocity estimates they are attributed to turbulence on scales less than $2r$, where $r = z cot\theta$ is the radius of the circle swept out at a given range during one scan and z is the altitude of interest. Kropfli (1986) shows how turbulence on scales greater than $2r$ can be obtained by comparing fluctuations of the scan to scan wind components about some temporal mean which is obtained by averaging over multiple VAD scans. Frisch et. al. (1989) used this technique to obtain estimates of the vertical flux of turbulence kinetic energy from a radar scanning at 50.8° elevation. Eberhard et. at. (1989) have also applied this technique to a scanning Doppler Lidar.

The above applications of the VAD technique for determining turbulence statistics use the procedure set forth by Wilson (1970) of performing separate integrations over the four quadrants of the VAD scan. This method requires the assumption that the stresses and variances around the scanning circle are horizontally homogeneous. Frisch (1990) shows how one can expand the turbulence stress in a Taylor series and compute the stress for the general case of non-homogeneity in a method analogous to that used by Browning and Wexler (1968) for the mean wind. This can then be equated with a Fourier expansion of the variance of the Doppler radial velocity.

In this study the VAD technique will be extended to examine third moment turbulence quantities following the procedure set forth by Frisch (1990) to solve for the turbulent stress and velocity variances. Wyngaard (1983) showed that even for a simplified momentum flux budget in strong shear or baroclinic conditions, terms involving shear production and turbulent transport must be retained (see equations (2) and (3)). By extending the VAD technique to third moment quantities, all terms in this simplified momentum flux budget equation, excluding the pressure, buoyancy, and eddy dissipation terms, can be determined. The

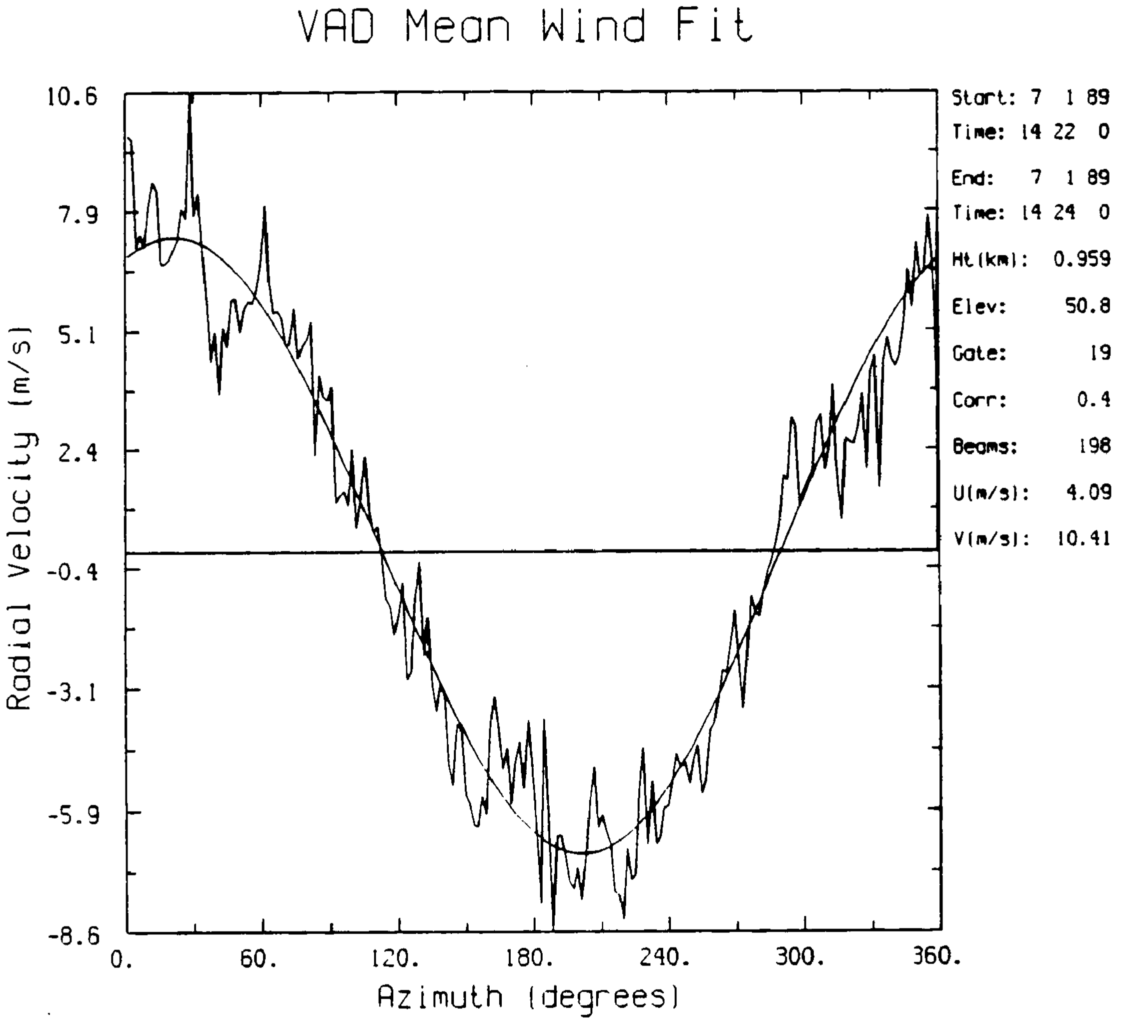

Fig. 3. Example of radar radial velocities sampled at one elevation angle as a function of azimuth at one height (one range gate) for the VAD method. Smooth curve is the best- fit from the mean wind analysis.

relative magnitudes of these derived turbulence profiles can then be compared to existing data sets, thereby obtaining a measure of the accuracy of this technique.

The VAD data used for this study was obtained by one of the National Oceanic and Atmospheric Administration's (NOAA) Wave Propagation Laboratory's (WPL) X-band radars. Three data sets will be used, two from the North Dakota Thunderstorm Project (NDTP) from the summer of 1989 and one from the summer of 1988 obtained during the Cloud Chemistry Cloud Physics Organization (3CPO, Martner et. al. 1988) project. All three data sets were characterized by hot, clear summer days with moderate to strong winds which changed throughout the data periods. These data should serve to establish this extended VAD technique as a viable method for obtaining detailed, high-ordered turbulence measurements throughout the depth of the PBL.

2. THEORETICAL BACKGROUND

2a. Momentum Budget

The complete turbulent stress budget equation in tensor notation is:

$$\frac{\partial(\overline{u'_i u'_k})}{\partial t} + \bar{u}_j \frac{\partial(\overline{u'_i u'_k})}{\partial x_j} = - \overline{u'_i u'_j} \frac{\partial \bar{u}_k}{\partial x_j} - \overline{u'_k u'_j} \frac{\partial \bar{u}_i}{\partial x_j} - \frac{\partial(\overline{u'_i u'_j u'_k})}{\partial x_j}$$

$$+ \left[\frac{g}{\bar{\theta}_v}\right] \left(\delta_{k3} \overline{u'_i \theta'_v} + \delta_{i3} \overline{u'_k \theta'_v}\right) + f_c \left(\varepsilon_{kj3} \overline{u'_j u'_i} + \varepsilon_{ij3} \overline{u'_j u'_k}\right)$$

$$+ \overline{\frac{p'}{\bar{\rho}} \left(\frac{\partial u'_i}{\partial x_k} + \frac{\partial u'_k}{\partial x_i}\right)} + \nu \frac{\partial^2(\overline{u'_i u'_k})}{\partial {x_j}^2} - 2\nu \frac{\overline{\partial u'_i \partial u'_k}}{\partial {x_j}^2} \qquad (1)$$

where the primes indicate a deviation from some mean and the overbar represents an ensemble average. A detailed derivation of this and other equations in this chapter can be found in appendix A.

The time scale for most PBL processes is on the order of one hour or less and therefore the Coriolis term can be neglected. The second to last term on the right hand side represents molecular diffusion and is also much smaller than the other terms. The last term is the viscous dissipation term and is usually written as $2\varepsilon_{u_i v_i}$.

The terms on the left hand side of equation (1) represent local storage and advection by the mean wind. The first two terms on the right hand side represent turbulent transport due to gradients in the mean wind components. The next term represents turbulent transport of eddy stress. The second line of equation (1) contains the buoyancy and Coriolis terms. Finally the last line represents pressure redistribution, molecular diffusion and eddy dissipation respectively. A common assumption for simplifying this equation is that of horizontal homogeneity. This assumption effectively eliminates all terms with horizontal gradients. Although there are horizontal discontinuities throughout the depth of the PBL, if the horizontal scales of the radar measurements are small enough this assumption should be valid. The horizontal measurement scale in the data for this study will be limited by the diameter of the VAD scan (Fig. 2). This scale will be a maximum at low elevation angles which for these data is 35.3°. At this angle, assuming a maximum z_i of 2.0 km, the diameter of the VAD scan should be less than 7.0 km. Making the above simplifications and expanding equation (1) for the fluxes of $\overline{u'w'}$(i=1, k=3) and $\overline{v'w'}$(i=2, k=3) gives the following two equations:

$$\frac{\partial \overline{u'w'}}{\partial t} + \bar{w}\frac{\partial \overline{u'w'}}{\partial z} = -\overline{u'w'}\frac{\partial \bar{w}}{\partial z} - \overline{w'w'}\frac{\partial \bar{u}}{\partial z} - \frac{\partial(\overline{u'w'w'})}{\partial z} + \left[\frac{g}{\bar{\theta}_v}\right](\overline{u'\theta'_v}) - \overline{\frac{u'}{\bar{\rho}}\frac{\partial p'}{\partial z}} - 2\varepsilon_{uw} \tag{2}$$

$$\frac{\partial \overline{v'w'}}{\partial t} + \bar{w}\frac{\partial \overline{v'w'}}{\partial z} = -\overline{v'w'}\frac{\partial \bar{w}}{\partial z} - \overline{w'w'}\frac{\partial \bar{v}}{\partial z} - \frac{\partial(\overline{v'w'w'})}{\partial z} + \left[\frac{g}{\bar{\theta}_v}\right](\overline{v'\theta'_v}) - \overline{\frac{v'}{\bar{\rho}}\frac{\partial p'}{\partial z}} - 2\varepsilon_{vw} \tag{3}$$

These equations are similar to those shown by Wyngaard (1983) to be applicable to a baroclinic boundary layer. The two terms on the righthand side of equations (2) and (3), local storage and transport due to mean subsidence, are usually considered much smaller than the other terms. However since these terms are easily computed they will be retained as a matter of completeness.

2b. VAD Technique

The method outlined by Frisch (1990) of performing a Fourier analysis on an entire VAD scan will be used for this analysis. This is in contrast to the method used by others (Wilson (1970), Kropfli (1986), Eberhard et. al. (1989)) which combines a series of four integrals, one for each quadrant of a VAD scan, for computing turbulence statistics. Numerically the results should be equivalent. The method of Frisch (1990) was chosen because it is intuitively a more straightforward approach and can easily be extended to higher-ordered statistics. The following paragraphs outline the methodology and equations applicable for this approach.

The Doppler radial velocity (V_r) can be written in terms of the three components u(east), v(north) and w(vertical).

$$V_r = usin\beta cos\theta + vcos\beta cos\theta + wsin\theta$$

Approaching velocities are considered negative. The velocity components can be expanded in terms of a mean component and gradients about that mean to give

$$u = u_o + x\frac{\partial u}{\partial x} + y\frac{\partial u}{\partial y} \tag{4}$$

$$v = v_o + x\frac{\partial v}{\partial x} + y\frac{\partial v}{\partial y} \tag{5}$$

where $x = rsin\beta$, $y = rcos\beta$, β is azimuth and r is the radius of the circle swept out by a given range gate (see Fig. 2). Making these substitutions gives:

$$V_r = \left[u_o sin\beta + rsin^2\beta\frac{\partial u}{\partial x} + rcos\beta sin\beta\frac{\partial u}{\partial y}\right]cos\theta$$

$$+ \left[v_o cos\beta + rsin\beta cos\beta\frac{\partial v}{\partial x} + rcos^2\beta\frac{\partial v}{\partial y}\right]cos\theta + w_o sin\theta \tag{6}$$

The terms involving beta can be written in terms of Euler expressions. This makes the separation of the various harmonic terms straightforward and gives the above equation as

$$V_r = \left[-\frac{iu_o}{2}\left(e^{i\beta} - e^{-i\beta}\right) - \frac{r}{4}\frac{\partial u}{\partial x}\left(e^{2i\beta} + e^{-2i\beta} - 2\right)\right] cos\theta$$

$$\left[-\frac{ir}{4}\frac{\partial u}{\partial y}\left(e^{2i\beta} - e^{-2i\beta}\right) + \frac{v_o}{2}\left(e^{i\beta} + e^{-i\beta}\right) - \frac{ir}{4}\frac{\partial v}{\partial x}\left(e^{2i\beta} - e^{-2i\beta}\right)\right] cos\theta$$

$$+ \frac{r}{4}\frac{\partial v}{\partial y}\left(e^{2i\beta} + e^{-2i\beta} + 2\right) cos\theta + w_o sin\theta \tag{7}$$

Performing a least-squares analysis of the radar V_r data (or equivalently a discrete Fourier analysis) using the complex form

$$\sum_{n=0}^{N} A_n e^{in\beta}$$

produces terms which can be equated to the righthand side of the above equation. Separating terms for $e^{in\beta}$ with n=0, 1, and 2in (7) and equating them with the least-squares analysis of V_r gives the following coefficients for the mean wind analysis.

$$A_0 = \tfrac{r}{2}\left(\tfrac{\partial u}{\partial x} + \tfrac{\partial v}{\partial y}\right) cos\theta + w_o sin\theta$$
$$A_1 = \tfrac{v_o}{2} cos\theta$$
$$A_{1i} = -\tfrac{u_o}{2} cos\theta$$
$$A_2 = \tfrac{r}{4}\left(\tfrac{\partial v}{\partial y} - \tfrac{\partial u}{\partial x}\right) cos\theta$$
$$A_{2i} = -\tfrac{r}{4}\left(\tfrac{\partial v}{\partial x} + \tfrac{\partial u}{\partial y}\right) cos\theta$$

The subscripts indicate the harmonic from which they were derived. A subscript without an i indicates the real part of the coefficient and a subscript with an i the imaginary part. These are equivalent to the expressions obtained by Browning and Wexler (1968).

The variance of the radial velocity can be written as

$$\overline{(V_r - \bar{V}_r)^2} = (u' sin\beta cos\theta + v' cos\beta cos\theta + w' sin\theta)^2$$

where the prime indicates a deviation about some mean which can be obtained from one or more VAD scans. Expanding this gives:

$$\overline{(V_r\ -\ \bar{V}_r)^2}\ =\ \overline{u'^2}cos^2\theta sin^2\beta\ +\ \overline{v'^2}cos^2\theta cos^2\beta\ +\ \overline{w'^2}sin^2\theta$$

$$+\ 2\overline{u'v'}cos^2\theta cos\beta sin\beta\ +\ 2\overline{u'w'}cos\theta sin\theta sin\beta\ +\ 2\overline{v'w'}sin\theta cos\theta cos\beta$$

This expression is also the second moment expansion of the radial velocity. Rewriting the sine and cosine terms gives the expression

$$\overline{(V_r\ -\ \bar{V}_r)^2}\ =\ \overline{u'^2}cos^2\theta sin^2\beta\ +\ \overline{v'^2}cos^2\theta cos^2\beta\ +\ \overline{w'^2}sin^2\theta$$

$$+\ \overline{u'v'}cos^2\theta sin2\beta\ +\ \overline{u'w'}sin2\theta sin\beta\ +\ \overline{v'w'}sin2\theta cos\beta$$

Writing this in terms of Euler expressions gives the final expression

$$\overline{(V_r\ -\ \bar{V}_r)^2}\ =\ \overline{u'^2}cos^2\theta\left[-\frac{1}{4}\left(e^{2i\beta}\ +\ e^{-2i\beta}\ -\ 2\right)\right]$$

$$+\ \overline{v'^2}cos^2\theta\left[\frac{1}{4}\left(e^{2i\beta}\ +\ e^{-2i\beta}\ +\ 2\right)\right]\ +\ \overline{w'^2}sin^2\theta$$

$$+\ 2\overline{u'v'}cos^2\theta\left[-\frac{i}{4}\left(e^{2i\beta}\ -\ e^{-2i\beta}\right)\right]\ +\ \overline{u'w'}sin2\theta\left[-\frac{i}{2}\left(e^{i\beta}\ -\ e^{-i\beta}\right)\right]$$

$$+\ \overline{v'w'}sin2\theta\left[\frac{1}{2}\left(e^{i\beta}\ +\ e^{-i\beta}\right)\right] \tag{8}$$

Performing a similar least-squares analysis of the radar data as was done for the mean wind only now using $\overline{V_r'^2}$(the second moment of the radial velocity or the variance) and equating this with (8) gives the harmonic coefficients of $e^{in\beta}$ for n=0, 1 and 2.

$$\begin{aligned}
A_0 &= \tfrac{1}{2}\overline{u'^2}cos^2\theta\ +\ \tfrac{1}{2}\overline{v'^2}cos^2\theta\ +\ \overline{w'^2}sin^2\theta \\
A_1 &= \overline{v'w'}sin\theta cos\theta \\
A_{1i} &= -\overline{u'w'}sin\theta cos\theta \\
A_2 &= \tfrac{1}{4}cos^2\theta\left(\overline{v'^2}\ -\ \overline{u'^2}\right) \\
A_{2i} &= -\tfrac{1}{2}\overline{u'v'}cos^2\theta
\end{aligned}$$

An equivalent expression can be written for the third moment expansion of the radial velocity:

$$\overline{(V_r - \bar{V}_r)^3} = \overline{u'^3} cos^3\theta sin^3\beta + \overline{v'^3} cos^3\theta cos^3\beta + \overline{w'^3} sin^3\theta$$

$$+ 3\overline{u'^2 v'} cos^3\theta sin^2\beta cos\beta + 3\overline{u'^2 w'} cos^2\theta sin\theta sin^2\beta$$

$$+ 3\overline{u' v'^2} cos^3\theta cos^2\beta sin\beta + 3\overline{v'^2 w'} cos^2\theta sin\theta cos^2\beta$$

$$+ 3\overline{u' w'^2} sin^2\theta cos\theta sin\beta + 3\overline{v' w'^2} sin^2\theta cos\theta cos\beta$$

$$+ 6\overline{u' v' w'} cos^2\theta sin\theta sin\beta cos\beta$$

Again changing the sine and cosine terms to Euler expressions gives the expression for the third moment of the radial velocity data as

$$\overline{(V_r - \bar{V}_r)^3} = \overline{u'^3} cos^3\theta \left[-\frac{i}{8}\left(e^{3i\beta} - 3e^{i\beta} + 3e^{-i\beta} - e^{-3i\beta}\right) \right]$$

$$+ \overline{v'^3} cos^3\theta \left[\frac{1}{8}\left(e^{3i\beta} + 3e^{i\beta} + 3e^{-i\beta} + e^{-3i\beta}\right) \right] + \overline{w'^3} sin^3\theta$$

$$+ 3\overline{u'^2 v'} cos^3\theta \left[-\frac{1}{8}\left(e^{3i\beta} - e^{i\beta} - e^{-i\beta} + e^{-3i\beta}\right) \right]$$

$$+ 3\overline{u' v'^2} cos^3\theta \left[-\frac{i}{8}\left(e^{3i\beta} + e^{i\beta} - e^{-i\beta} - e^{-3i\beta}\right) \right]$$

$$+ 3\overline{u'^2 w'} cos^2\theta sin\theta \left[-\frac{1}{4}\left(e^{2i\beta} + e^{-2i\beta} - 2\right) \right]$$

$$+ 3\overline{v'^2 w'} cos^2\theta sin\theta \left[\frac{1}{4}\left(e^{2i\beta} + e^{-2i\beta} + 2\right) \right]$$

$$+ 3\overline{u' w'^2} sin^2\theta cos\theta \left[-\frac{i}{2}\left(e^{i\beta} - e^{-i\beta}\right) \right]$$

$$+ 3\overline{v' w'^2} sin^2\theta cos\theta \left[\frac{1}{2}\left(e^{i\beta} + e^{-i\beta}\right) \right]$$

$$+ 6\overline{u' v' w'} cos^2\theta sin\theta \left[-\frac{i}{4}\left(e^{2i\beta} - e^{-2i\beta}\right) \right] \qquad (9)$$

with the least-squares analysis of $\overline{V_r'^3}$ producing the coefficients

$$\begin{aligned}
A_0 &= \overline{w'^3} sin^3\theta + \tfrac{3}{2}\overline{u'^2 w'} cos^2\theta sin\theta + \tfrac{3}{2}\overline{v'^2 w'} cos^2\theta sin\theta \\
A_1 &= \tfrac{3}{8}\overline{v'^3} cos^3\theta + \tfrac{3}{8}\overline{u'^2 v'} cos^3\theta + \tfrac{3}{2}\overline{v' w'^2} sin^2\theta cos\theta \\
A_{1i} &= \tfrac{3}{8}\overline{u'^3} cos^3\theta - \tfrac{3}{8}\overline{v'^2 u'} cos^3\theta - \tfrac{3}{2}\overline{u' w'^2} sin^2\theta cos\theta \\
A_2 &= -\tfrac{3}{4} cos^2\theta sin\theta \left(\overline{v'^2 w'} - \overline{u'^2 w'}\right) \\
A_{2i} &= -\tfrac{3}{2}\overline{u'v'w'} cos^2\theta sin\theta \\
A_3 &= \tfrac{1}{8}\overline{v'^3} cos^3\theta - \tfrac{3}{8}\overline{u'^2 v'} cos^3\theta \\
A_{3i} &= \tfrac{1}{8}\overline{u'^3} cos^3\theta - \tfrac{3}{8}\overline{v'^2 u'} cos^3\theta
\end{aligned}$$

The harmonic coefficients derived above contain all of the terms needed to solve the simplified turbulent momentum flux budget equations (2) and (3) except for the buoyancy, pressure and eddy dissipation terms.

3. DATA

The data were collected by programming the radar to scan at a fixed elevation angle for one entire 360 degree revolution (one VAD scan) at which time the elevation angle would be changed. A series of three to four different elevation angles would be scanned one after another. This series of elevation angles (one volume scan) was then repeated continuously. The elevation angles used and the reasons for selecting specific angles will be discussed later in this chapter.

The radar obtains estimates of radial velocity (in addition to a number of other parameters such as returned power) by sending out a pulse of electromagnetic energy (one trigger) at a fixed wave length (3.2 cm for the X-band radar). The radar then receives echoes of this transmitter energy from PBL targets. In the summer convective PBL these targets are believed to be insects, dust or other millimeter sized constituents (Kropfli, 1986). These echoes are sampled in discrete time intervals, referred to as range gates, which determine the radial resolution of the radar. (Since electromagnetic waves travel at the speed of light, approximately 300 m per μs, time and length can be used interchangeably.) Each range gate also has a finite depth, or pulse length. The pulse length is determined by the time required to obtain an estimate of the various data fields at each given range. Another parameter which affects the radar resolution is the gate spacing. This is the distance (or time) between the center of each range gate.

The WPL radar has a beam width of 0.8°. The radar beam can be considered essentially circular in the lateral direction. This implies a diameter of a few m up to a maximum of 50 m at the top of the boundary layer for the lowest elevation scans used in this study. Using a pulse length of 112.5 m as a typical example produces a cylindrical resolution volume for this radar with average dimensions of 30 m in diameter by 112.5 m in length for boundary layer studies (refer to Fig. 2). This small pulse volume produces a resolution which exceeds most other measurement techniques and is on the same order as LES models.

To obtain statistically significant and accurate estimates of radial velocity (as well as other data parameters) a number of triggers (pulses) are electronically averaged together at each range gate to produce one beam of data. For a sweep typical to this study there were 250 pairs of triggers (one pair is required to obtain the phase information needed to compute Doppler velocities) for each beam and 200 beams of data (one sweep) in 2 minutes. This translates into over 400 samples per second at each height or a total of 5×10^4 samples at each height for each sweep. This fast sampling rate in conjunction with the small pulse volume produces very accurate estimates of the radial velocity which translates into high accuracy in the derived turbulence statistics. Some factors which can degrade this accuracy and should be considered, especially in boundary layer studies, are the signal to noise ratio of the data and side lobe contamination from ground clutter. Table 1 contains a summary of the three data sets and the specific radar parameters which were used to collect them.

3a. NDTP Radar Data

During the NDTP VAD scans were performed at a series of four different elevation angles: 35.3°, 50.8°, 68.9° and 89.7°. (The significance of these angles will be discussed in the section covering the analysis procedures.) This volume scan took a total of eight minutes to complete, each scan being two minutes in length. The pulse length for these data was 112.5 m, the gate spacing 75 m and 510 triggers were averaged together to produce one beam of data. Each beam had 67 range gates and 197 beams in each sweep. Data were collected from a minimum range of 0.0 km out to a maximum radial range of 5.0 km. In reality the effective

TABLE 1

SUMMARY OF DATA SET LOCATIONS, TIMES AND RADAR PARAMETERS USED DURING DATA COLLECTION.

	NDTP 1-2Jul89	NDTP 27-28Jun89	3CPO 19Jun88
Site	New Salem, ND	New Salem, ND	Ivesdale, IL
Data Times (CDT)	14:20 1Jul89- 02:04 2Jul89	16:24 27Jun89- 02:28 28Jun89	10:14 19Jun89- 16:20 19Jun89
Scan Types	4-Angle VAD	4-Angle VAD	3-Angle VAD
Elevations (degrees)	35.3,50.8, 68.9,89.7	35.3,50.8, 68.9,89.7	35.3,50.8, 89.7
Scan times/ Volume time	2 minutes/ 8 minutes	2 minutes/ 8 minutes	1 minute/ 3 minutes
Beams/Sweep	197	197	197
Number of range gates	67	67	50
Gate spacing	75 meters	75 meters	75 meters
Pulse Length	112.5 meters	112.5 meters	112.5 meters
Numbers of Triggers	510	510	380

minimum radial range of this radar is on the order of 150-250 m, due mainly to the time required for the radar electronics to stabilize after each transmission.

Data were collected on two days beginning in the afternoon and lasting into the night. The first of these days was 27-28Jun89. Data collection began at 16:24 CST on 27Jun89 and ended at 02:28 CST on 28Jun89 for a total of 10 hours of data. The second data set contains nearly twelve hours of data beginning at 14:20 CST 1Jul89 and ending at 02:04 CST on 2-Jul89. Both data sets have essentially continuous data. The radar was manned during daytime hours and allowed to run unattended after 20:00 CST. The cutoff in data recording around 02:00 CST was a consequence of the radar data tape storage capacity.

3b. 3CPO Radar Data

The third data set was obtained with the same radar during the summer of 1988 near Champaign, Illinois (Ivesdale , IL) as part of the 3CPO project. These data consist of three angle VAD volume scans with elevations of 35.3°, 50.8° and 89.9°. The pulse length was 112.5 m, gate spacing 75 m and 380 triggers were averaged to produce one beam. Each scan had 50 gates, 197 beams and lasted one minute for a total volume time of three minutes. There was one day of data with the three angle VAD's which began on 19Jun90 at 10:14 and ended 19Jun90 near 16:20 CDT. This data set is also essentially continuous.

3c. Site Descriptions

The radar site during the NDTP was approximately 50 km west of Bismarck, North Dakota (near New Salem, ND). Local terrain was mostly grasslands with gradual rolling hills. These hills had a typical rise of less than 50 m over a horizontal distance of a few kilometers. Any potential influence on the PBL structure should be limited to the lowest few hundred meters. During the 3CPO project the radar was located on very flat terrain with the only surrounding obstructions being scattered trees and buildings.

4. ANALYSIS PROCEDURES

4a. Scanning Strategy

To simplify the solution of the required turbulence statistics a specific scanning strategy was devised. The elevation angles of 35.3°, 50.8° and 89.7° have particular significance. At 35.3° the zero harmonic from the second moment analysis is such that the leading coefficients of the variance terms on the righthand side are all equal. Therefore the turbulent kinetic energy (TKE) can be derived directly. Similarly at 50.8° the zero-order harmonic from the third moment analysis has equal coefficients and the vertical flux of TKE can be easily obtained (Frisch et. al., 1989). The 89.7°scans were used to obtain accurate estimates of the vertical velocity and associated statistics. Optimally 90.0° would be used however mechanical restrictions with the radar prohibited this. A harmonic analysis is also performed at 89.7° which should produce results nearly as accurate as a 90.0° scan. At this high elevation angle $sin\theta \gg cos\theta$ which allows $\bar{w}$ to be determined from the mean wind A_o coefficient, $\overline{w'^2}$ from the second moment A_o coefficient and $\overline{w'^3}$ from A_o from the third moment analysis.

4b. Stress Budget Determination

As outlined above not all statistics are computed at each elevation angle. Based on the scanning geometry (Fig. 2) and assuming a fixed radar range gate spacing, statistics computed at low elevation angles will have a better vertical resolution than the higher elevations angles . This implies that a solution of the momentum flux budget at a given altitude (z) will require the interpolation of statistics between data points at certain elevation angles. The heights at which the flux budgets were solved were chosen to coincide with the measurements obtained from the near-vertical sweeps, producing an effective vertical resolution of 75 m. While this is the lowest resolution possible with this technique, it minimizes the required interpolation distances. For a range gate spacing of 75 m this produces maximum interpolation distances of 35 m at 68.9°, 29 m at 50.8° and 22 m at 35.3° elevation. Since these are relatively short distances in terms of PBL mixed layer scales, a simple linear interpolation scheme was employed.

The only terms which cannot be derived directly or by making appropriate simplifying assumptions are $\overline{u'w'^2}$ and $\overline{v'w'^2}$. Since the solutions for $\overline{u'w'^2}$ and $\overline{v'w'^2}$ are essentially the same, only the solution for $\overline{u'w'^2}$ will be outlined. The triple correlation $\overline{u'w'^2}$ is contained in the first harmonic of the third moment analysis (A_{1i}). However there are two additional terms involving $\overline{u'^3}$ and $\overline{v'^2u'}$. One term can be eliminated by subtracting A_{3i} from A_{1i} to give:

$$A_{1i} \;-\; A_{3i} \;=\; \tfrac{1}{4}\overline{u'^3}cos^3\theta \;-\; \tfrac{3}{2}\overline{u'w'^2}sin^2\theta cos\theta$$

Using two different elevation angles, producing two equations in two unknowns, allows this equations to be solved as:

$$\frac{3}{2}\overline{u'w'^2} \;=\; \left[(A_{1i\theta_0} \;-\; A_{3i\theta_0})cos^3\theta_1 \;-\; (A_{1i\theta_1} \;-\; A_{3i\theta_1})cos^3\theta_0\right]$$

$$\div\; \left[sin^2\theta_1 cos\theta_1 cos^3\theta_0 \;-\; sin^2\theta_0 cos\theta_0 cos^3\theta_1\right]$$

An equivalent solution follows for $\overline{v'w'^2}$.

4c. Data Quality Considerations

Before processing the radar data with the VAD analysis program a number of steps were taken to ensure quality of the data. Random samples of the data were initially displayed on the National Center for Atmospheric Research's (NCAR) Research Data Support System (RDSS). This system allows for easy identification of any velocity data which may be folded. The Nyquist velocity for these data was set at 21 ms^{-1} which was sufficient to prevent folding of the three data sets.

The RDSS display also allows the identification of any significant ground clutter contamination.

As another method of monitoring the quality of the radar data a correlation field is created during data collection. This field represents the degree of correlation between pairs of pulses. A correlation threshold of 0.4 was used when the velocity data were processed. This will not eliminate ground clutter which is typically well correlated, but it does help eliminate bad data when the signal to noise ratio becomes small. This usually occurs just above the inversion height (Frisch and Uttal, 1988) where relatively clean free atmospheric air becomes dominant and boundary layer scatters are lost.

4d. Data Averaging

After the initial data quality checks were complete, a first pass analysis of the data was performed. Processing only one scan or one volume scan would only give a view of the turbulence over a period of a few minutes. Since the time scale of PBL processes is on average around 10 to 20 minutes (Kaimal et. al. 1976) the turbulence derived from a single volume will incorporate only a fraction of one or two thermals. It is therefore desirable to average over a number of volume scans in order that the derived statistics are representative of the current state of the PBL and incorporate a number of thermals. A one-hour averaging time was selected for these data. This was felt to be sufficiently long so as to encompass a number of buoyant plumes and short enough so that temporal changes in mean quantities would be minimal.

For the NDTP data eight volume scans (32 sweeps, eight at each of the four elevation angles) were averaged together to give an averaging time of approximately 64 minutes. Thirteen volumes (39 sweeps, 13 at each of the three elevation angles) of the 3CPO data were averaged for an averaging time of 57 minutes. As a check that this averaging period was sufficient, a comparison of the

NDTP data was made between an average of eight volumes, an average computed from the first seven volume scans and an average computed from the last seven volume scans. This constitutes a time difference of eight minutes (the length of one volume scan) between each of the averaging periods. Although the mean wind should not be expected to change significantly in eight minutes, momentum flux and higher-ordered statistics could have significant changes. Therefore if the averaging period is too short turbulence statistics will not be stable. The results in Fig. 4 show a comparison of the mean wind, momentum flux and turbulent transport of momentum flux for the three averaging periods. There are differences, particularly in the stress plots, however they are relatively small. Based on these results the averaging period of one hour will be assumed appropriate and used as the basis for turbulence calculations in this study.

4e. Software Development

Due to deficiencies of existing software for processing VAD scans a significant portion of this research effort was devoted to the development of a new VAD analysis package. Most of the logic of this program centered around the four angle VAD scanning strategies of the NDTP project and the desire to derive third-order velocity statistics. Since there were no other available programs to use for comparison, a series of data simulations were conducted as a test of the programs validity. These consisted of using input data of known harmonic components and comparing these with the analysis output. Other tests included adding noise components of varying magnitudes on top of the known input data. In all cases the program was able to retrieve the appropriate input harmonics. It is therefore felt to be adequately tested for accuracy.

Numerous turbulent statistics profiles are computed by the analysis software including those discussed previously which are needed for solving the momentum flux budget. Others include reflectivity profiles and eddy dissipation rate (edr)

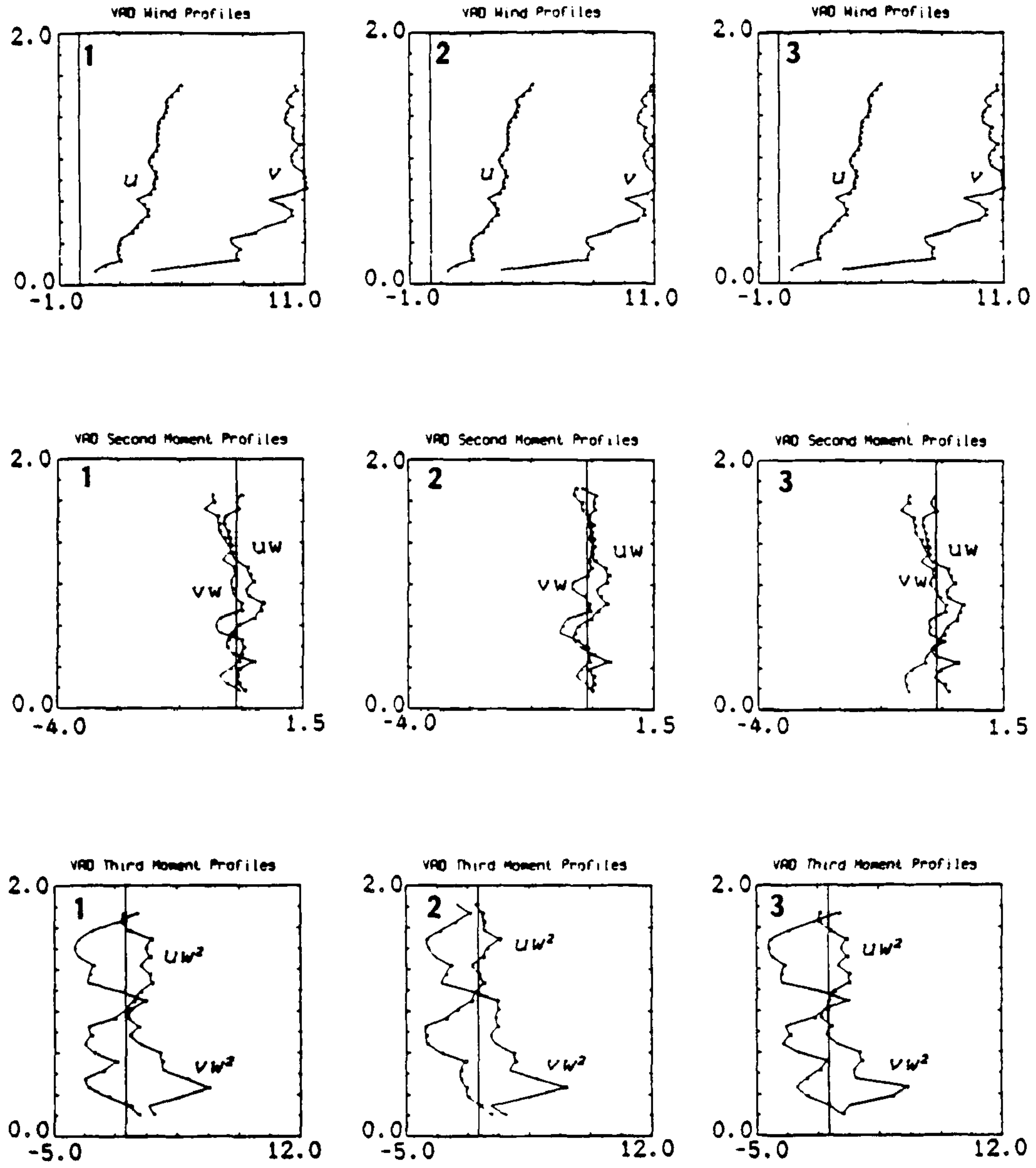

Fig. 4. Comparison of averaging periods at 14:20 CDT for 1Jul89. Plots with a number 1 in the upper lefthand corner are averages for 8 volume scans. A number 2 indicates the first seven of the 8 volume scans and a 3 the last seven of the 8 volume scans. Vertical scale is km. Horizontal scales are ms^{-1} for velocity, m^2s^{-2} for stresses and m^3s^{-3} for the third moment quantities.

estimates (Frisch and Clifford, 1974) from all elevation angles. From the 35.3° elevations sweeps $\bar{u}$ and $\bar{v}$ are computed since this is the lowest elevation and will provide the best estimates of horizontal components. Also $\overline{u'v'}$, divergence assuming $\bar{w}$ has a negligible influence at this low elevation, $\overline{u'^2}$ and $\overline{v'^2}$, and TKE are all computed at 35.3°. At 50.8° the turbulent momentum flux ($\overline{u'w'}$ and $\overline{v'w'}$), $\overline{u'v'w'}$, and the vertical flux of TKE are calculated. The 68.9° scans are used simultaneously with the 50.8° scans to estimate the third moment terms $\overline{u'w'^2}$ and $\overline{v'w'^2}$. The near vertical scans are used for all vertical velocity statistics including $\overline{w'^2}$, $\overline{w'^3}$, and the third moment measure of skewness.

In order to determine some lower limit on the accuracy of the derived turbulence statistics, simulations were performed in which a single harmonic wind field (i.e. a mean wind with no associated turbulence) was used as input with random noise superimposed. The noise can be interpreted as a measure of the uncertainty in the radar radial velocity estimates. This mean wind with the superimposed noise was used as input to the analysis program. Any turbulence quantities derived by the program will be a measure of the minimum accuracy obtainable for a given uncertainty in the radial velocity estimates. Turbulence values greater than this "noise" turbulence can be assumed to be the result of atmospheric turbulence. The results are summarized in Table 2.

4f. Determination of z_i from the Radar Data

The first pass through the VAD analysis program utilized a low thresholding scheme. This thresholding refers to the amount of averaging which is performed. Two parameters affect the average: the number of beams per sweep with good data and the number of sweeps with good data. The number of beams per sweep with good data is determined from the velocity thresholding against the correlation field value of 0.4. For this first pass only 25 beams per sweep from the 197 total were required to pass this threshold at a given range. If a sweep had at least 25 beams

TABLE 2

ERROR ESITMATES OF THE VAD ANALYSIS
PROGRAM OBTAINED USING A KNOWN INPUT MEAN WIND WITH
A +/- 0.5 M/S SUPERIMPOSED NOISE.

Turbulent Parameter	Absolute Error
Vertical Velocity Variance	+/- 0.095m^2/s^2
Stress Components	+/- 0.025m^2/s^2
Turbulent Transport	+/- 0.015m^3/s^3

passing this criteria at a given range gate then it was considered to have good data at that range and turbulence statistics would be computed. The second parameter, the number of good sweeps, is then the number of sweeps in an averaging period at a given elevation angle and range which pass the minimum number of beams criteria. It should be reiterated that separate averages are maintained for each elevation angle and this thresholding is performed independently at each elevation and range. The 25 beams per sweep criteria is sufficient to derive mean wind quantities and if the beams are well distributed around the scanning volume reasonable estimates of second and third moment quantities may be produced, although with greater uncertainty than the mean quantities.

This low thresholding scheme was used mainly as an attempt to identify the top of the PBL (z_i). The upper parts of the entrainment zone have a higher proportion of free atmosphere air and therefore fewer PBL scatterers for the radar to detect. A low threshold for the number of beams per sweep at these heights must then be utilized in order to obtain any turbulence statistic estimates. Since there are essentially no other supporting meteorological data except for the NWS soundings (at most one during each data period), this is the only method to identify the top of the PBL.

Taking the maximum height of the radar echo should serve as an estimate of z_i (assuming clear air conditions with no clouds.) Since boundary layer scatterers produce very weak signals for the radar used in this study (generally -10 to 0 dBZ at relatively close ranges), the range of observation becomes important. The near vertical sweeps have the shortest radial range to any given height within the PBL and should therefore have slightly better sensitivity to boundary layer targets than the lower elevation sweeps. Using data from a one hour average at 18:06 CDT (00:06Z), the 89.7° sweeps gives a z_i of 2.1 km (Fig. 5). This method is in close agreement (within 5 percent) with the National Weather Service (NWS) 00Z

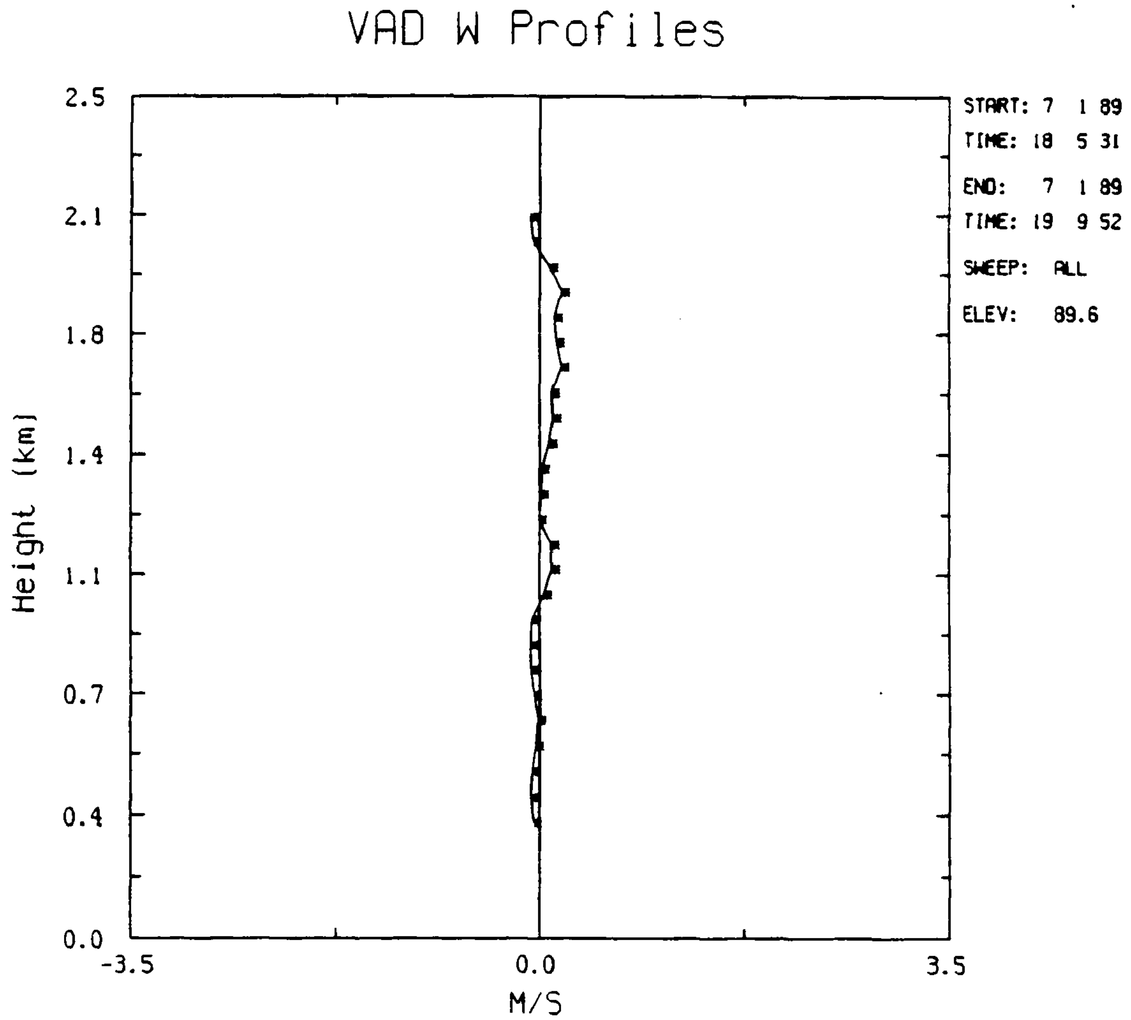

Fig. 5. An 89.6° VAD scan used to estimate the top of the PBL from the vertical extent of radar echo. Top of echo is approximately 2.1 km AGL.

2Jul89 sounding shown in Fig. 6. Therefore when needed throughout this study z_i will be estimated from the height of the echo of the vertical sweeps averaged under a low thresholding scheme. As turbulence becomes very small and the nocturnal boundary layer develops, the top of the radar echo becomes an estimate of the top of the residual layer rather than z_i.

4g. Data Thresholding Schemes

The first pass of the data used a one-hour average for computing mean and turbulence statistics and the low thresholding scheme discussed above. This averaging was performed each half hour creating a one-hour sliding mean in order to compute time changes across a given averaging period and to gain temporal resolution. All three data sets were processed in this manner. A sample of these plots is shown in Fig. 7 for 1Jul89 at 14:20 CDT. They show the profiles of the mean wind components (u, v), mean wind speed (M), average stress components ($\overline{u'w'}$ and $\overline{v'w'}$), the vertical turbulent transport of horizontal momentum flux ($\overline{u'w'^2}$ and $\overline{v'w'^2}$), the mean vertical velocity ($\bar{w}$) and vertical velocity variance ($\overline{w'^2}$), respectively. Each plot is approximately a one-hour average.

The temporal and vertical evolution of the mean and turbulent PBL parameters can easily be derived from the above computations. However a notable problem with the profiles is the amount of fluctuation that occurs at certain heights. The profiles of the mean wind components and wind speed profiles show evidence of ground clutter contamination at several elevations. This can be seen in the bias toward zero on the order of 1 ms^{-1} near the 400 and 700 m levels (Fig. 7). The fluctuations of the turbulence profiles near the top of the PBL is most likely a function of under-sampling and not a result of ground clutter contamination.

Since this clutter contamination is a function of the radial range, the higher elevation sweeps will have clutter contamination at higher altitudes within the PBL (assuming the clutter is within the same range gates for all elevations).

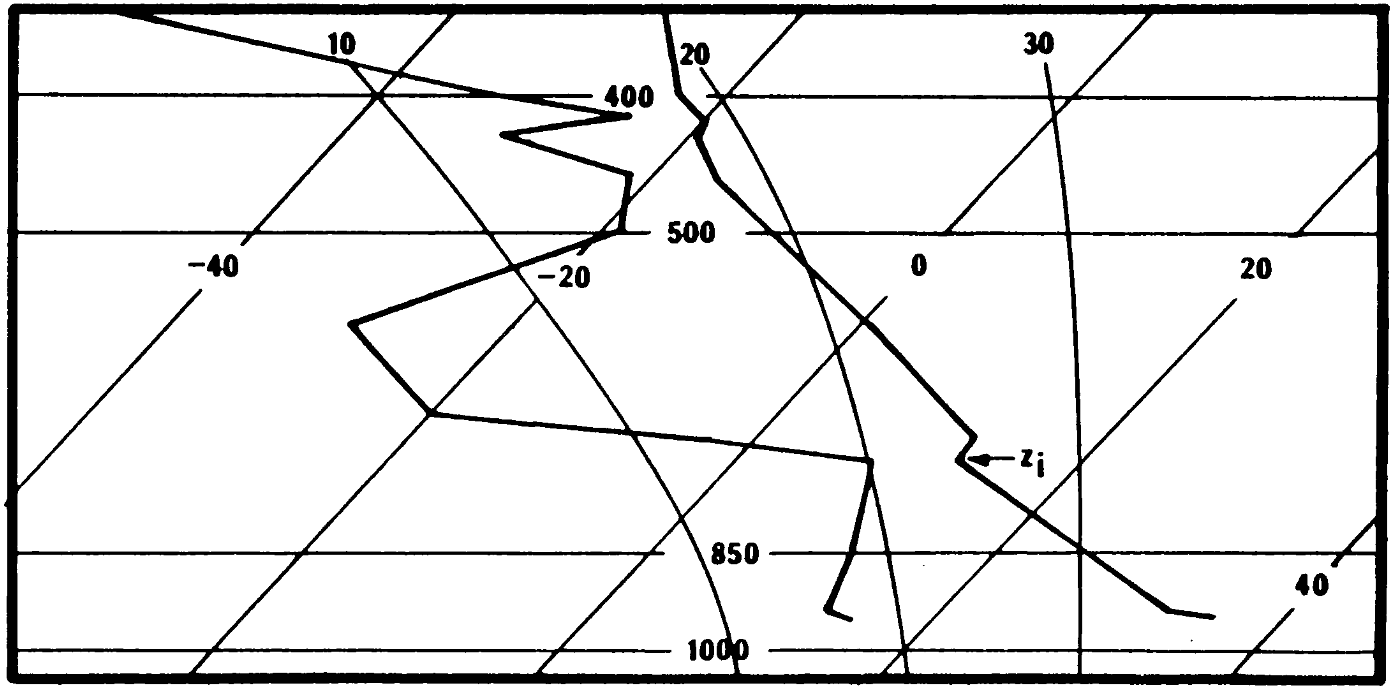

Fig. 6. NWS 00Z Bismarck sounding for 2Jun89. Inversion base is at 2.2 km AGL.

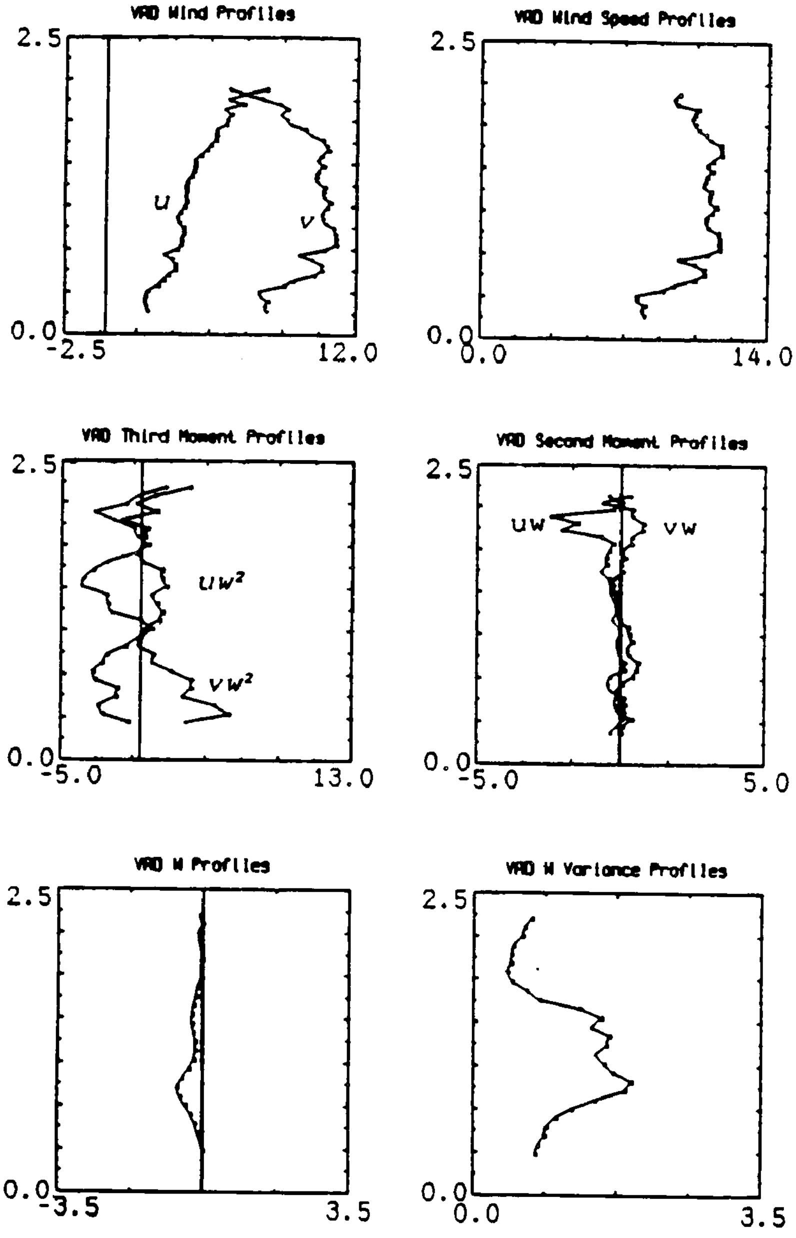

Fig. 7. Initial results from the VAD analysis program utilizing a low-thresholding scheme. Plots are mean profiles of the wind components (ms^{-1}), wind speed (ms^{-1}), vertical turbulent transport of horizontal stresses (m^3s^{-3}), horizontal stress components (m^2s^{-2}), vertical velocity (ms^{-1}) and vertical velocity variance (m^2s^{-2}), respectively. Data is from NDTP at 14:20 CDT on 1Jul89.

The magnitude of ground clutter contamination is a function of the ratio of the relative strengths of the returned signal from PBL scatters and the ground clutter targets (these can be buildings, trees, or even reflections from the earth's surface). Therefore the effect of this clutter can vary with time and height as the concentration of PBL scatterers changes. Besides the bias in the mean wind components, potentially large artificial changes in the turbulence statistics can occur if the magnitude of the ground clutter changes on a scan to scan basis.

The terms needed to solve for the budget equations (2) and (3) require gradients of turbulence quantities. If these gradients were computed from Fig. 7 erroneously large values would be obtained as a result of the fluctuations in these statistics. Stricter thresholding will help reduce these fluctuations at the higher altitudes assuming they are the result of under-sampling. Ground clutter however is typically well correlated and cannot simply be removed by requiring more beams per sweep or a higher value of the correlation field as a threshold. In fact using a higher correlation threshold may eliminate "good" data leaving a higher percentage of beams containing clutter.

One option of dealing with the ground clutter problem was to eliminate the gates containing the clutter on a routine basis from the turbulence calculations. However, examining Fig. 7 it is not clear exactly how many gates are contaminated. The gates most strongly affected are obvious but there is a gradual decrease in the effect of the clutter on either side. If two or three gates above and below the main ground clutter heights (400 and 700 m) were removed this would leave very few data points below 1 km.

As an alternative to dealing specifically with the contaminated range gates a data fitting routine was added to the analysis program. The advantage of fitting a curve through the data is that the gradients in the statistics required for solving (2) and (3) can easily be computed. One disadvantage is that the curve will have a bias from the contaminated gates and the absolute value of points on the curve will be somewhat affected. However the general shape of the profiles should not be greatly altered.

As a test of the influence of using a more strict thresholding scheme and applying a curve fitting routine, the data were processed a second time with the requirement that 100 beams of the 197 pass the correlation field threshold of 0.4 and all eight sweeps at each elevations angle meet this requirement before statistics can be computed. A third-order polynomial was then fit to the data using least-squares methods. This polynomial was felt to be sufficient to capture the general characteristics of the profiles and ordered low enough that it would not pick up significantly on ground clutter-induced fluctuations.

Results of this new thresholding and curve fitting are shown in Fig. 8 for 1Jul89 at 14:20 CDT. This figure is the same time period as Fig. 7 although the scales on the axis have been changed in proportion to maximum values observed during the period. The fluctuations in the upper portions of the PBL have been eliminated with some sacrifice in the vertical extent of the data. The curve fitting represents the data very well in almost all cases. There are cases where some of the second- and third- ordered statistics exhibit a fair amount of scatter but the curve fitting still captures the basic trend of the data.

4h. Momentum Budget Solutions

After applying the more extensive thresholding mentioned above to the data and fitting it with a third-order polynomial, the momentum flux budget equations (2) and (3) were solved following the methods of chapter 2. Considering the minimum effective range of the radar, a solution of these equations within the surface layer is not possible. The more stringent averaging necessary to produce accurate statistical estimates reduces the height coverage of the radar below the top of the PBL. Therefore the solution of (2) and (3) is restricted to the mixed

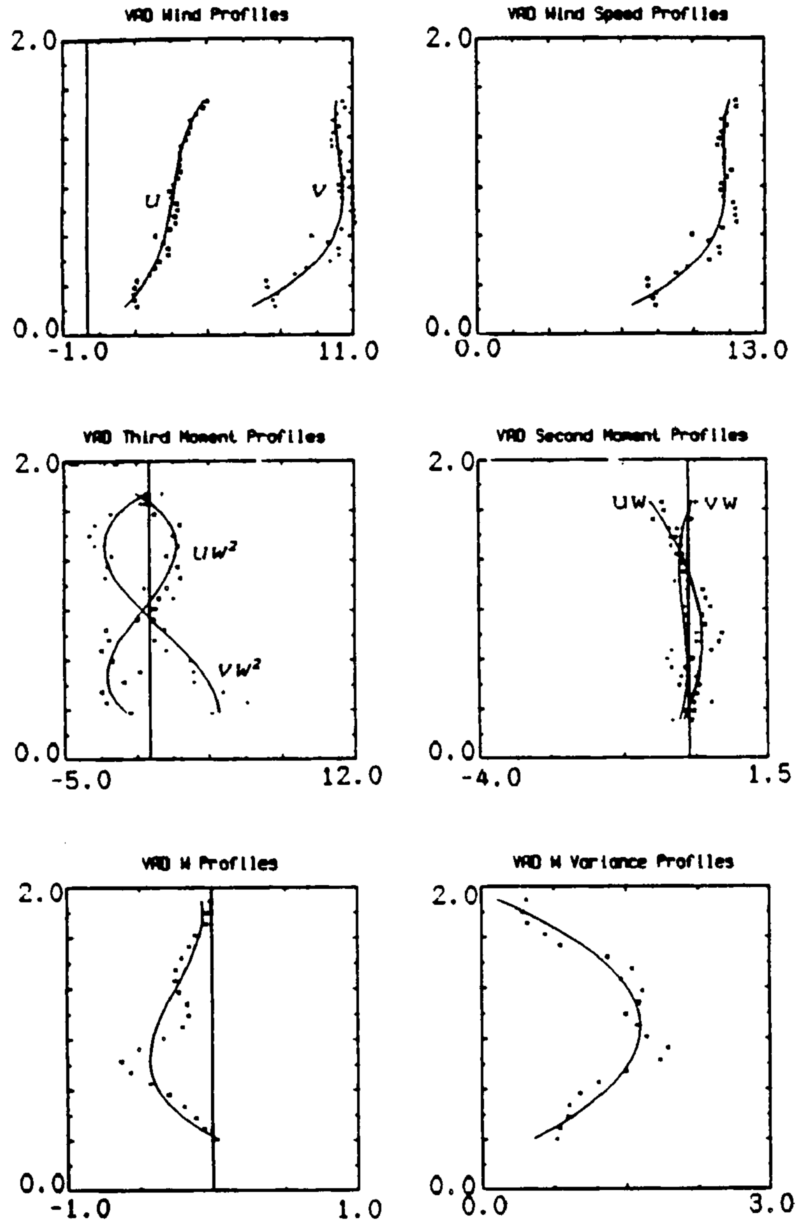

Fig. 8. As in Fig. 8 only using a high-thresholding scheme and a least-squares data fit.

layer, the minimum altitude around 400 m AGL (between $0.2z_i$ and $0.3z_i$) and a maximum height averaging around $0.8z_i$. For the nocturnal boundary layer z_i should simply be considered the radar echo height or the residual layer height.

Time changes in (2) and (3) were determined from averages computed one half hour before and one half hour after the current averaging period. All statistics were derived from the best-fit curve analysis. Therefore the accuracy of the fit had to be considered, although there were few cases where this was a problem.

5. SYNOPTIC AND MESOSCALE ENVIRONMENTS

5a. NDTP 1-2Jul89

A ridge centered over the Great Lakes region was the dominant feature at 500 mb at 00Z on 2Jul89 (Fig. 9). Winds over Bismarck were 8 ms^{-1} from the southwest. By 12Z on 2Jul89 the ridge had moved eastward and winds at Bismarck shifted to the west at 15 ms^{-1}. A surface cold front (more a wind shift than a temperature contrast) in western North Dakota moved slowly eastward through the observational period and was still west of the radar site at the end of data collection. Surface winds were southerly at 5 to 8 ms^{-1} throughout the day, weakening at night. The surface analysis for 23Z 1Jul89 in Fig. 10 shows a core of high temperatures over central South Dakota and south- central North Dakota, indicating weak temperature advection (potentially weak baroclinic tendencies) into the data area. Dew points were between 14°C and 17°C. The high temperature was 36°C at 2350Z on 1-Jul-89. The low was 18°C at 1051Z on 2-Jul-89.

Satellite and radar summaries (not shown) indicate thunderstorms developing late afternoon over South Dakota. These storms built northward into central North Dakota with extensive cloud cover over most of South Dakota and central North Dakota, the strongest storms remaining in South Dakota. All activity began to weaken after 0230Z and moved northeast out of the immediate region. Bismarck indicated a trace of precipitation in the 0050Z and 0150Z observations. No precipitation was evident at the WPL radar site but a significant outflow was observed in the VAD data at 0142Z.

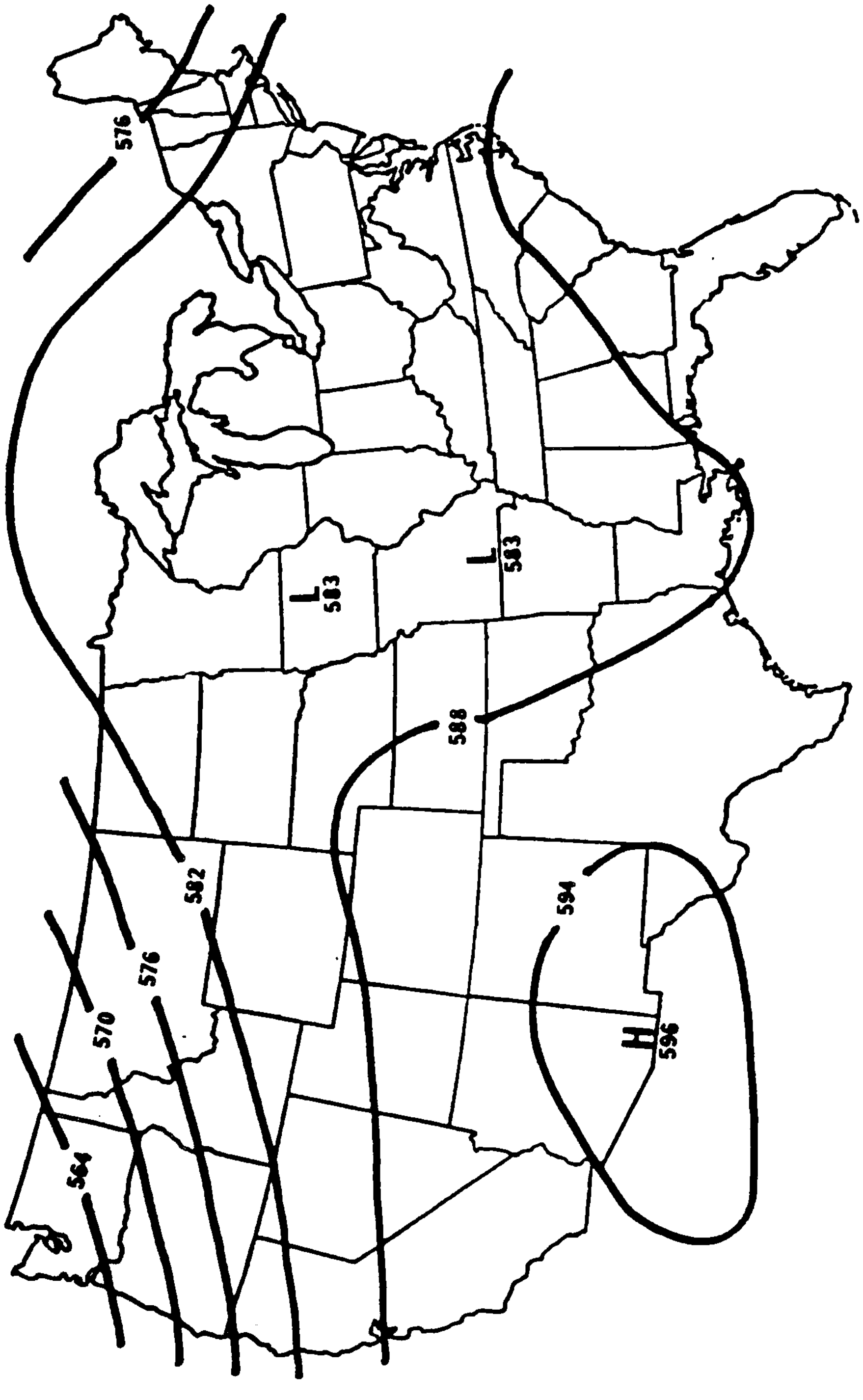

Fig. 9. 500 mb analysis from NDTP at 00Z 2Jul89.

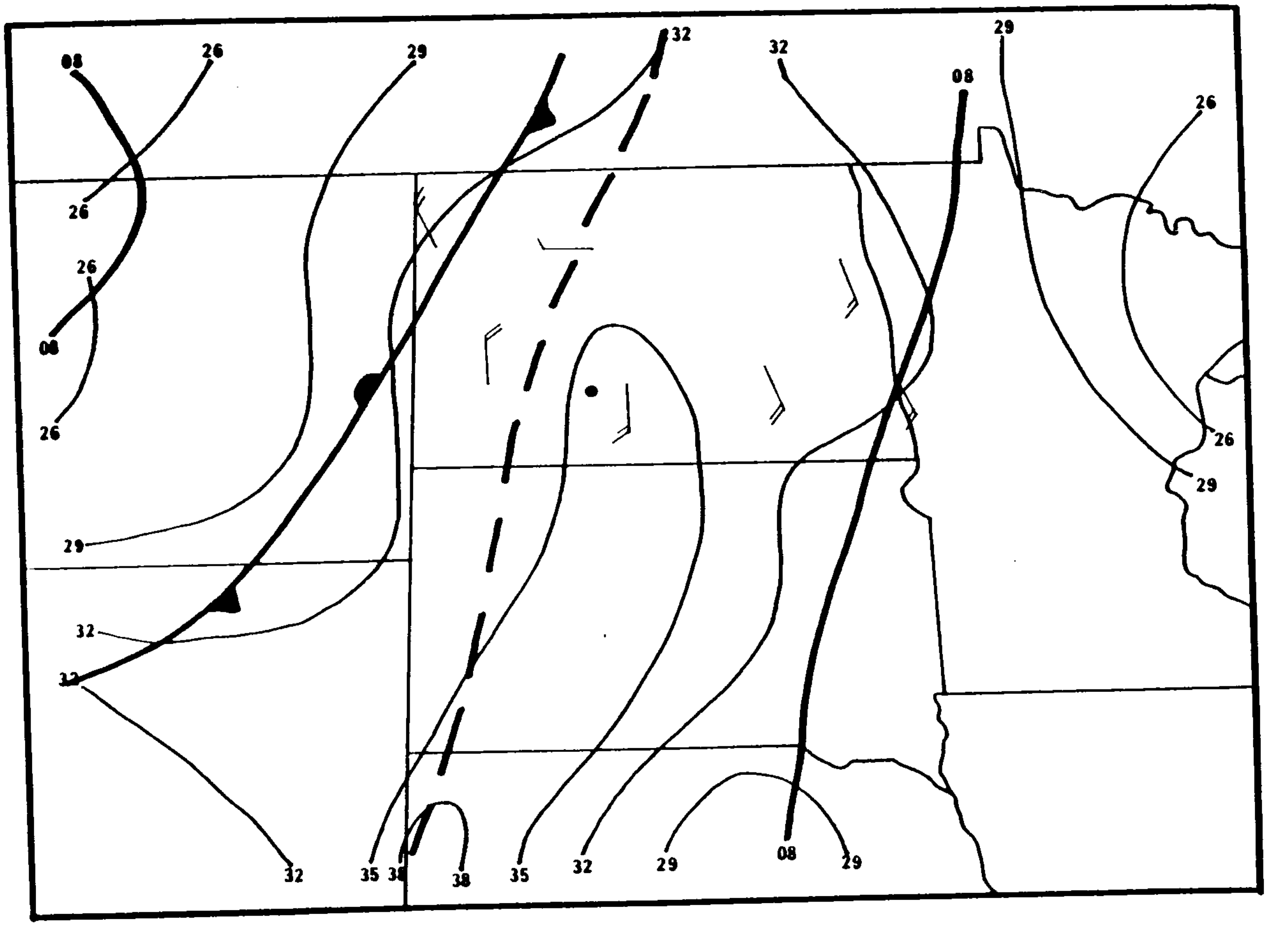

Fig. 10. Surface analysis from NDTP at 22Z 1Jul89. Dot is approximate location of radar site

5b. NDTP 27-28Jun89

A 500 mb ridge axis was centered over western North Dakota at 00Z on 28Jun89 (Fig. 11). Winds at Bismarck were northwesterly at 15 ms^{-1}. The ridge gradually intensified and moved eastward to the be centered over the eastern part of North Dakota by 12Z on 28Jun89 with winds shifting to westerly at 10 ms^{-1} at 500mb. Surface winds were generally northeasterly at 3 ms^{-1} in the eastern part of North Dakota shifting to southeasterly at 5 to 8 ms^{-1} over the central and western portions of the state. A weak warm front meandered through central South Dakota, curving northward across western Montana, reached western North Dakota by 06Z 28Jun89. Surface pressure gradients gradually strengthened over the observational period producing persistent 5 to 8 ms^{-1} easterlies at Bismarck. Figure 12 shows the 21Z 27Jun89 surface analysis. It indicates weak, cool temperature advection across the eastern part of North Dakota into the Bismarck area, indicating moderate baroclinicity.

Thunderstorms developed in the early afternoon in central South Dakota as seen in the radar summaries and satellite observations (not shown). The storms moved to the northeast and entered south-central and southeastern North Dakota by late evening. There were no outflows or precipitation at the radar site from these storms. Dew points were generally between 13°C and 15°C over the south-central sections of the state. The high temperature on 27Jun89 was 33°C at 2150Z and the minimum was 14°C at 1049Z on 28Jun89.

5c. 3CPO 19Jun88

The dominant feature at 500mb on 20Jun88 at 00Z was a broad ridge over the central U.S. and an area of low pressure over Louisiana (Fig. 13). The high had strengthened slightly over the last 12 hours and there was a northward progression of the low pressure area. Winds at 500 mb over Illinois were northerly throughout the observational period. There were no storms in the immediate area with cirrus

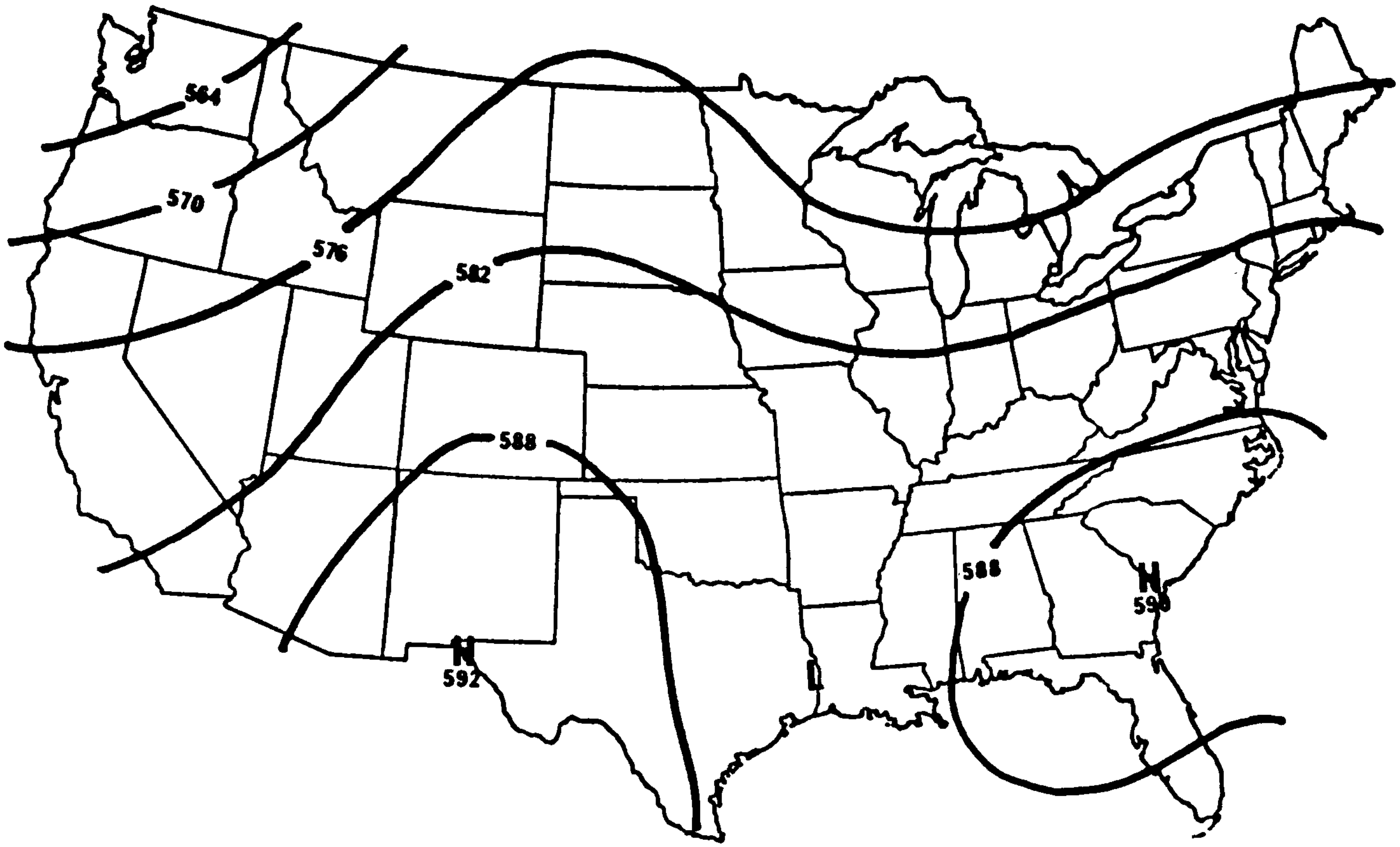

Fig. 11. 500 mb analysis from NDTP at 00Z 28Jun89.

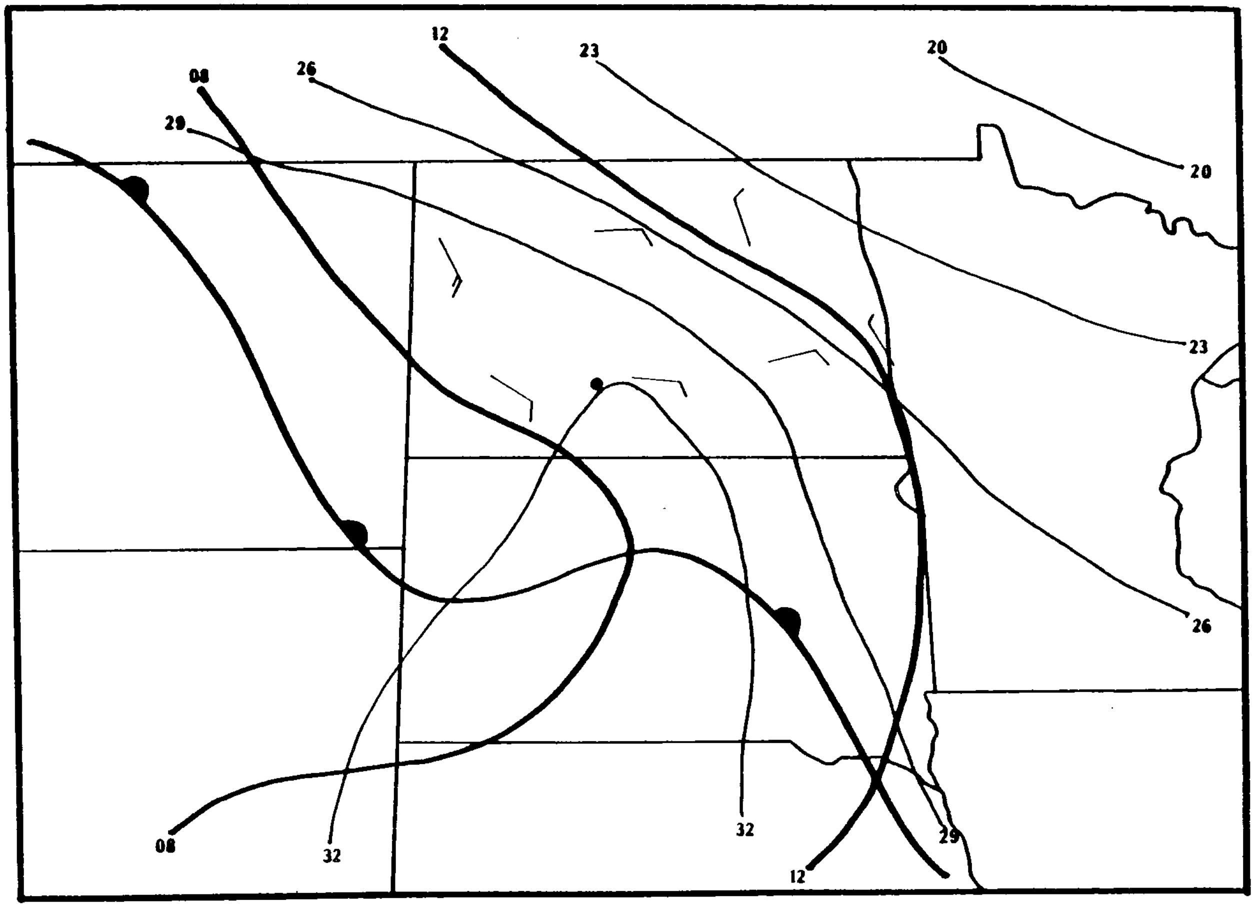

Fig. 12. Surface analysis from NDTP at 21Z 27Jun89. Dot is approximate location of radar site.

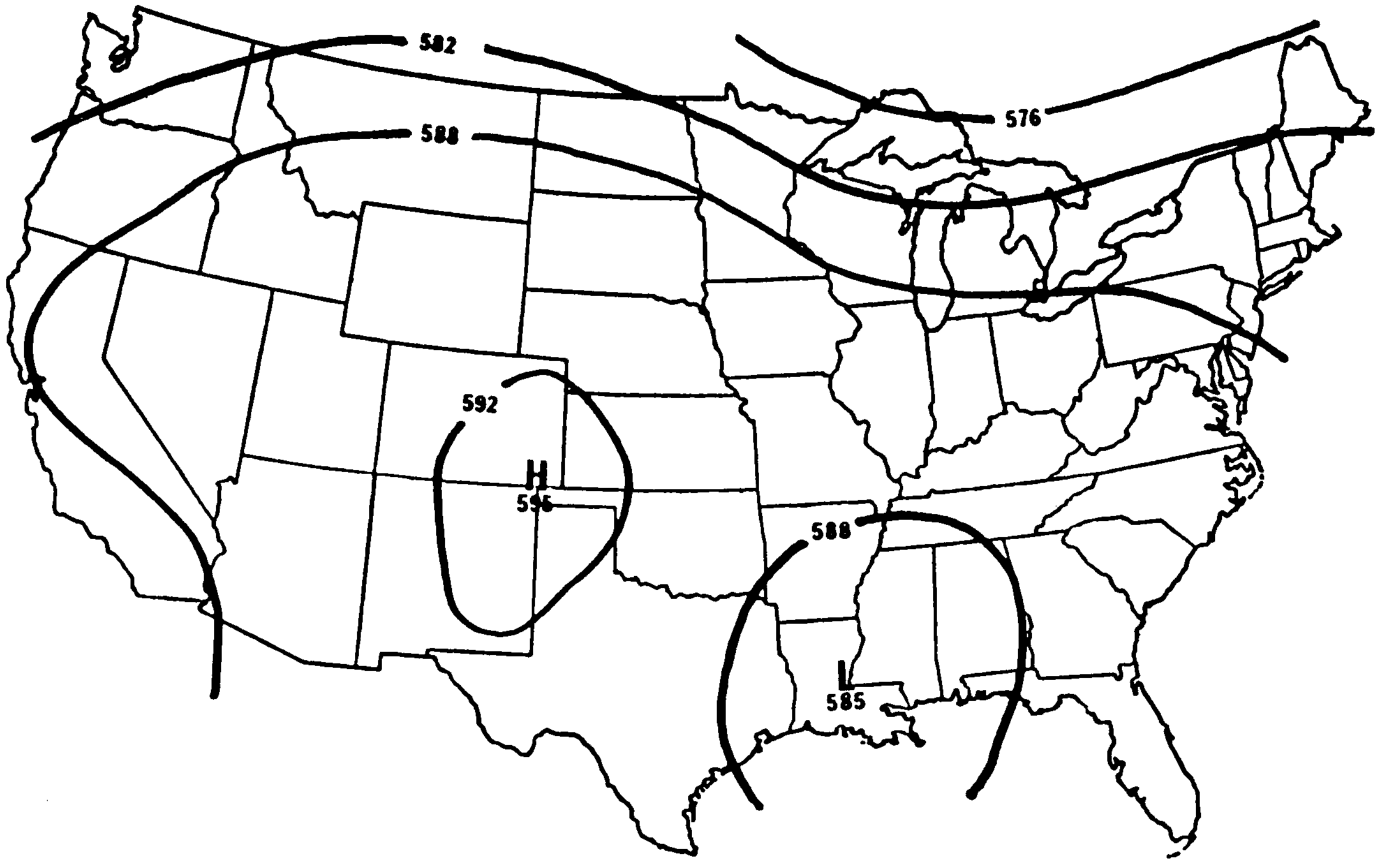

Fig. 13. 500 mb analysis from 3CPO at 00Z 20Jun88.

being the only reported clouds. The surface analysis (Fig. 14) indicates strong high pressure off the east coast and a trough over the central U.S. This produced moderate surface winds from the south to southeast at 3 to 8 ms^{-1} throughout the day. High temperatures over the region were between 32°C and 35°C. High temperature at Champaign was 35°C and dew points ranged from 11°C to 13°C.

All three of these data sets are characterized by hot, clear summer days with moderate surface winds and should have fully developed, convective boundary layers. The only significant clouds were cirrus in 3CPO and widely scattered fair weather cumulus during NDTP. Although there were no significant local disturbances on any of these days (except for a brief outflow observed on 1Jul89) the PBL wind profiles have significant curvature, especially in the lower half of the PBL. There is evidence of weak temperature advection during both days from NDTP, indicating weak baroclinic flow. These data should serve as good cases for measurement of the terms in the turbulent momentum flux budgets (see equations (2) and (3), chapter 2).

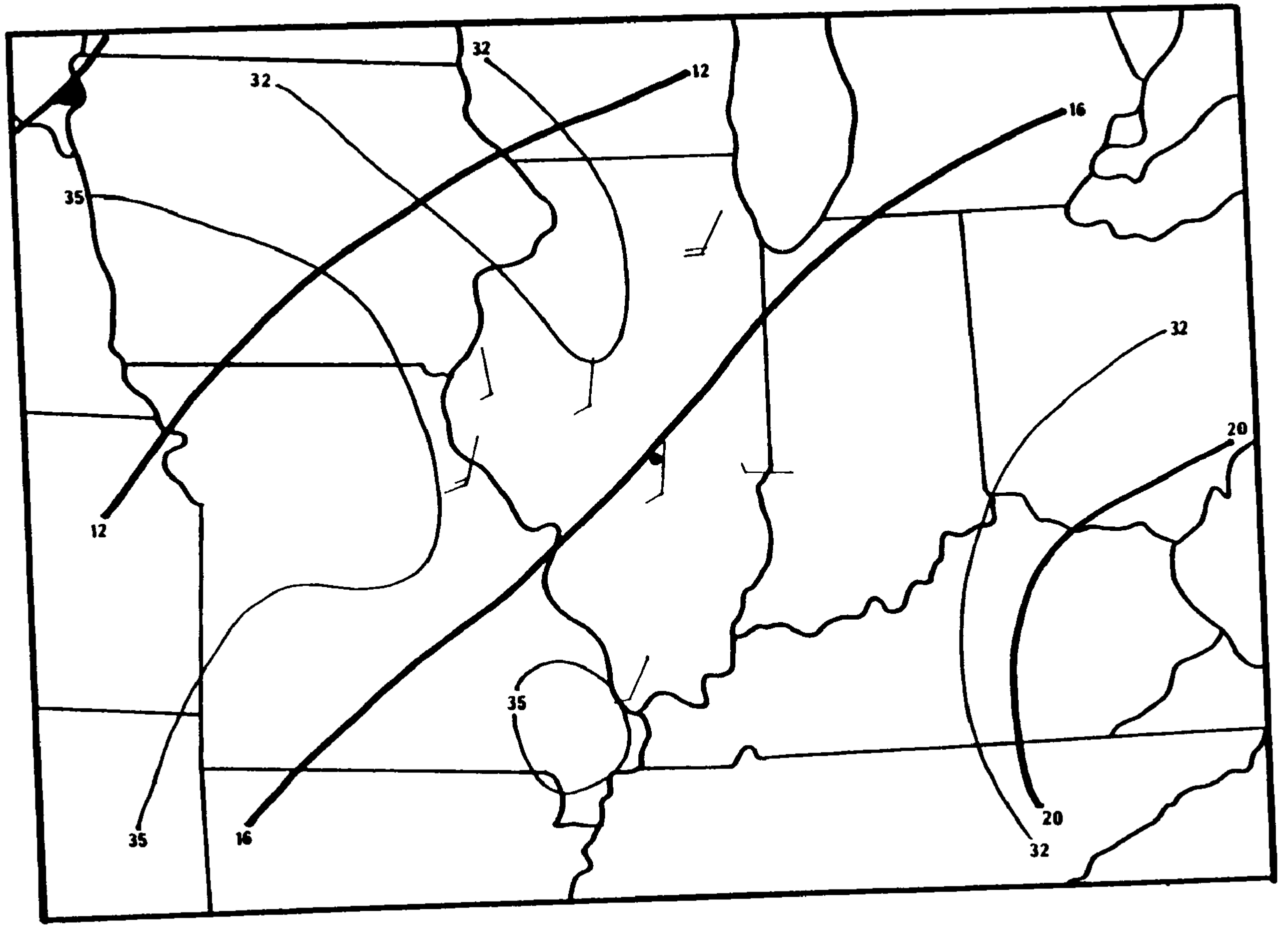

Fig. 14. Surface analysis from 3CPO at 21Z 19Jun88. Dot is approximate location of radar site.

6. CASE STUDY RESULTS

The first part of the next three sections of this chapter will be concerned with general changes occurring in the derived statistics from each of the three data sets. The focus will mainly be on the absolute magnitudes of the statistics rather than characteristic shapes of the profiles, primarily because the profiles are in a general state of flux in all three data sets making any inference about the shapes of these profiles difficult. The second part of these sections will describe the general changes which occur in the absolute magnitudes of the derived terms in the momentum flux budgets (2) and (3). Following these discussions will be a more detailed account of the vertical structure and relative importance of each term within the momentum budget for selected time periods from the NDTP data followed by an overall comparison of the three data sets. The final section of this chapter will examine other available field data and computer model results and their relationships to the radar data.

6a. NDTP 1-2Jul89

i. Evolution of Statistical Turbulence Profiles

Figures 15-20 are a time series from 1-2Jul89 of the derived profiles of the mean wind components, wind speed, turbulent horizontal momentum flux, turbulent transport of horizontal momentum flux, mean vertical velocity and the variance of the vertical velocity, respectively. Each plot is a 64 minute average (8 volume scans).

The mean wind shown in Fig. 15 slowly turned from the SSW at 14:20 CDT to become more westerly by early evening (18:38 CDT). Wind speeds gradually

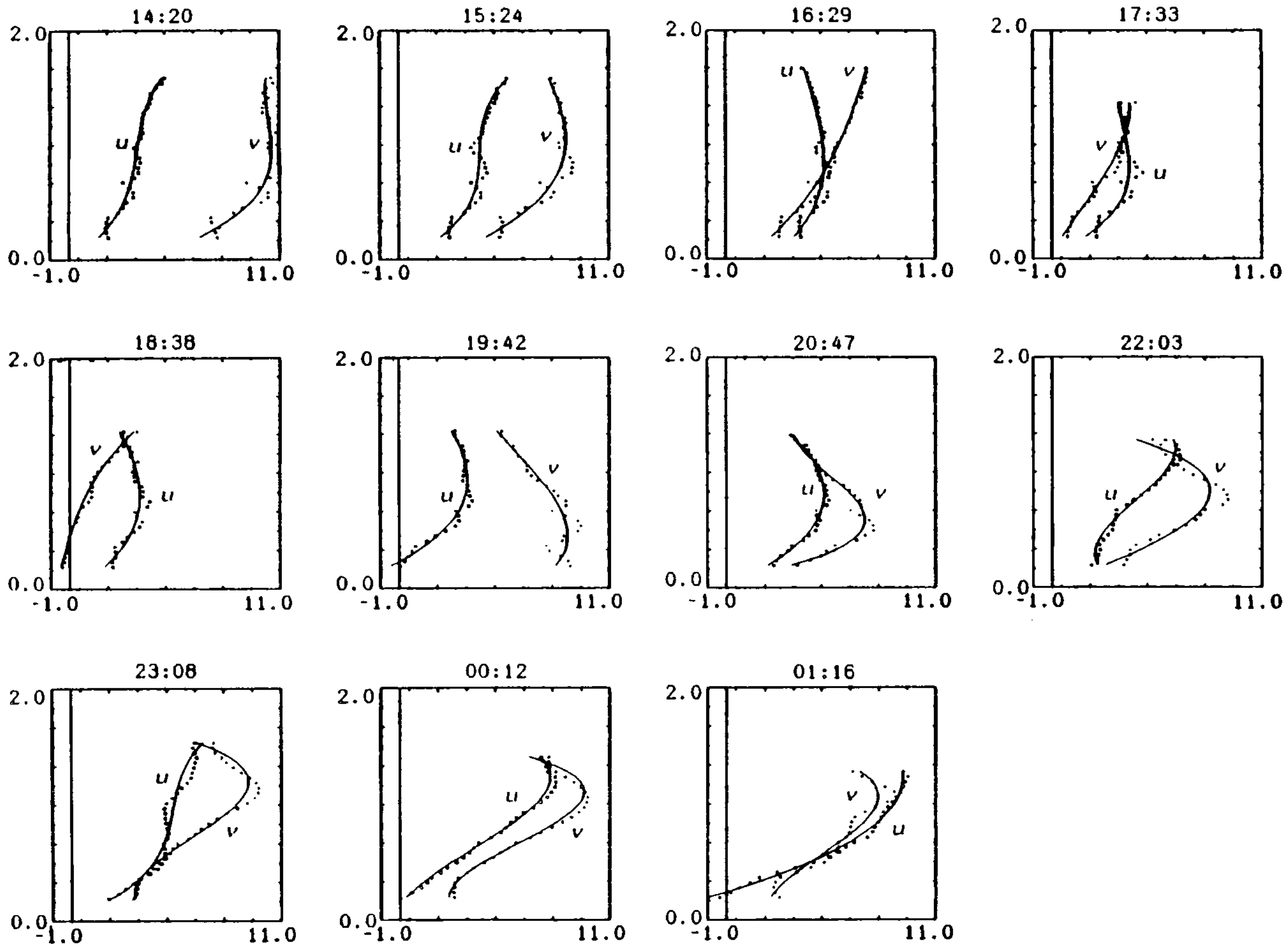

Fig. 15. Time series analysis of mean wind components for 1-2Jul89. Vertical scale is km and horizontal scale is ms^{-1}. All plots are from an eight volume scan average (64 minutes) except the last plot which is only six volume scans.

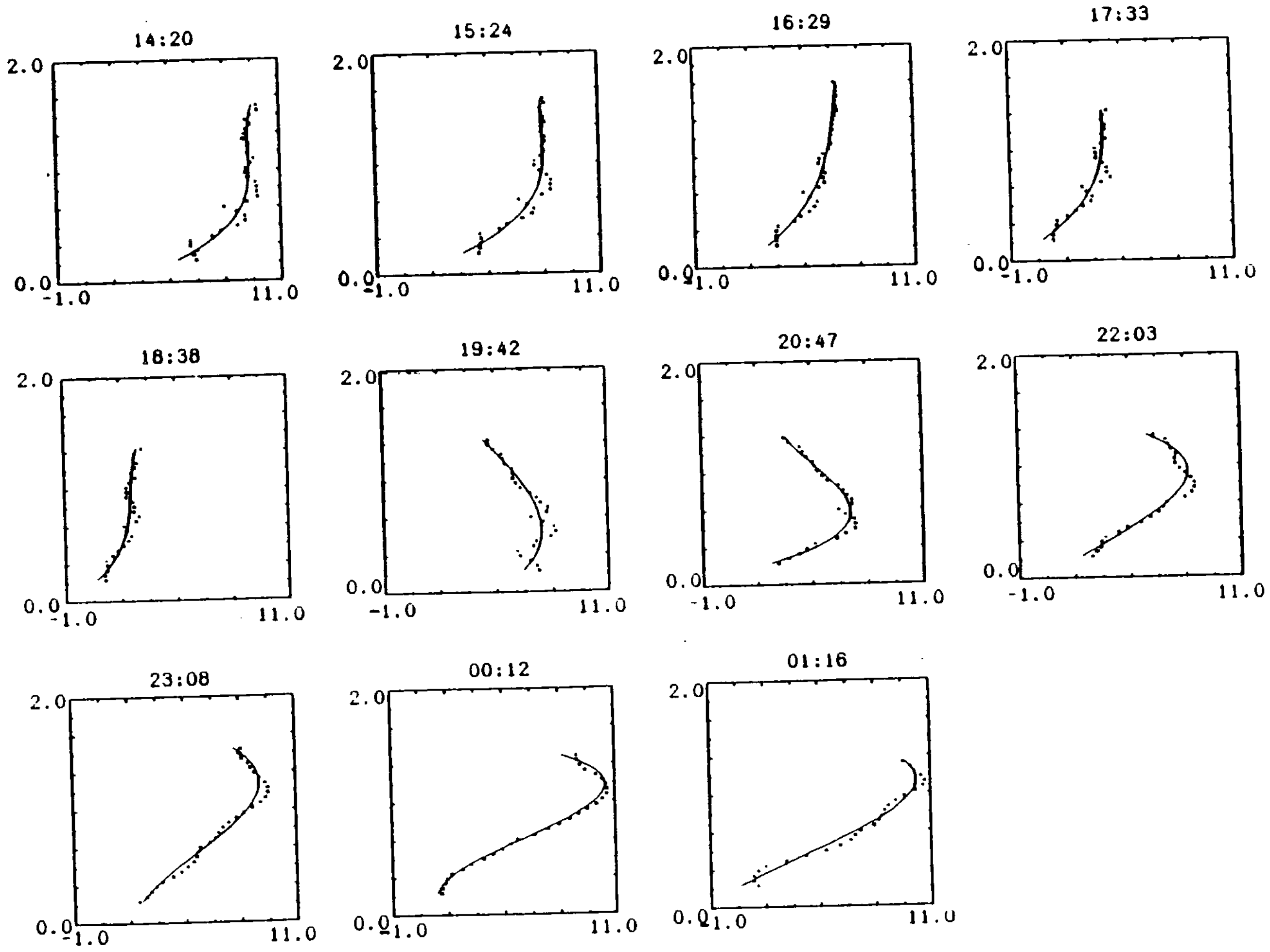

Fig. 16. As in Fig. 15 for wind speed. Horizontal scale is ms^{-1}.

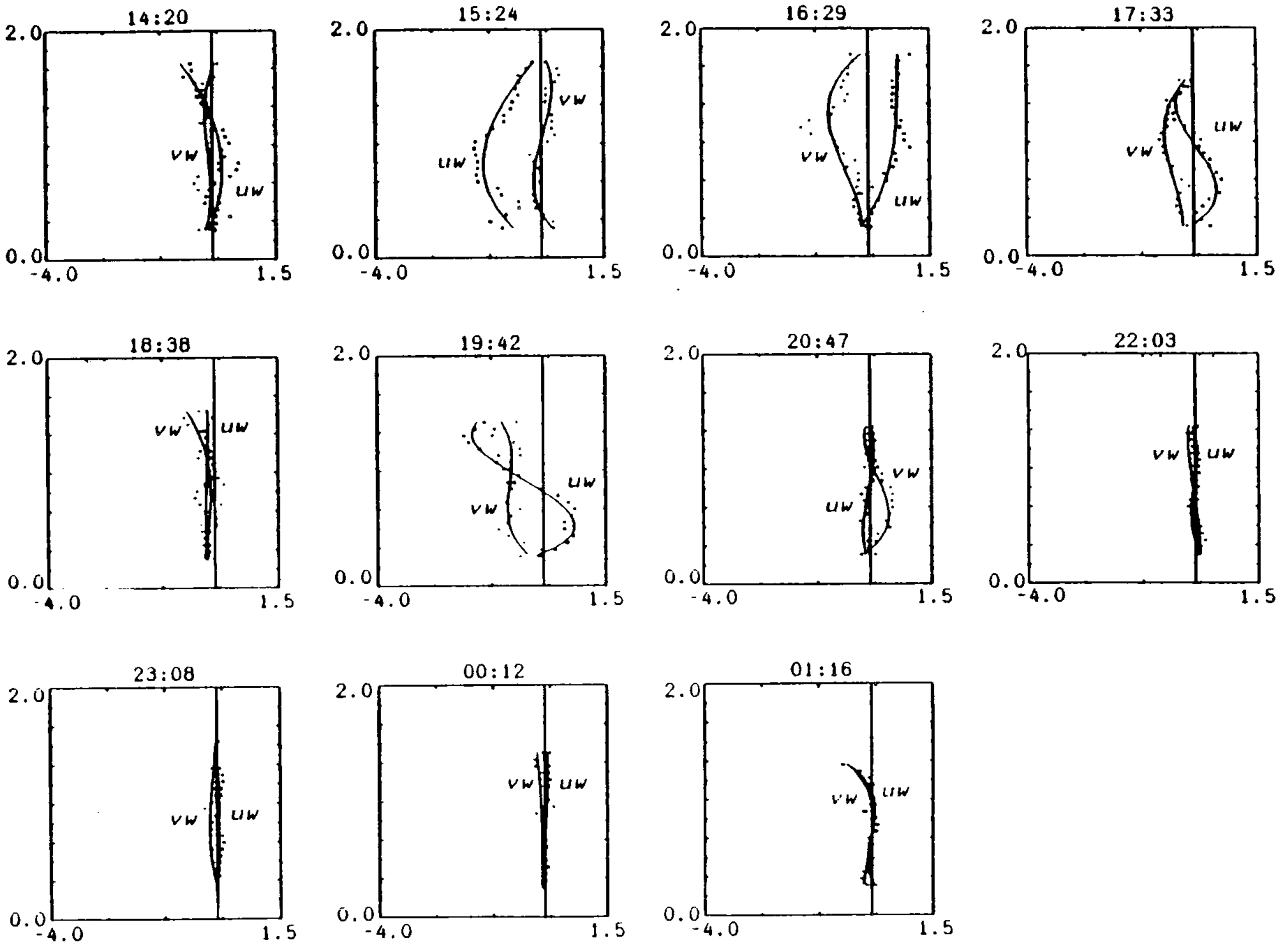

Fig. 17. As in Fig. 15 for $\overline{u'w'}$ and $\overline{v'w'}$. Horizontal scale is m^2s^{-2}.

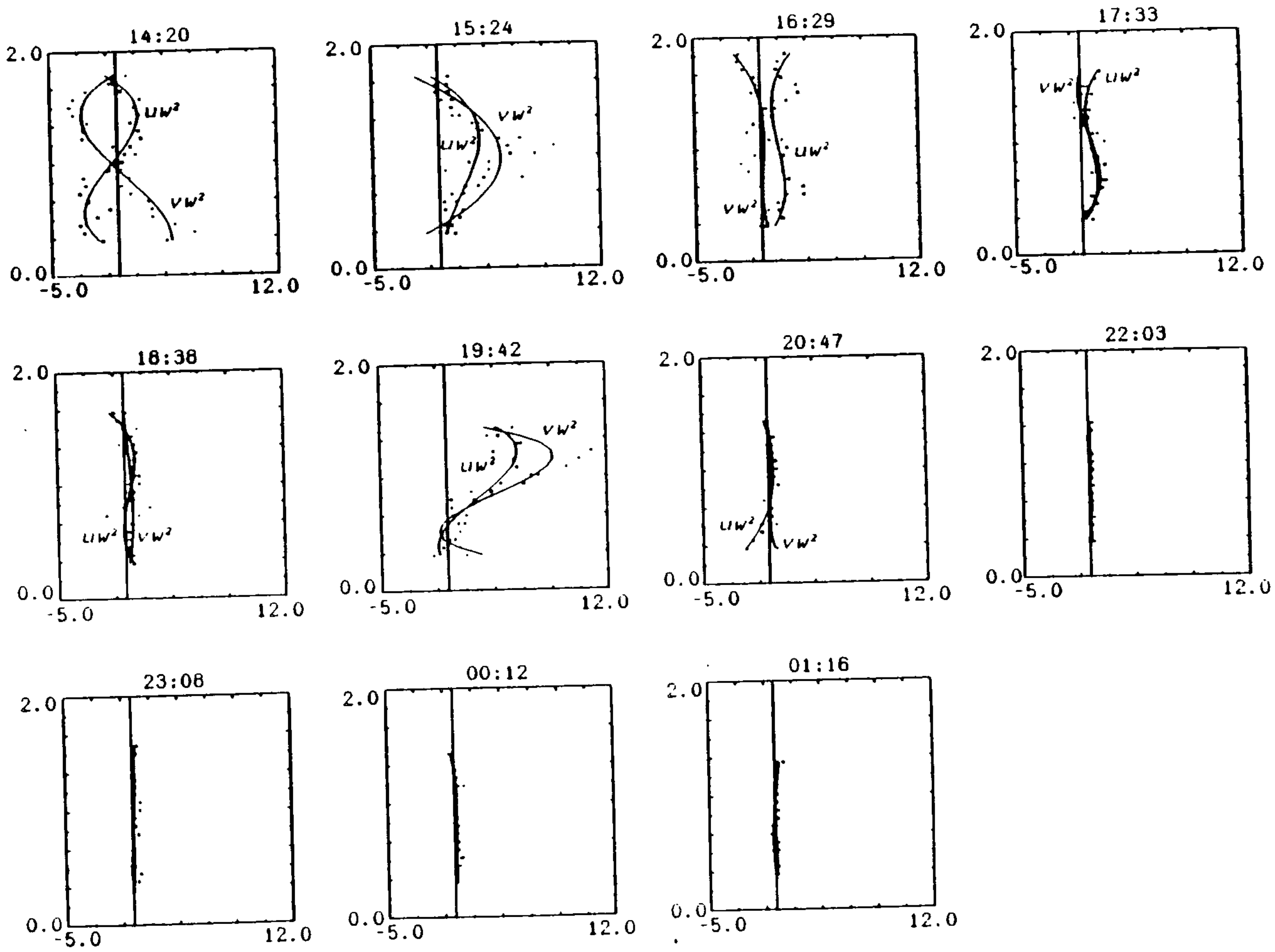

Fig. 18. As in Fig. 15 for $\overline{u'w'^2}$ and $\overline{v'w'^2}$. Horizontal scale is m^3s^{-3}.

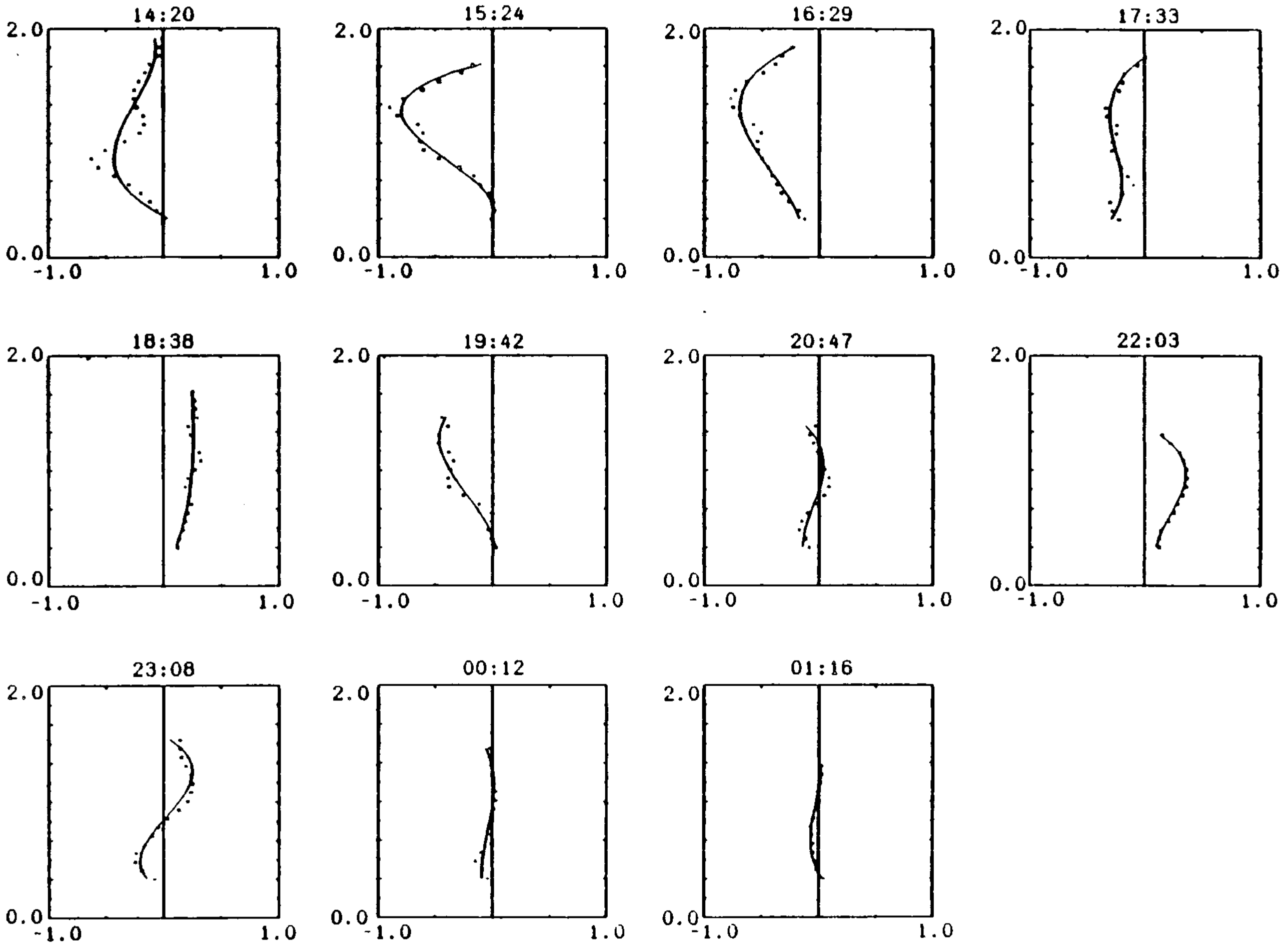

Fig. 19. As in Fig. 15 for vertical velocity. Horizontal scale is ms^{-1}. Negative motions are downward.

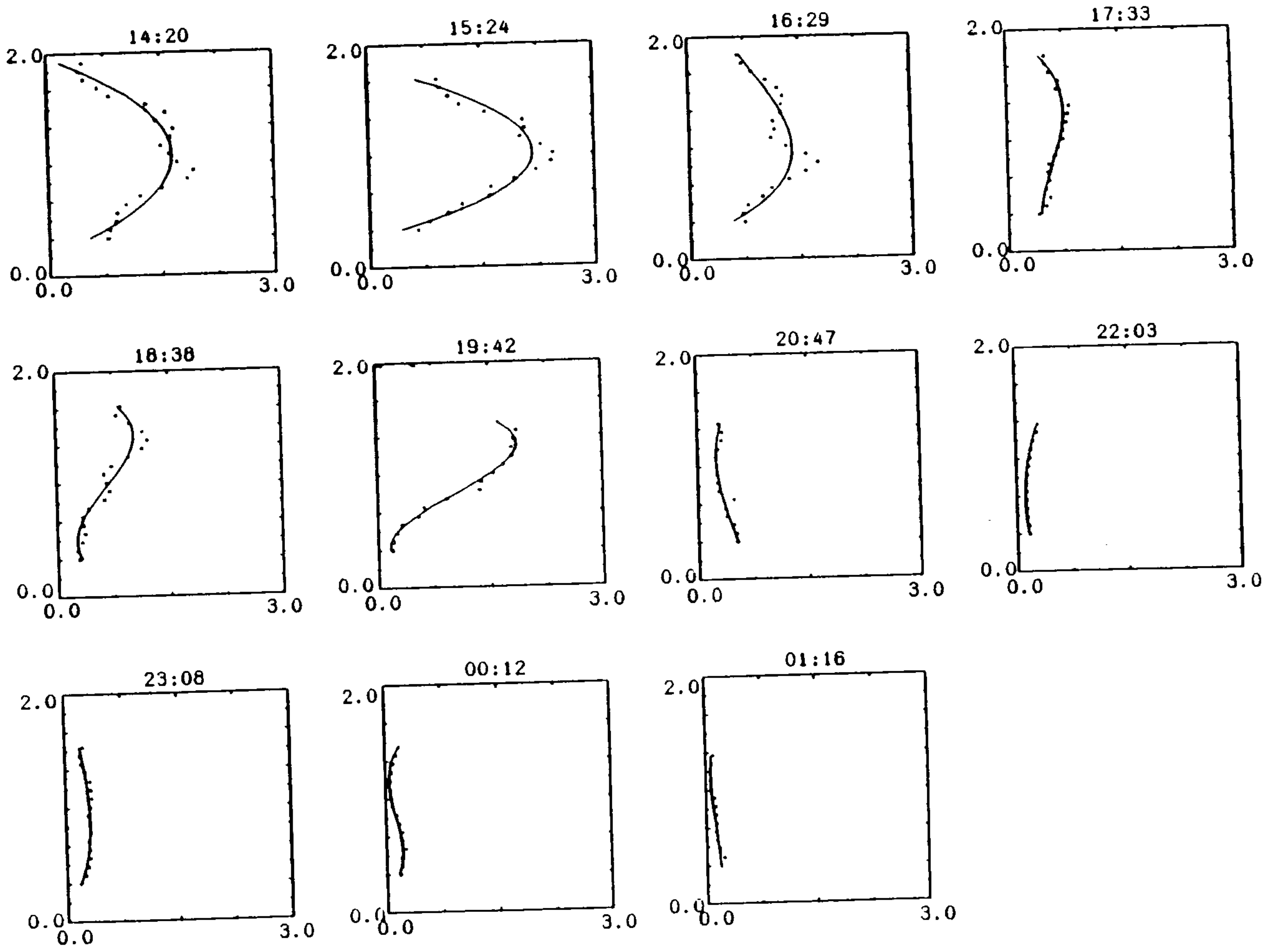

Fig. 20. As in Fig. 15 for vertical velocity variance. Horizontal scale is m^2s^{-2}.

decreased over this period (Fig. 16). At 19:42 CDT an outflow from storms to the southeast caused an abrupt shift in direction to the north and an increase in wind speeds. By 20:14 CDT (not shown) winds had decreased and were now from the southwest again. From 20:47 CDT until the end of the data period the winds slowly turned to the WSW and speeds increased following the development of a low-level nocturnal jet. The height of this jet core increased from 0.6 km at 20:47 CDT to just over 1.1 km at 01:16 CDT. Since nocturnal boundary layer jets typically form near the top of the stable layer this elevation of the jet in time is likely a result of the deepening of the stable layer below the jet.

It is difficult to discriminate between the end of the convective outflow and the onset of the jet development. The rapid change in the wind direction from the south back to the southwest appears to be the end of the outflow so that after the 20:14 CDT average it is assumed the outflow is over. The initial development of the jet begins in the v-component (Fig. 16 at 20:47) which increases until 23:40 CDT. After this time the evolution of the jet appears to be dominated by a turning (presumably inertial turning) rather than any significant increase in speed.

The stress profiles (Fig. 17) on 1-2Jul89 have moderate magnitudes at 14:20 CDT with peaks around 1 $\mathrm{m^2s^{-2}}$ which increase to 1.5 $\mathrm{m^2s^{-2}}$ by 15:24 CDT. After 16:29 CDT there is a gradual decrease in the stress values which reach a minimum of around 0.5 $\mathrm{m^2s^{-2}}$ at 18:38 CDT. The storm outflow produces a significant increase in the stresses with values as large as 2 $\mathrm{m^2s^{-2}}$ at 19:42 CDT. After this time they rapidly decreased and by 20:47 were below ± 0.5 $\mathrm{m^2s^{-2}}$. They remained near this value through the rest of the data period.

The terms $\overline{u'w'^2}$ and $\overline{v'w'^2}$ (Fig. 18) also have rather large values (± 4 $\mathrm{m^3s^{-3}}$) between 14:20 and 16:29 CDT after which there is a gradual decrease before the outflow reaches the radar site. During the outflow values of 8 $\mathrm{m^3s^{-3}}$ are observed.

These turbulent transport terms then decreased rapidly becoming small for the remainder of the data period (less than 0.5 m^3s^{-3}).

The vertical velocity and vertical velocity variance (Figs. 19 and 20) exhibit behavior similar to the other statistics with the largest values observed before 16:29 CDT followed by a gradual decrease before the convective outflow. Large values are again observed during the outflow followed by a rapid decrease. Values of both $\bar{w}$ and $\overline{w'^2}$ remain small through the rest of the data period.

The vertical velocity variance profiles are fairly typical of a convective PBL. There are however some interesting features in the vertical velocity field. Negative values (downward motion) of $\bar{w}$ are observed until just before the convective outflow at which time they become positive. During the outflow $\bar{w}$ becomes negative again until the jet begins forming around 20:47 CDT. After this time $\bar{w}$ is generally positive near the jet core and negative closer to the surface. Dynamic forcing of the jet could induce these positive vertical motions while negative $\bar{w}$ could be the result of subsidence within the developing nocturnal boundary layer.

ii. Evolution of Turbulence Momentum Budget

The momentum budgets corresponding to the time period in Figs. 15-20 are illustrated in Figs. 21-29. The vertical scale in each of these plots has been scaled to the maximum value of the terms within the budget. This was done in order that the relative magnitudes of each term in the budget can be seen even after turbulent activity has decreased (e.g. within the nocturnal boundary layer.) This was necessary since without other supporting meteorological data it was not possible to derive accurate scaling parameters. Positive values on the plots represent sinks for positive momentum (as a result of the sign of the terms in (2) and (3)) and sources for negative momentum. The reverse is true for negative values on the plots.

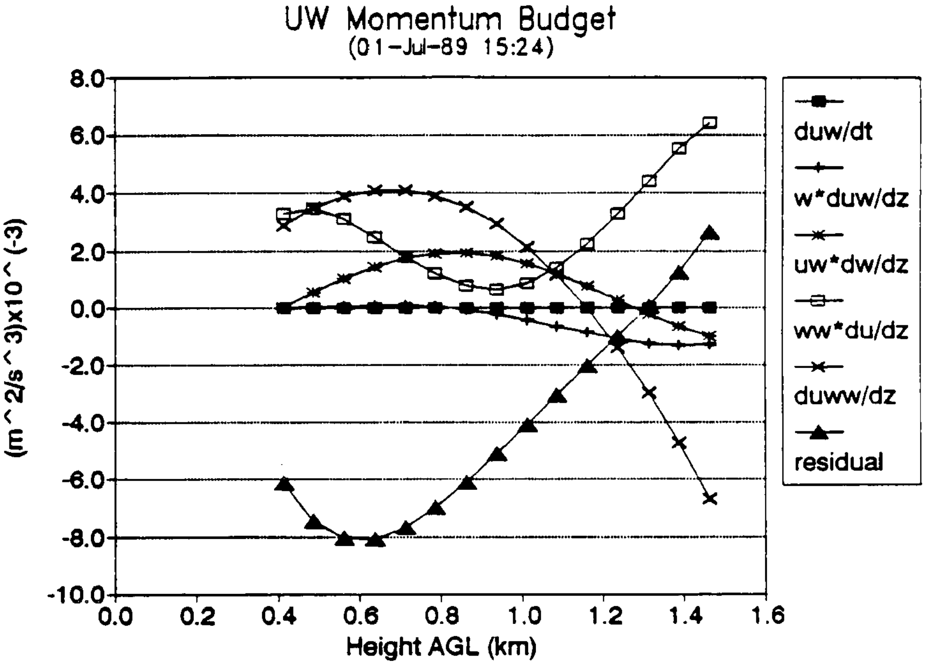

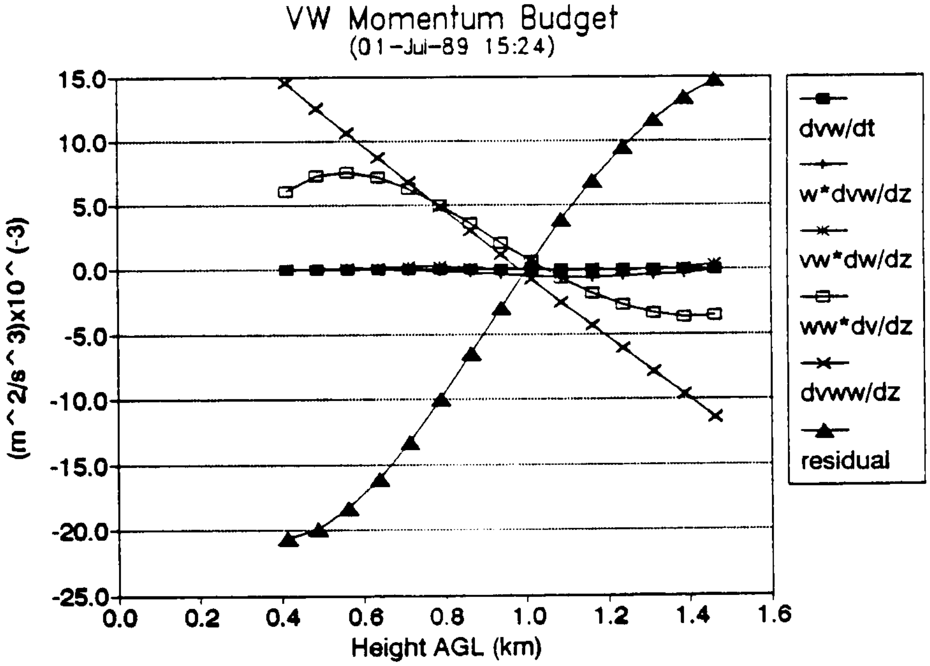

Fig. 21. Horizontal turbulent momentum flux budgets for 1Jul89 at 15:24 CDT. Terms are derived from the one hour average best-fit plots in Figs. 15-20. The residual is the sum of all the derived terms.

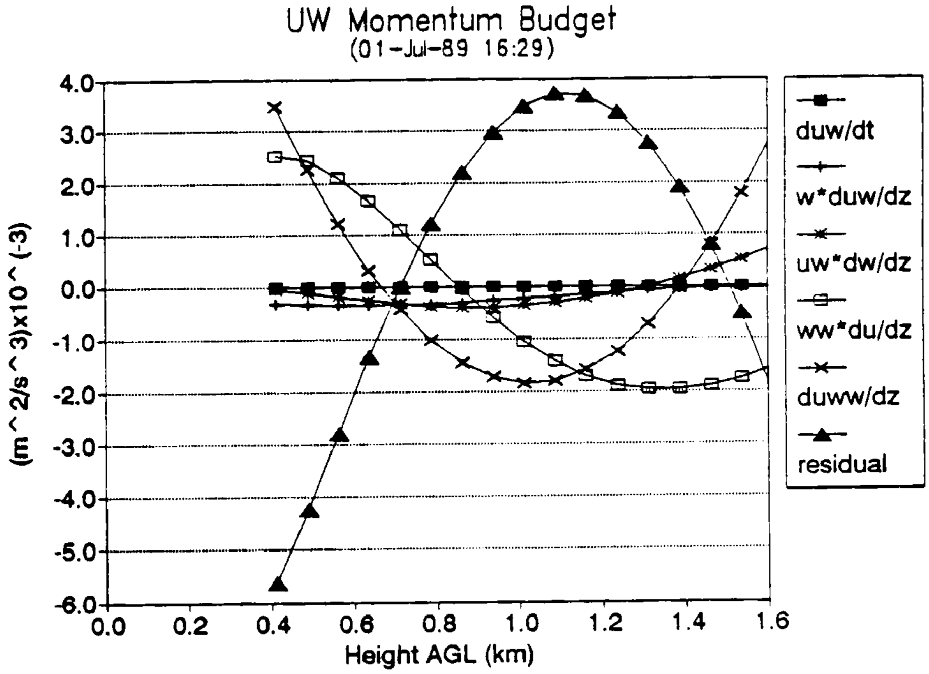

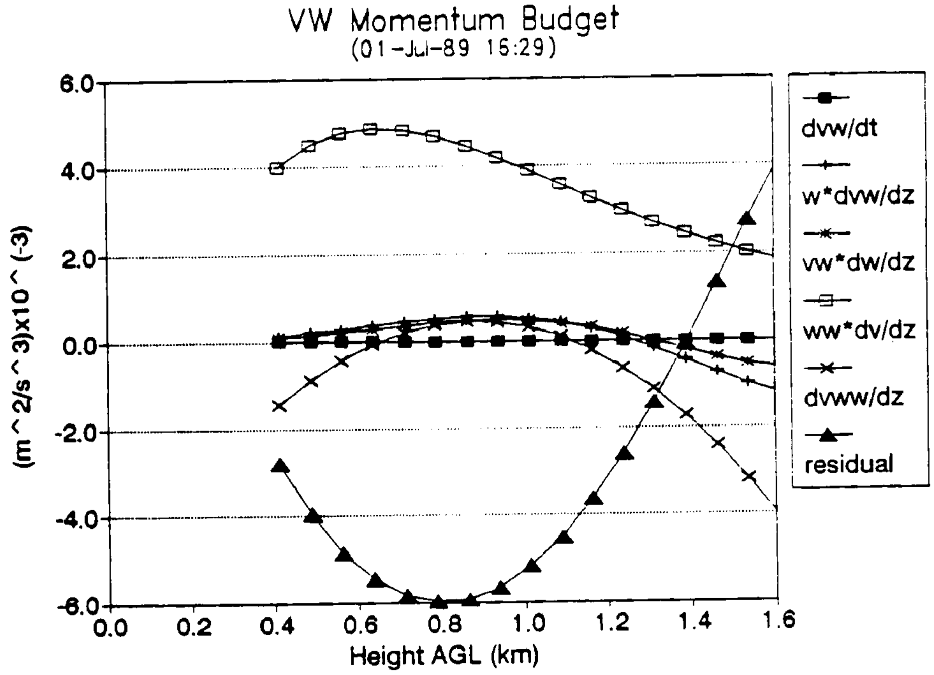

Fig. 22. As in Fig. 21 for 1Jul89 at 16:29 CDT.

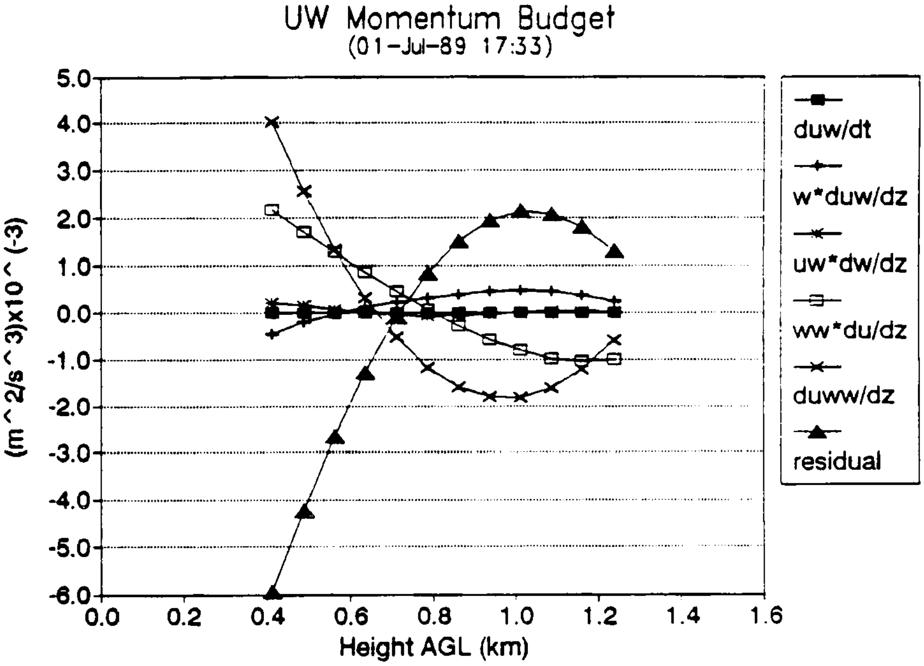

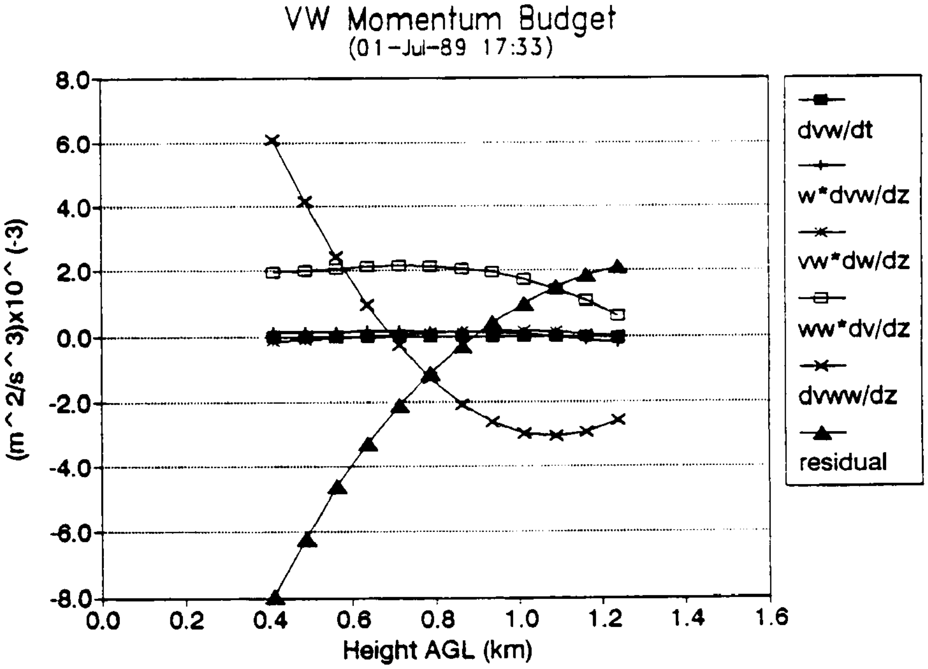

Fig. 23. As in Fig. 21 for 1Jul89 at 17:33 CDT.

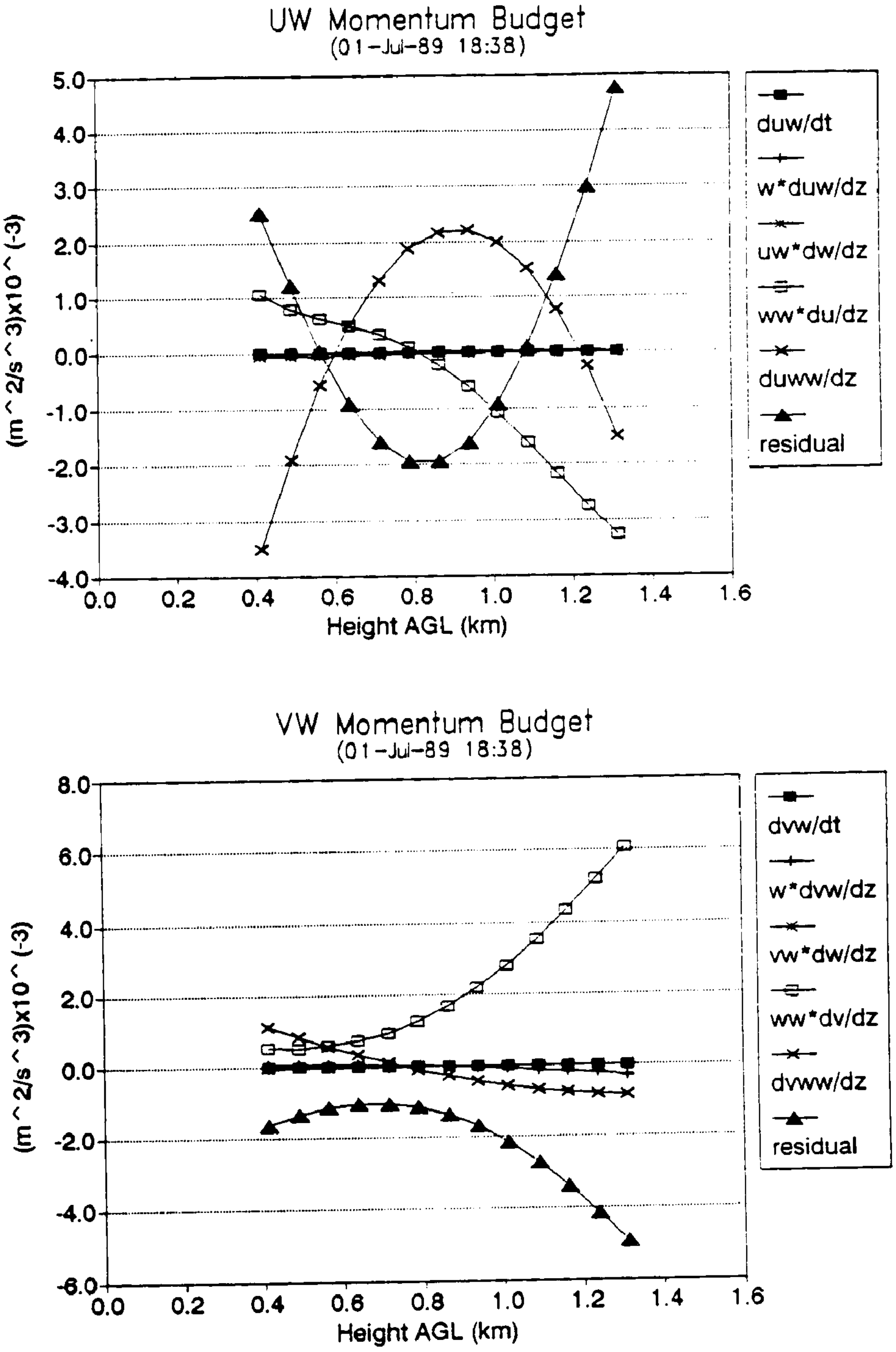

Fig. 24. As in Fig. 21 for 1Jul89 at 18:38 CDT.

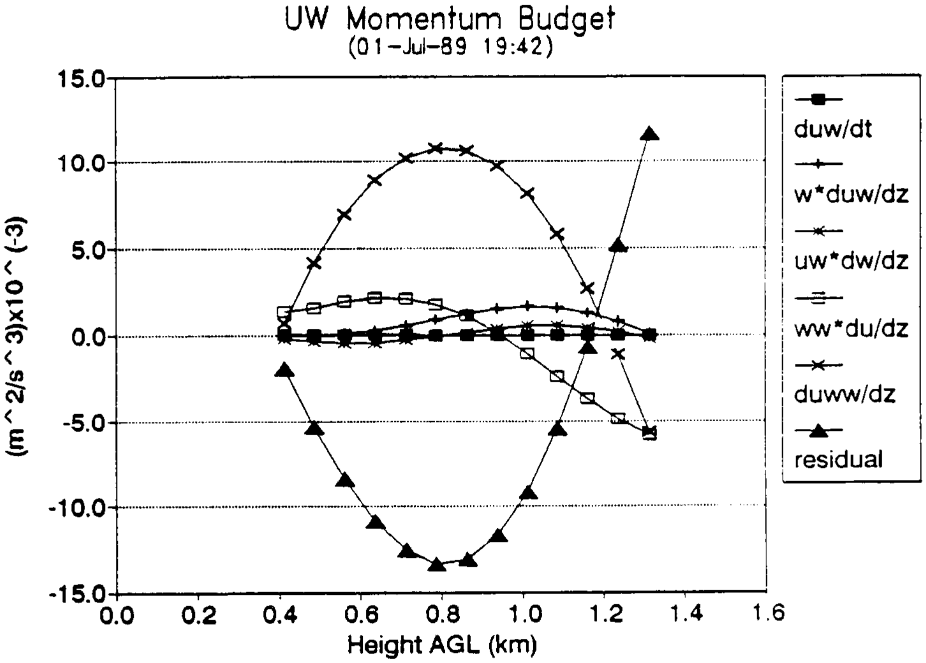

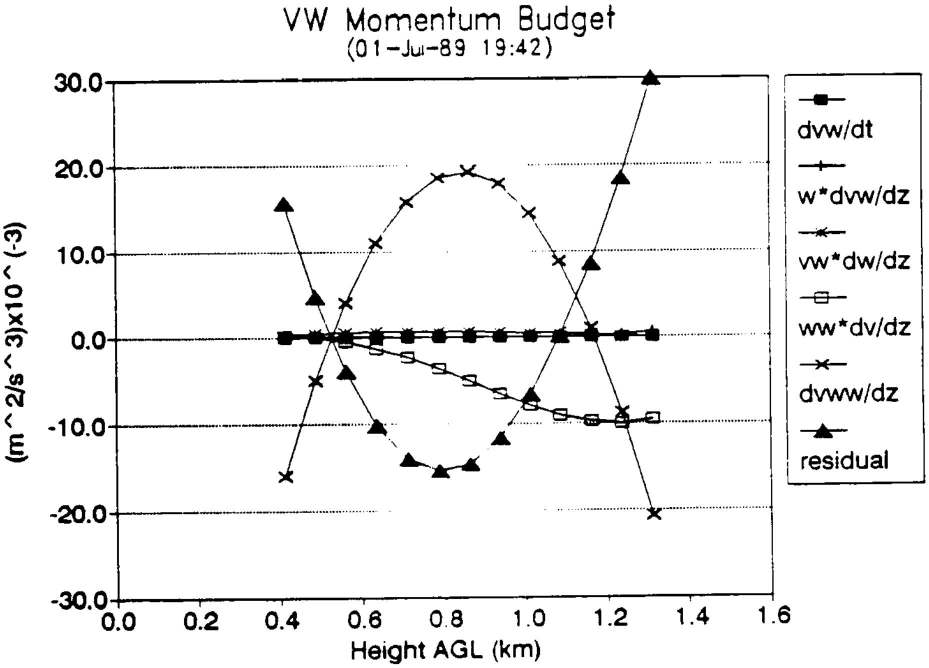

Fig. 25. As in Fig. 21 for 1Jul89 at 19:42 CDT.

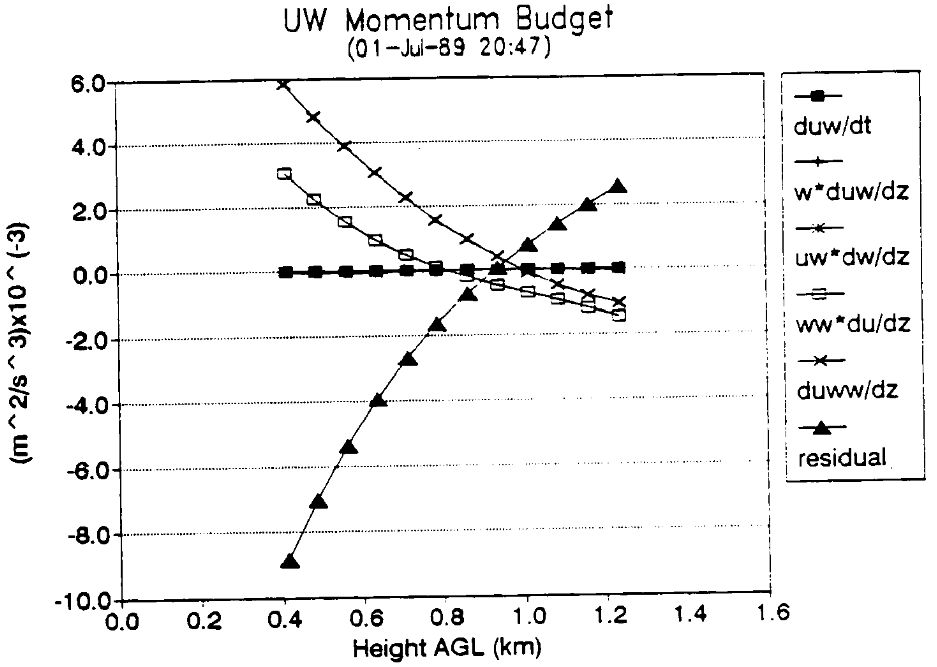

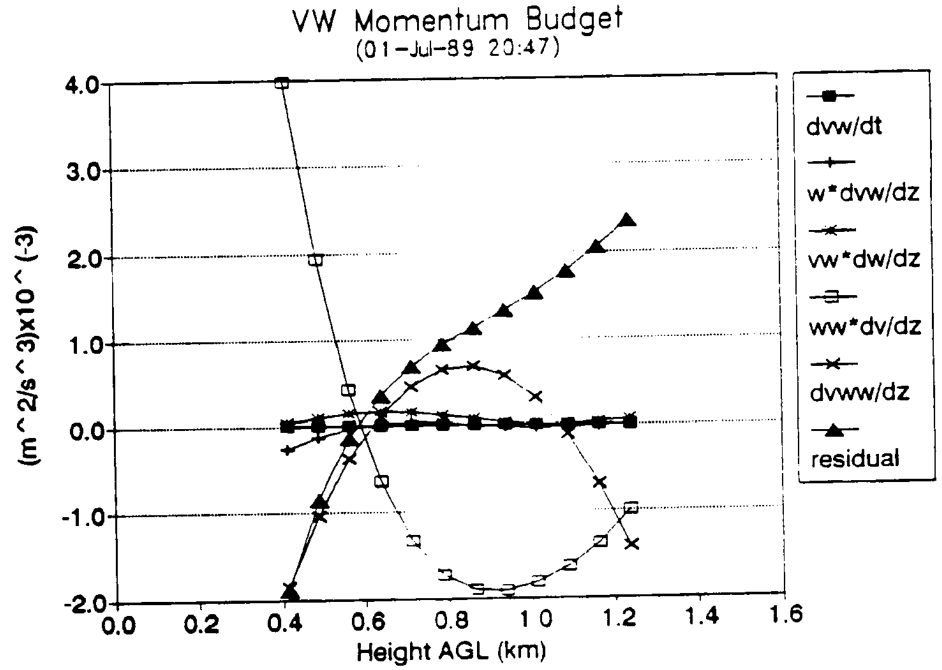

Fig. 26. As in Fig. 21 for 1Jul89 at 20:47 CDT.

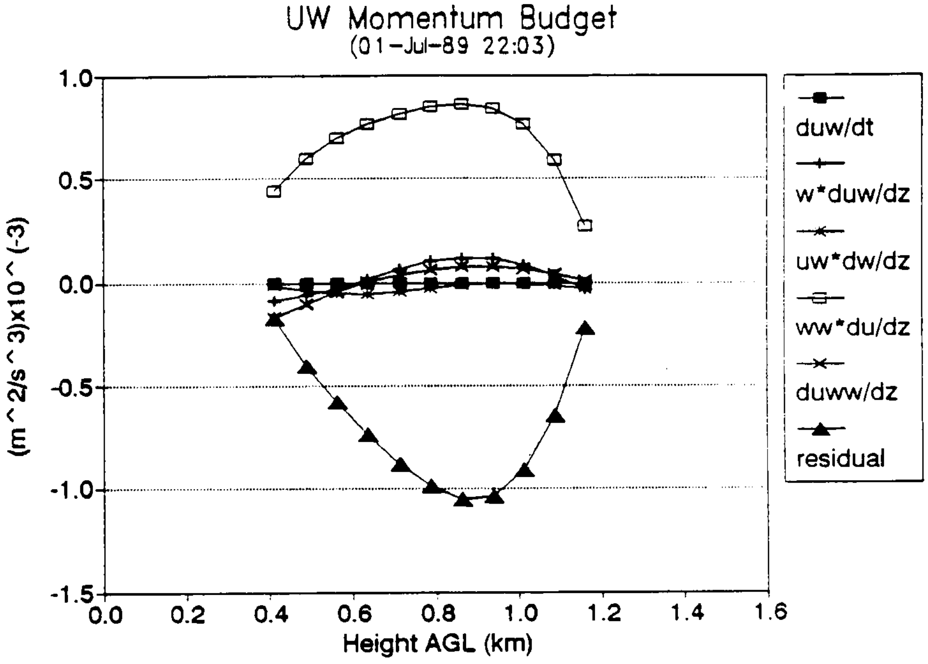

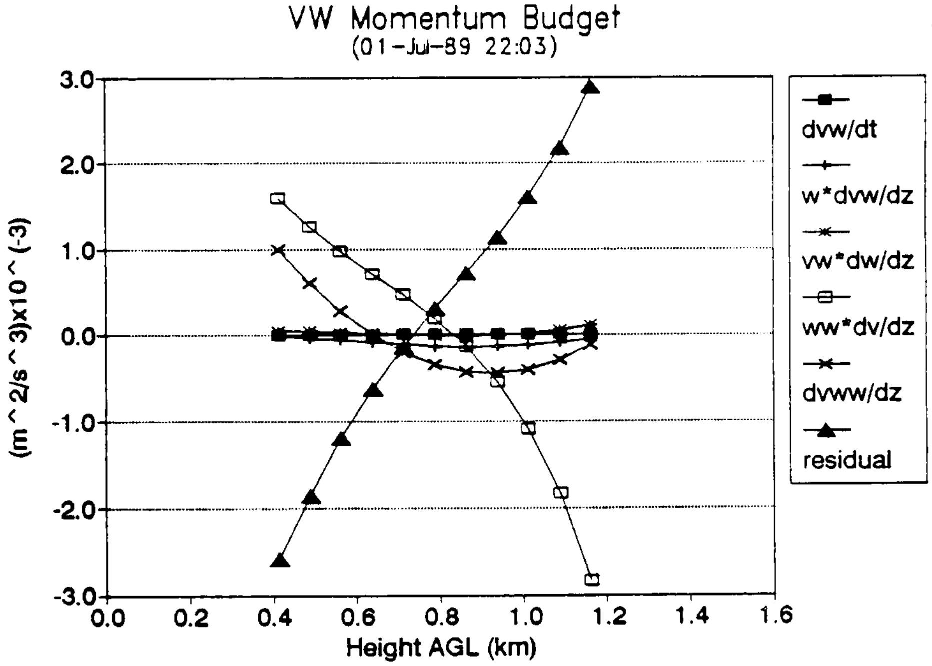

Fig. 27. As in Fig. 21 for 1Jul89 at 22:03 CDT.

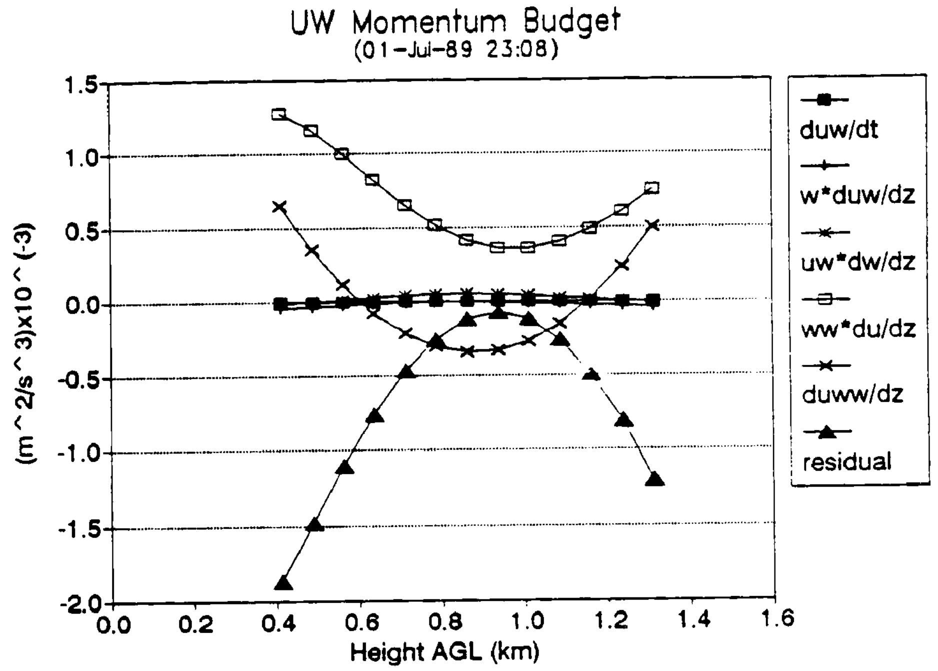

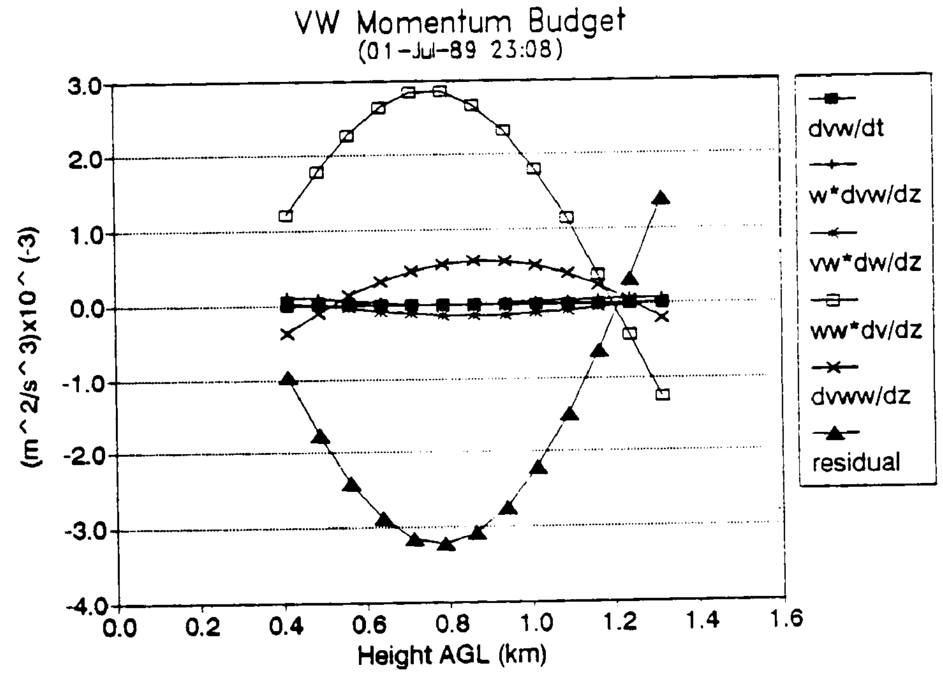

Fig. 28. As in Fig. 21 for 1Jul89 at 23:08 CDT.

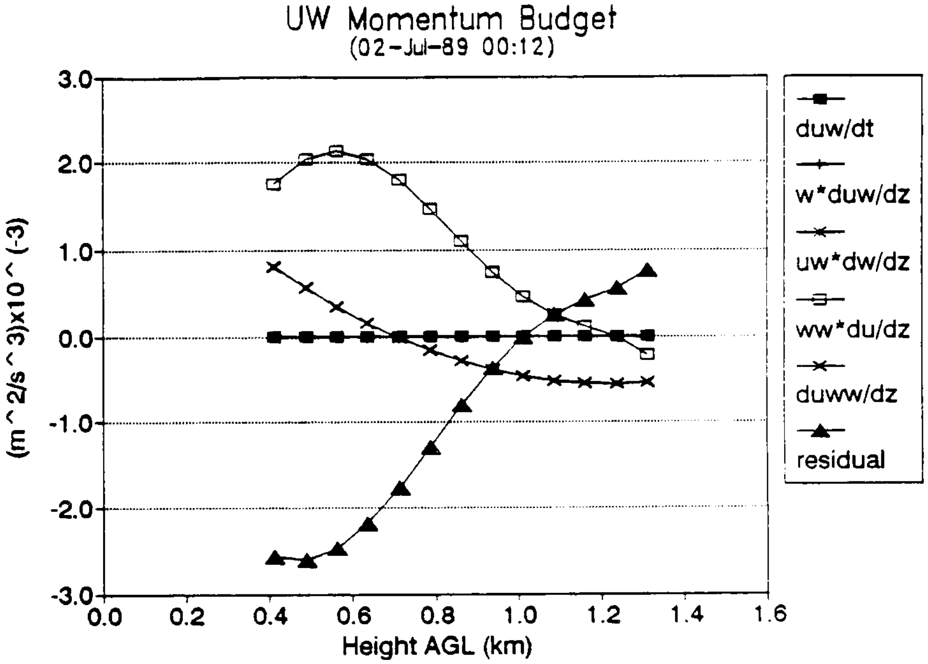

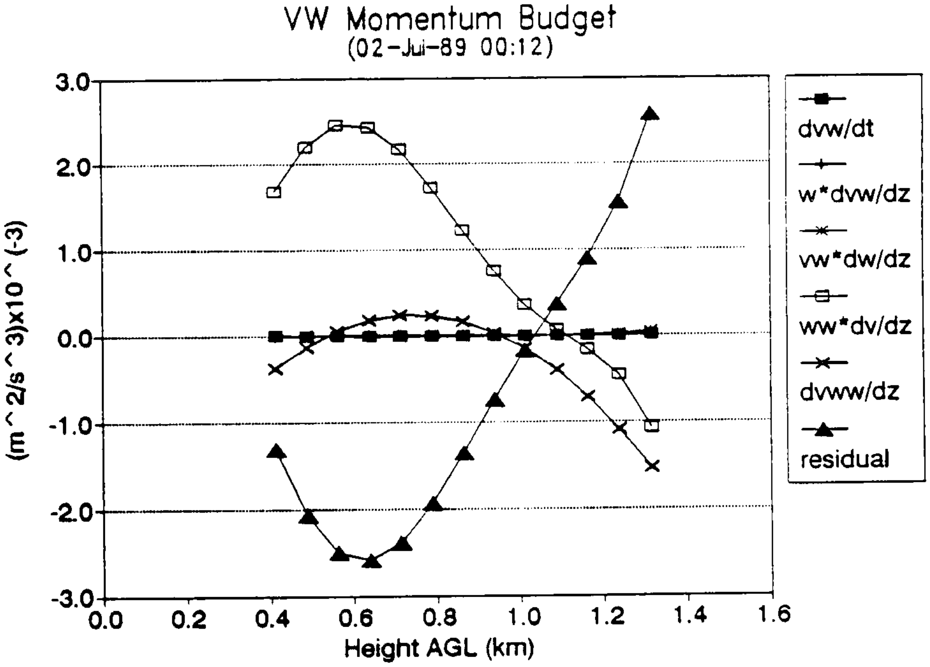

Fig. 29. As in Fig. 21 for 2Jul89 at 00:12 CDT.

The first term in equations (2) and (3) is the local time change of the stress. This was shown in a scale analysis by Wyngaard (1983) to be negligible relative to other terms in the budget as were the mean advections. The local time change of stress and vertical advection terms were carried through in this analysis since they were straight forward to compute. As seen in Figs. 21-29 the temporal changes in the stresses were always several orders of magnitude less than other terms in the budget which supports the theoretical work of Wyngaard (1984). The advection by $\bar{w}$ was not always negligible. Although it was typically much smaller than turbulent transport or shear production, magnitudes of greater than 0.5×10^{-3} m^2s^{-3} were not uncommon during the daytime (Fig. 23). A maximum value of over 1.5×10^{-3} m^2s^{-3} was observed during the outflow event at 19:42 CDT (Fig. 25). During the night it was typically negligible (e.g. Fig. 28).

The third term in (2) and (3) is the production of momentum flux due to shear in $\bar{w}$. This term was comparable in magnitude to the advective production by $\bar{w}$. Occasionally values near 0.5×10^{-3} m^2s^{-3} were observed during the daytime (Fig. 22). A maximum of nearly 2×10^{-3} m^2s^{-3} was observed at 15:24 CDT (Fig. 21). Nighttime values were much smaller, typically $\pm 0.1 \times 10^{-3}$ m^2s^{-3} or less (Fig. 29) and could be neglected.

Production of momentum flux by shear in the horizontal wind is the forth term in (2) and (3). This is a dominant term throughout the data period. Maximum daytime magnitudes were $\pm 6 \times 10^{-3}$ m^2s^{-3} (Fig. 21). Nighttime values were generally $\pm 3 \times 10^{-3}$ m^2s^{-3} or less (Fig. 28). Between 14:20 CDT (not shown) and 16:29 CDT (Fig. 22) this term was nearly a constant source of momentum flux. As the absolute magnitude of turbulence began to decrease it was more difficult to classify and seemed to alternate between a source and a sink term. During the night shear production became the dominant term in (2) and (3) (Fig. 28).

The final term which can be solve for in (2) and (3) from the radar data is the turbulent transport of momentum flux. This term cannot be classified as a distinct source or sink term. It has characteristics more like a redistribution term typically being a source at one level and a sink of momentum flux at another. This was the dominant term during the daytime with a maximum of 10×10^{-3} m^2s^{-3} or greater being common between 15:24 CDT (Fig. 21) and 16:29 CDT (Fig. 22). The extreme values at 19:42 CDT (see Figs. 18 and 25) may be the result of a poor data fit. Between 16:29 CDT and the outflow passage at 19:42 CDT typical values were $\pm 4 \times 10^{-3}$ m^2s^{-3} (Fig. 24). Nighttime values decreased significantly with $\pm 0.5 \times 10^{-3}$ m^2s^{-3} becoming common after 22:03 CDT (Figs. 28 and 29).

The residual (the sum of all the terms in the first line of (2) and (3)) is also contained in Figs. 21-29. This is the net contribution from the buoyancy, pressure and dissipation terms. This term therefore follows the same overall trends as the other turbulence statistics. Before 16:29 CDT values of $\pm 15 \times 10^{-3}$ m^2s^{-3} are common (Fig. 21). These decrease to $\pm 5 \times 10^{-3}$ m^2s^{-3} before the outflow passage (Fig. 24). Peaks around $\pm 15 \times 10^{-3}$ m^2s^{-3} are common during the outflow event (Fig. 25) followed by a rapid decrease to values around $\pm 3 \times 10^{-3}$ m^2s^{-3} (Fig. 27) by the end of data collection.

6b. NDTP 27-28Jun89

i. Evolution of Statistical Turbulence Profiles

Figures 30-35 are a time series of the statistical profiles used to derive the momentum flux budgets on 27-28Jun89. The mean winds (Fig. 30) are more uniform than 1-2Jul89. There is a general linear slope in the profiles but no significant curvature. Winds are from the ESE at 9 ms^{-1} at 16:57 CDT increasing to 12 ms^{-1} by 18:01 CDT (Fig. 31). A low-level jet also forms on this day. Evidence of formation begins around 19:05 CDT and slowly turns and accelerates reaching a maximum of nearly 23 ms^{-1} at the end of the data period. The jet

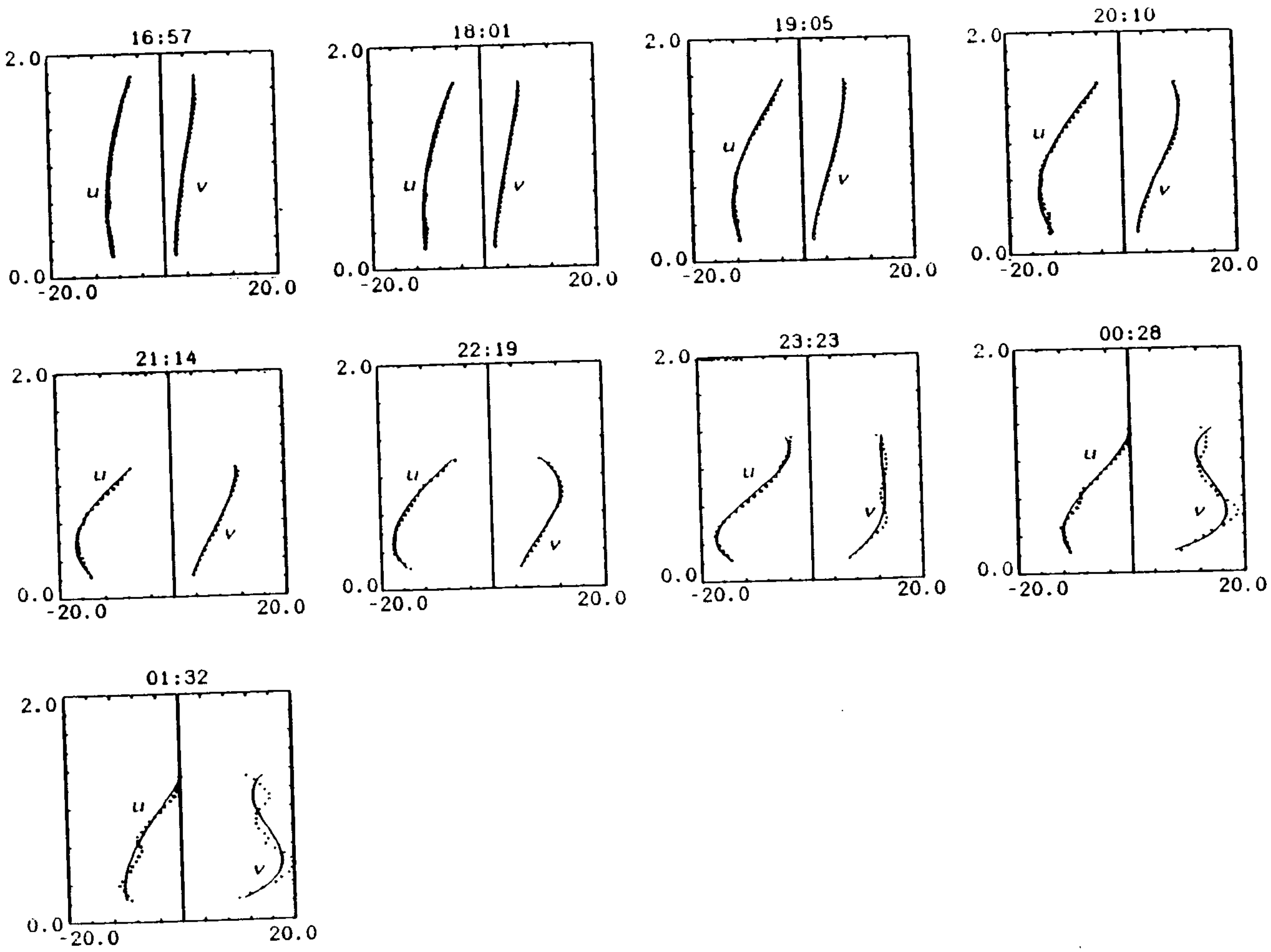

Fig. 30. Time series analysis of mean wind components for 27-28Jun89. Vertical scale is km and horizontal scale is ms^{-1}. All plots are from an eight volume scan average (64 minutes).

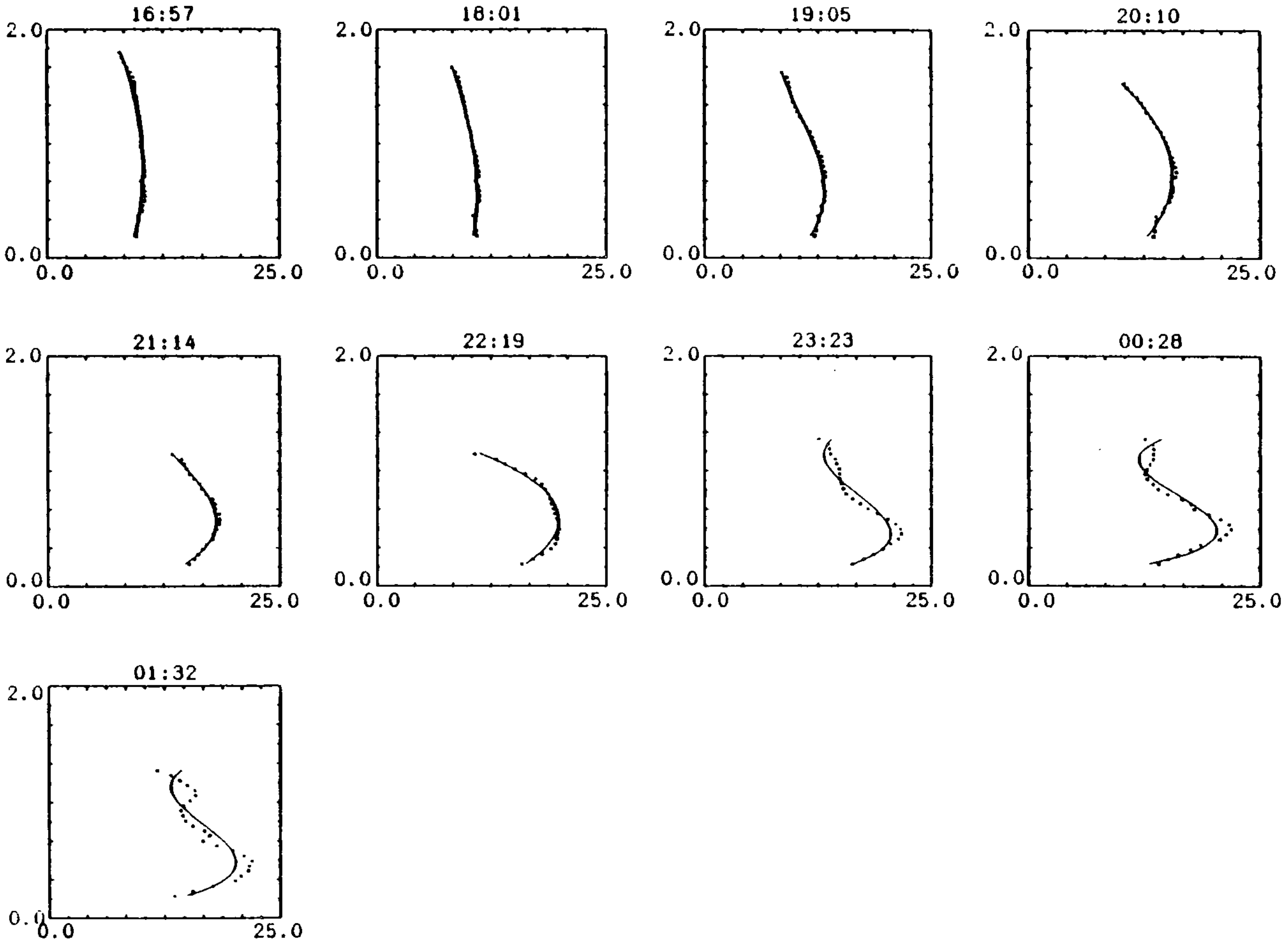

Fig. 31. As in Fig. 30 for wind speed. Horizontal scale is ms^{-1}.

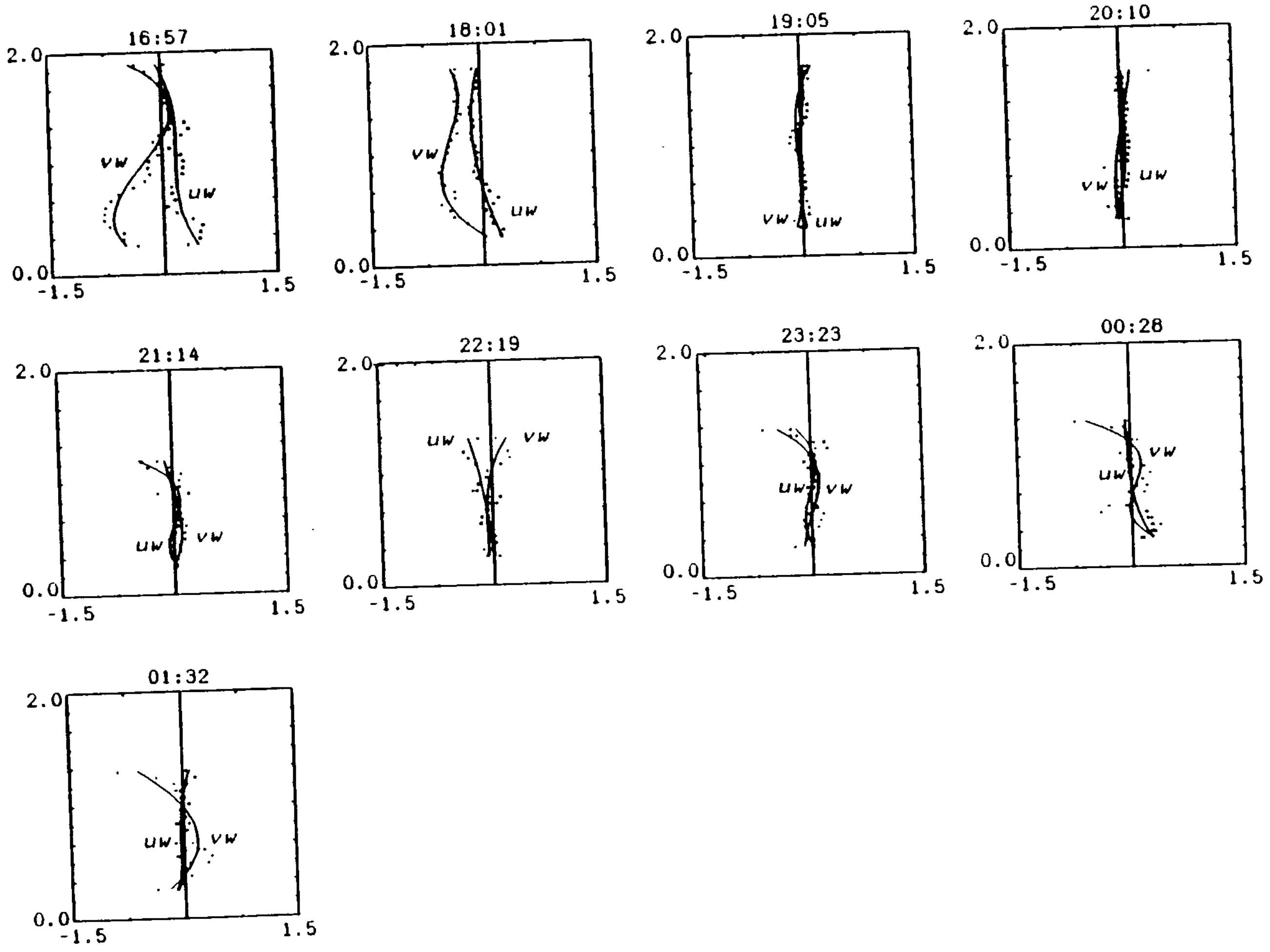

Fig. 32. As in Fig. 30 for $\overline{u'w'}$ and $\overline{v'w'}$. Horizontal scale is m^2s^{-2}.

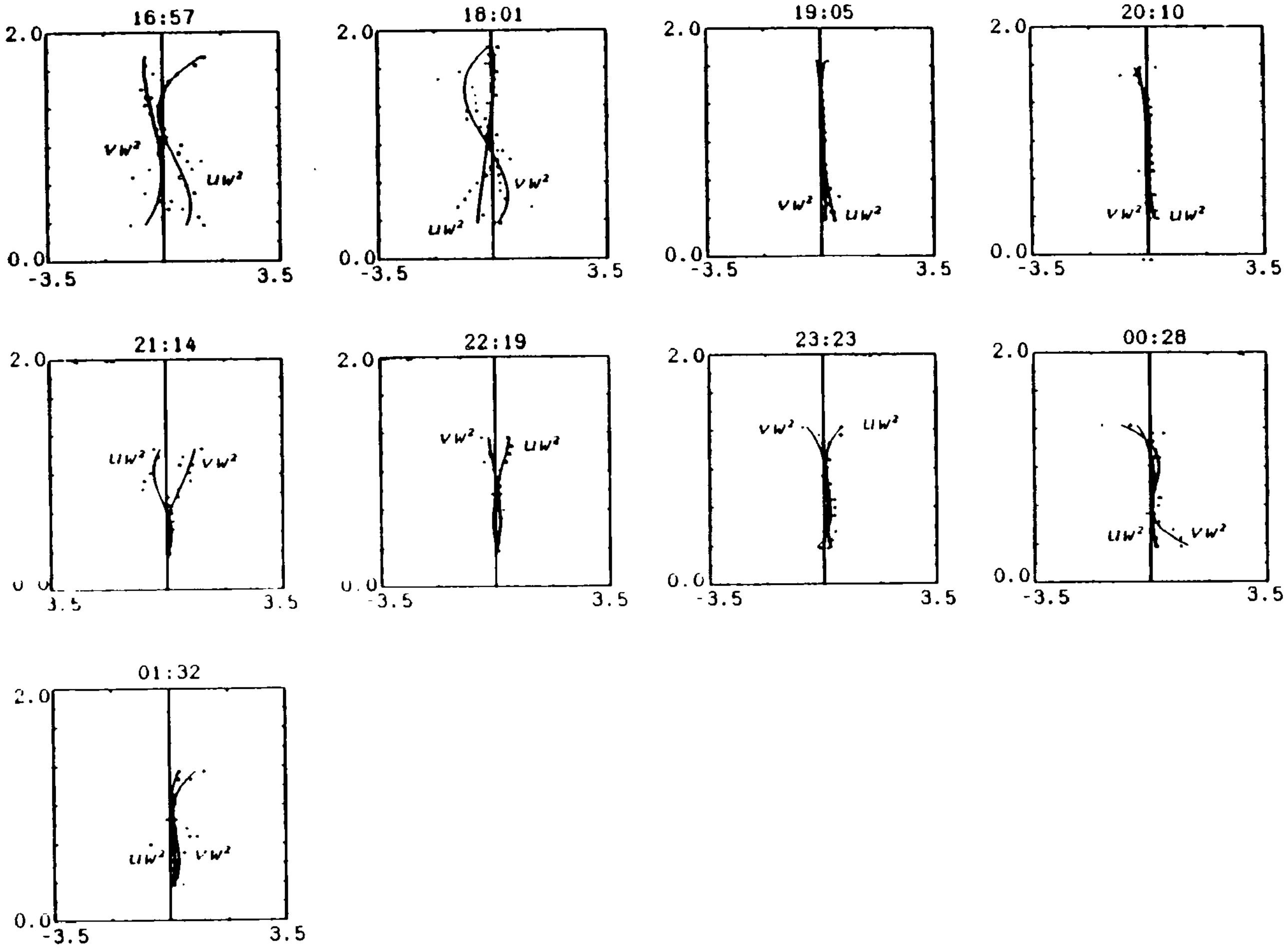

Fig. 33. As in Fig. 30 for $\overline{u'w'^2}$ and $\overline{v'w'^2}$. Horizontal scale is m^3s^{-3}.

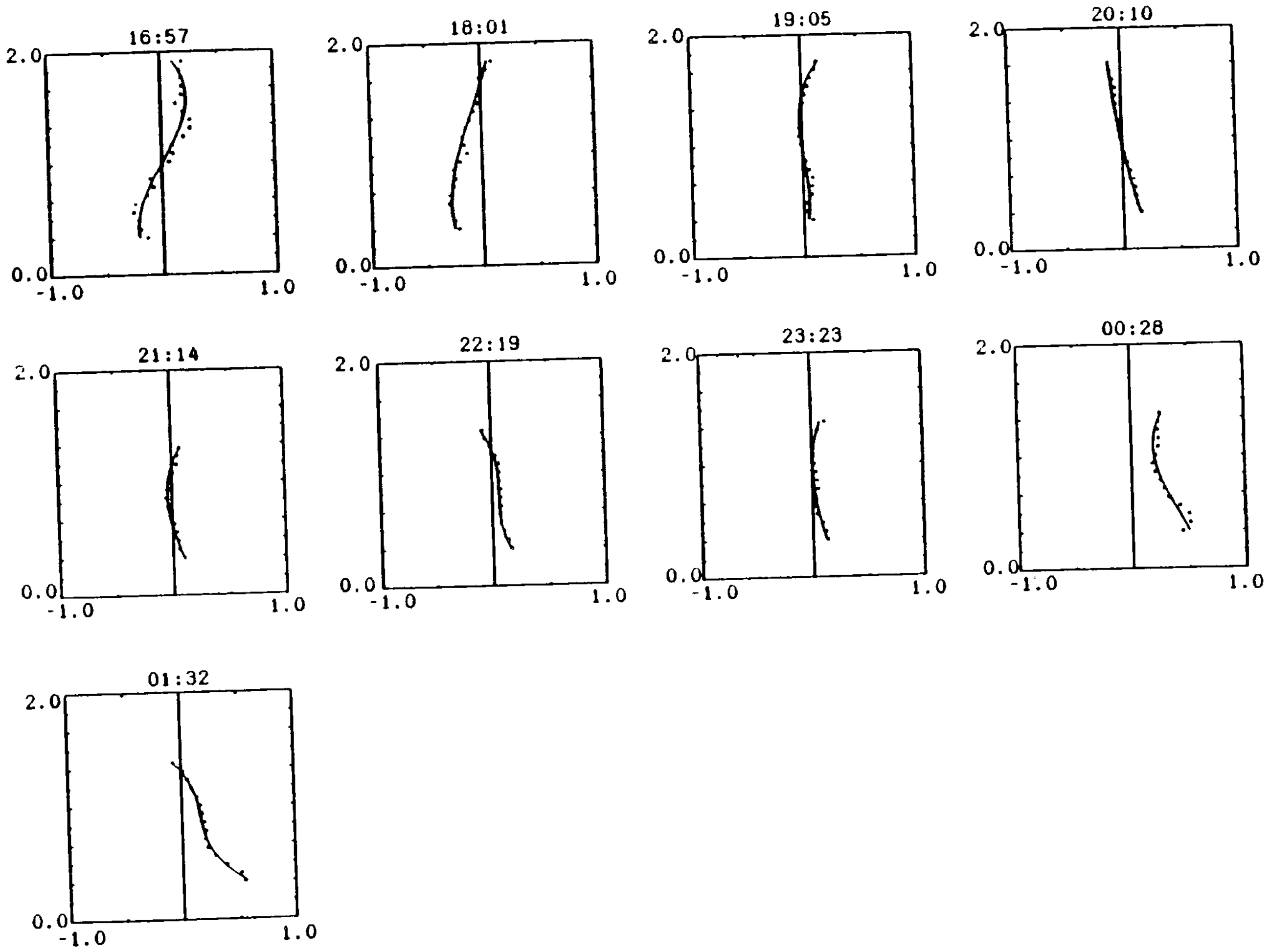

Fig. 34. As in Fig. 30 for vertical velocity. Horizontal scale is ms^{-1}. Negative motions are downward.

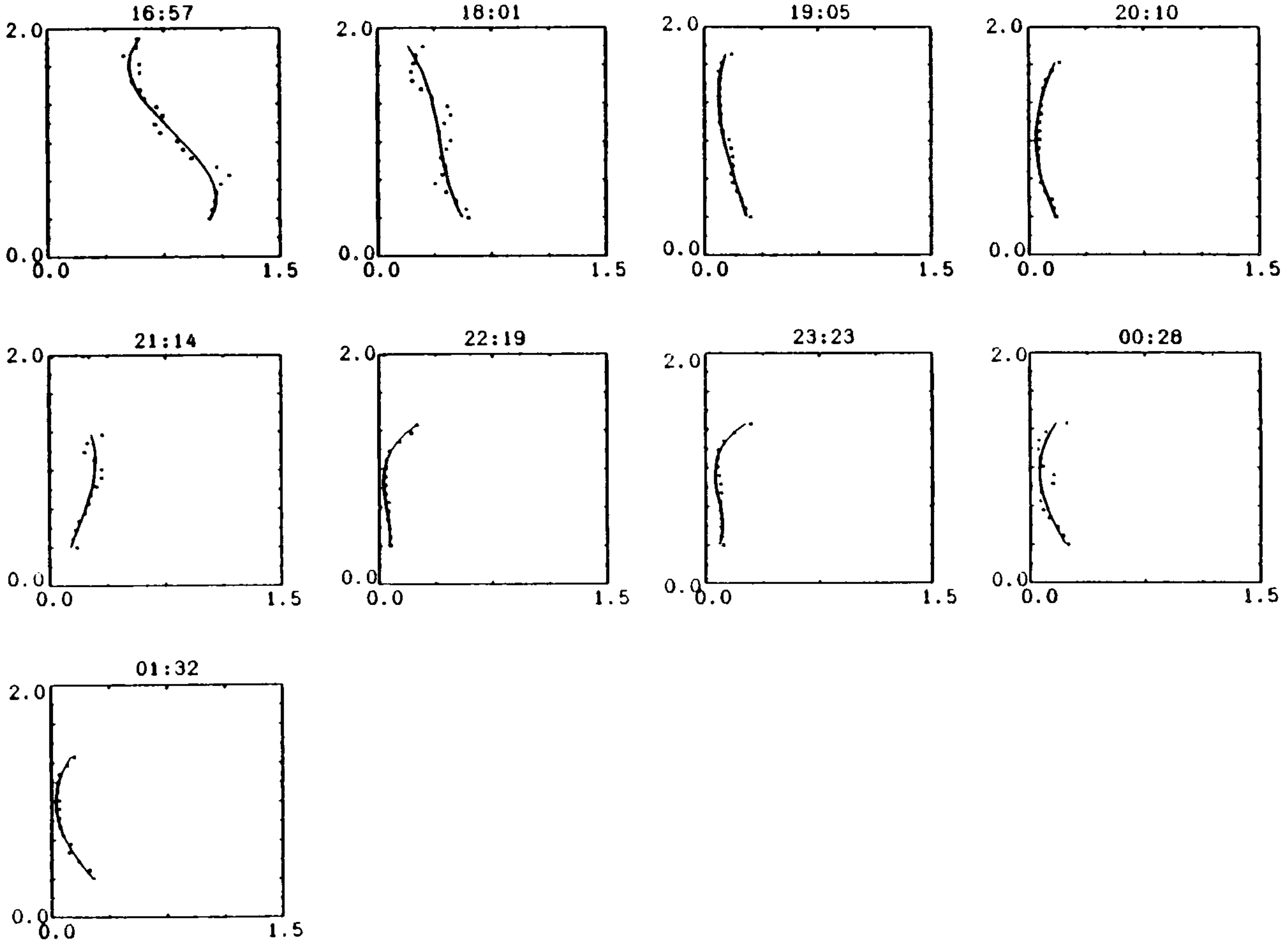

Fig. 35. As in Fig. 30 for vertical velocity variance. Horizontal scale is m^2s^{-2}.

core stays at a relatively constant height of 500 m throughout it's evolution. There appears to be a secondary core which develops at 1.1 km between 00:28 CDT and 01:32 CDT on 28Jun89. Using only a third-order polynomial data fit, this secondary maximum in the wind speed tends to degrade the data fit slightly although it is still good enough to derive reasonable wind gradients below 1 km AGL.

Magnitudes of the stress profiles (Fig. 32) are ±1 m^2s^{-2} for the first hour of the data period. The high temperature of 91F was reached at 1550 CDT. This data therefore begins just after the maximum in surface heating has been reached such that the intensity of turbulence begins decreasing relatively quickly (within approximately one hour). After 18:01 CDT stresses remain less than ±0.5 m^2s^{-2}.

The turbulent transport of momentum flux (Fig. 33) is a maximum during the first hour average with values greater than 2 m^3s^{-3}. It then begins steadily decreasing and after 18:01 CDT remains within ±0.5 m^3s^{-3}

Between 16:57 CDT and 19:05 CDT $\bar{w}$ has a tendency for negative values at low altitudes and positive values above (Fig. 34). From 19:05 CDT until 22:19 CDT these characteristics reverse to positive at low levels and negative at higher altitudes. After 22:19 CDT there is a general tendency for positive values at all heights. These tendencies in $\bar{w}$ seem to be related to the development of the low-level jet. In the initial stages of development $\bar{w}$ is positive at and below the level of the jet maximum. As the jet intensifies $\bar{w}$ tends to be positive below and above the main jet maximum. As mentioned above there is evidence of a secondary jet maximum above the main jet which may also be inducing positive vertical motions. Magnitudes of $\bar{w}$ are around 0.5 ms^{-1} during the first hour and then gradually decline. During the intensification of the jet (22:19 CDT to the end of data collection) $\bar{w}$ increases reaching a maximum of slightly over 0.5 ms^{-1} in the lowest levels. The variance in vertical velocity (Fig. 35) peaks during the first hour of observations and then steadily declines. During the intensification of the jet there is a gradual increase in $\overline{w^2}$ below the level of the jet maximum however peak values are still relatively small (0.3 m^2s^{-2}).

ii. Evolution of Turbulence Momentum Budget

Solutions for the momentum flux budgets from 27-28Jun89 are in Figs. 36-43. The temporal changes, production due to advection by $\bar{w}$ and shear production by $\bar{w}$ are generally negligible over the entire data period. The only exception is at the end of the period where the jet induced $\bar{w}$ becomes large enough that mean advection by $\bar{w}$ is a minor constituent of the momentum flux budget. The largest values of this term are near 0.4×10^{-3} m^2s^{-3} (Fig. 43).

Shear production was the dominant term on 27-28Jun89. It remained relatively constant throughout the period. Magnitudes ranged between $\pm 3 \times 10^{-3}$ m^2s^{-3} during the first few hours (Figs. 36 and 37) and slowly decreased from 19:05 to 20:10 CDT (Figs. 38 and 39). There were large peaks at 21:14 CDT (Fig. 40) of 7×10^{-3} m^2s^{-3} followed by a generally decreasing trend to $\pm 2 \times 10^{-3}$ m^2s^{-3} during the later part of the data period (Fig. 42). The shapes of the profiles were relatively stable, remaining fairly constant over a number of averaging periods or changing very slowly.

The turbulent transport of momentum flux was also a dominant term on this day. Magnitudes of $\pm 2 \times 10^{-3}$ m^2s^{-3} were typical with occasional peaks near 5×10^{-3} m^2s^{-3} during the first two hours (Figs. 36 and 37). As turbulent activity decreased turbulent transport values of $\pm 1.5 \times 10^{-3}$ m^2s^{-3} were common (Fig. 41). These profiles were more consistent throughout the data period than on 1-2Jul89.

The residuals for the uw budget were generally positive through the entire measurement period, with only occasional negative values as the lowest altitudes. The net vw budgets (residuals) were also typically positive with some negative tendencies at the highest data points until the last two averages during which it

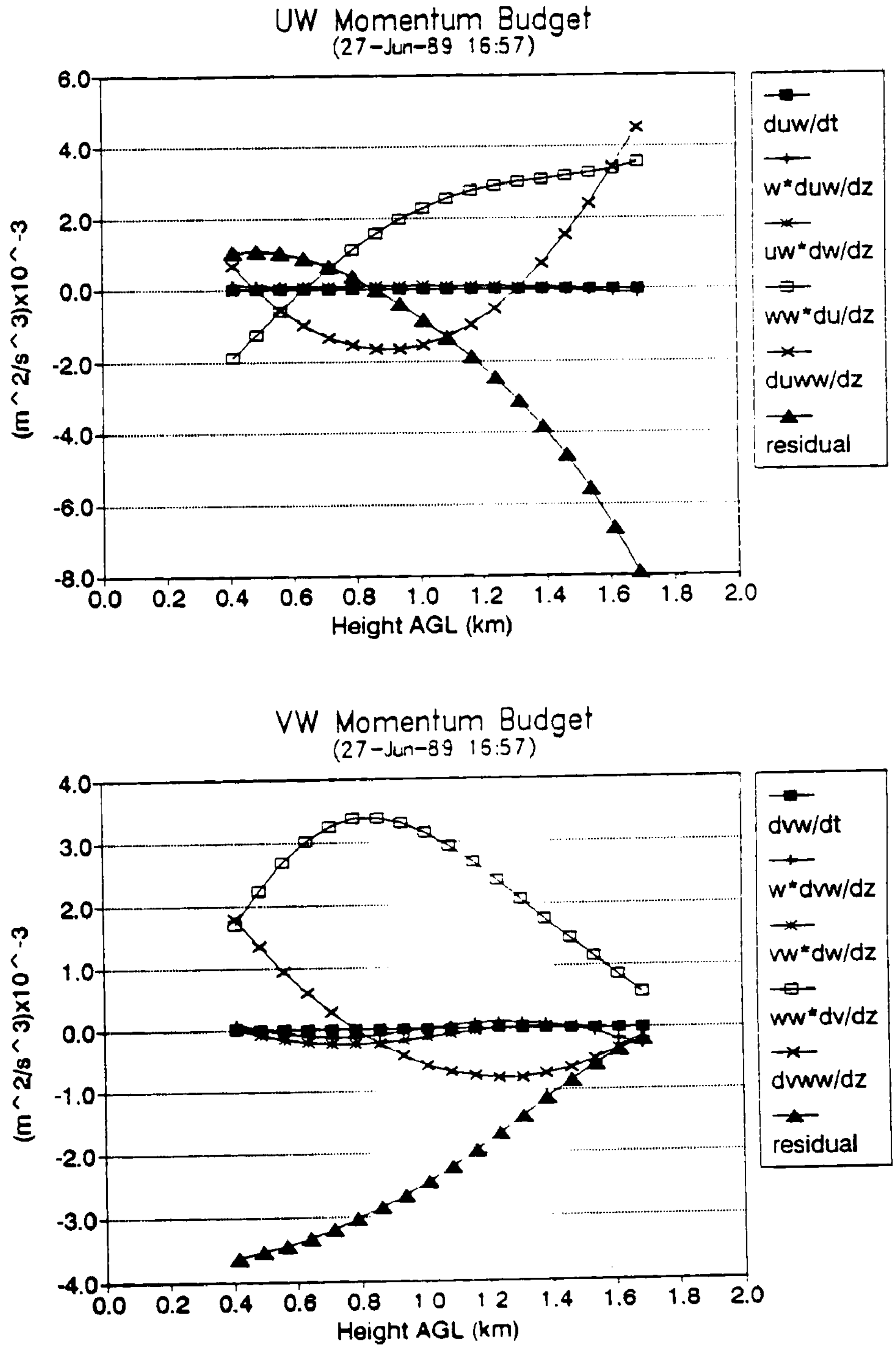

UW Momentum Budget
(27-Jun-89 16:57)

VW Momentum Budget
(27-Jun-89 16:57)

Fig. 36. Horizontal turbulent momentum flux budgets for 27Jun89 at 16:57 CDT. Terms are derived from the one hour average best-fit plots in Figs. 30-35. The residual is the sum of all the derived terms.

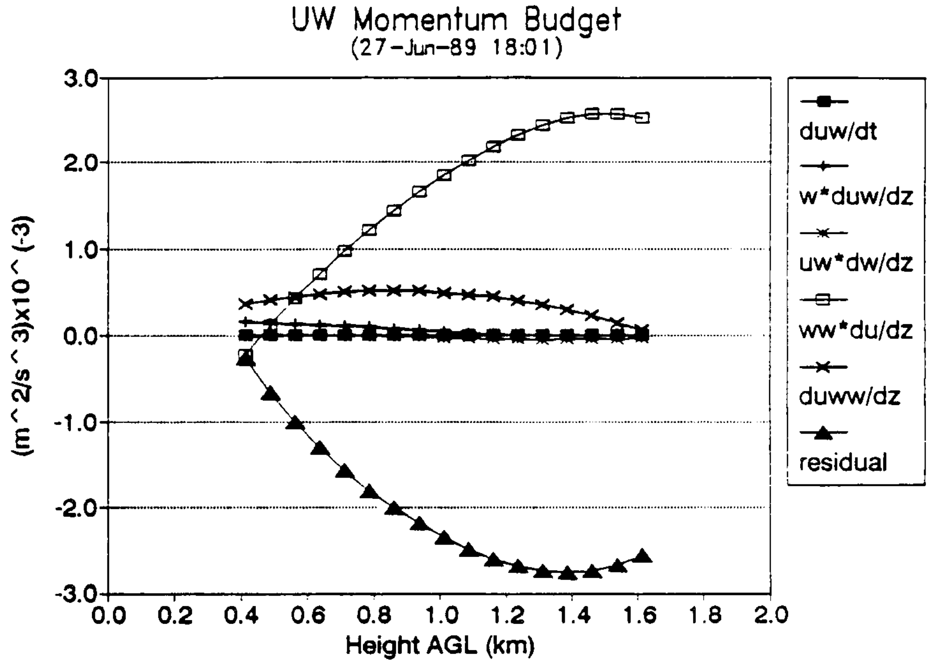

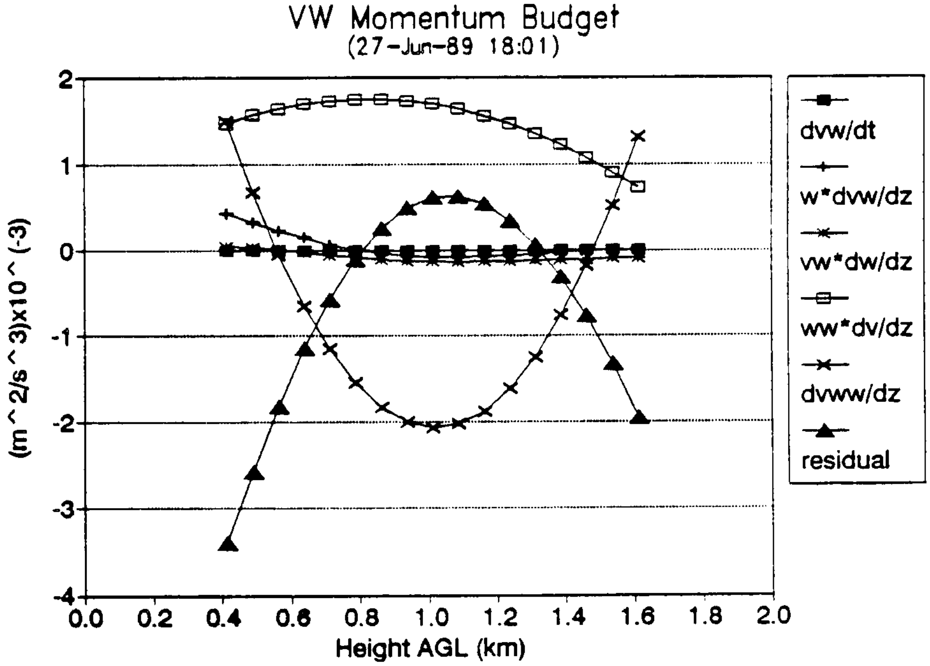

Fig. 37. As in Fig. 36 for 27Jun89 at 18:01 CDT.

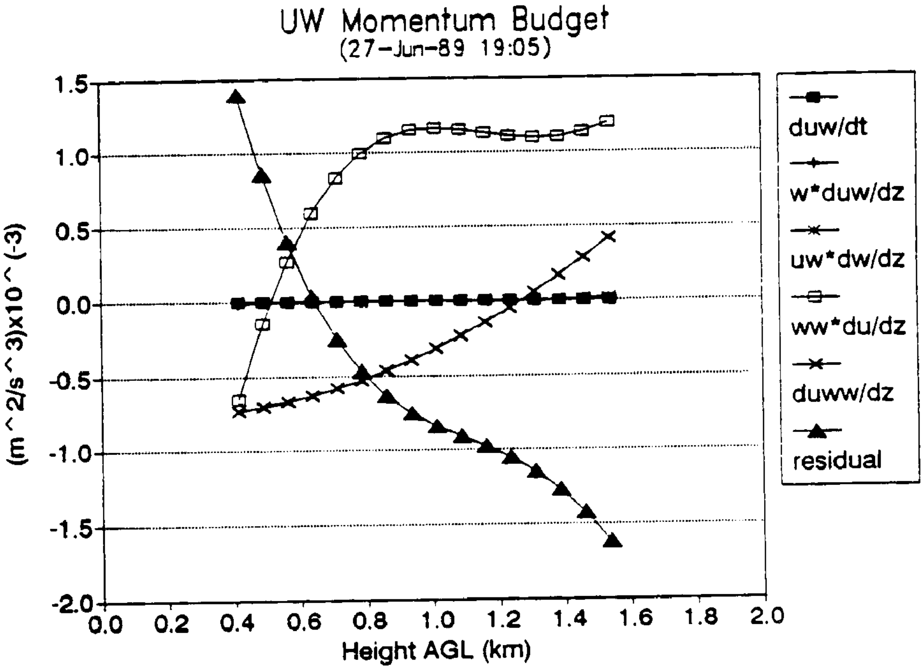

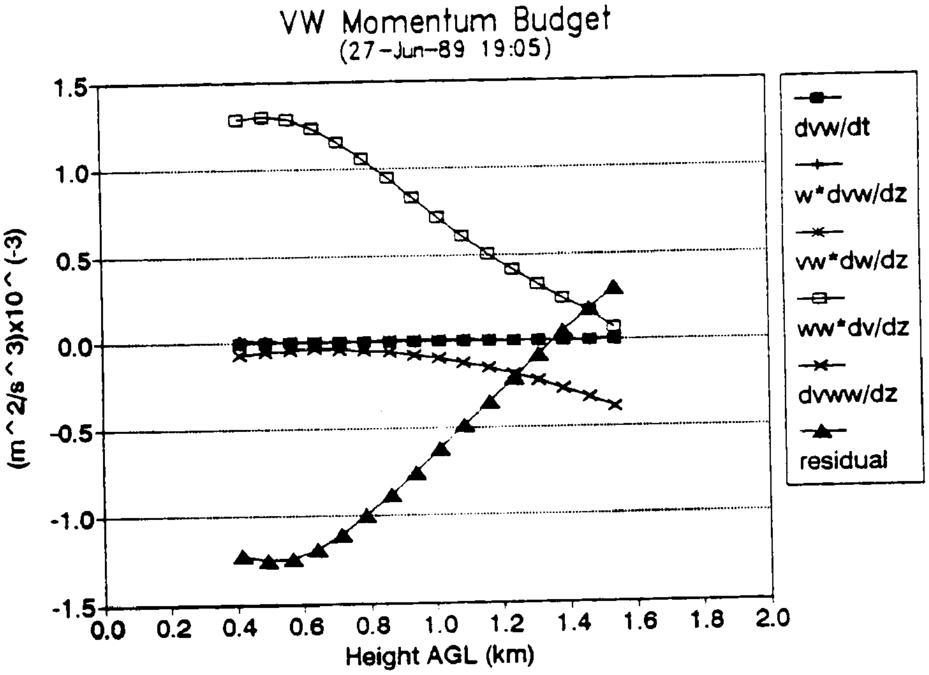

Fig. 38. As in Fig. 36 for 27Jun89 at 19:05 CDT.

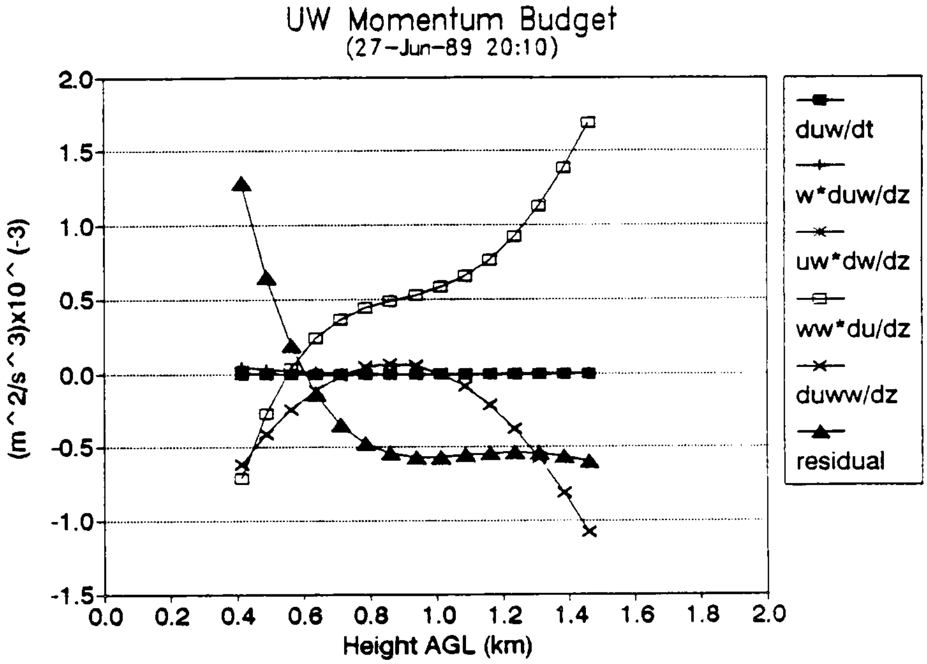

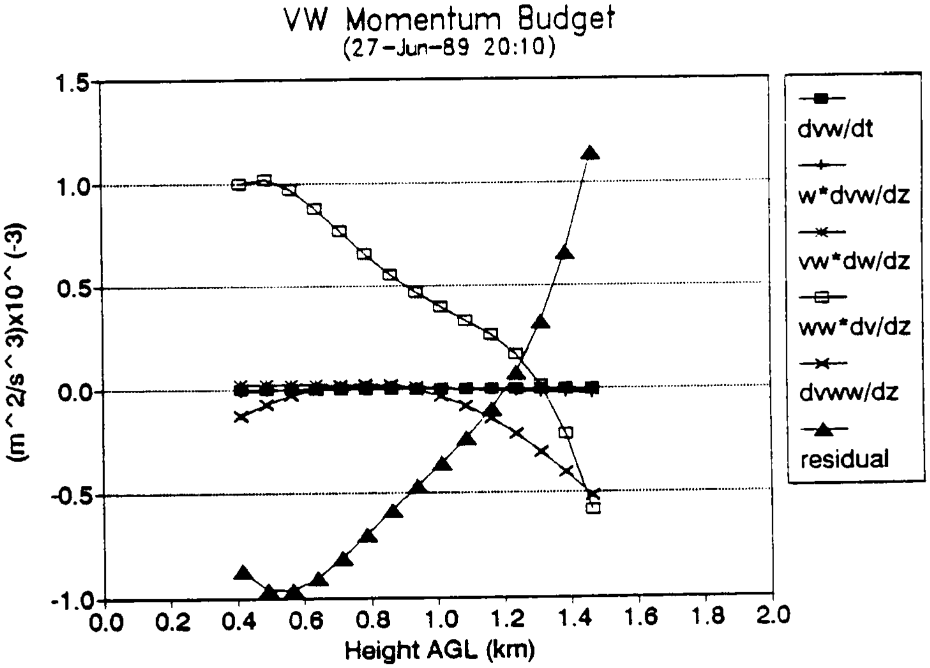

Fig. 39. As in Fig. 36 for 27Jun89 at 20:10 CDT.

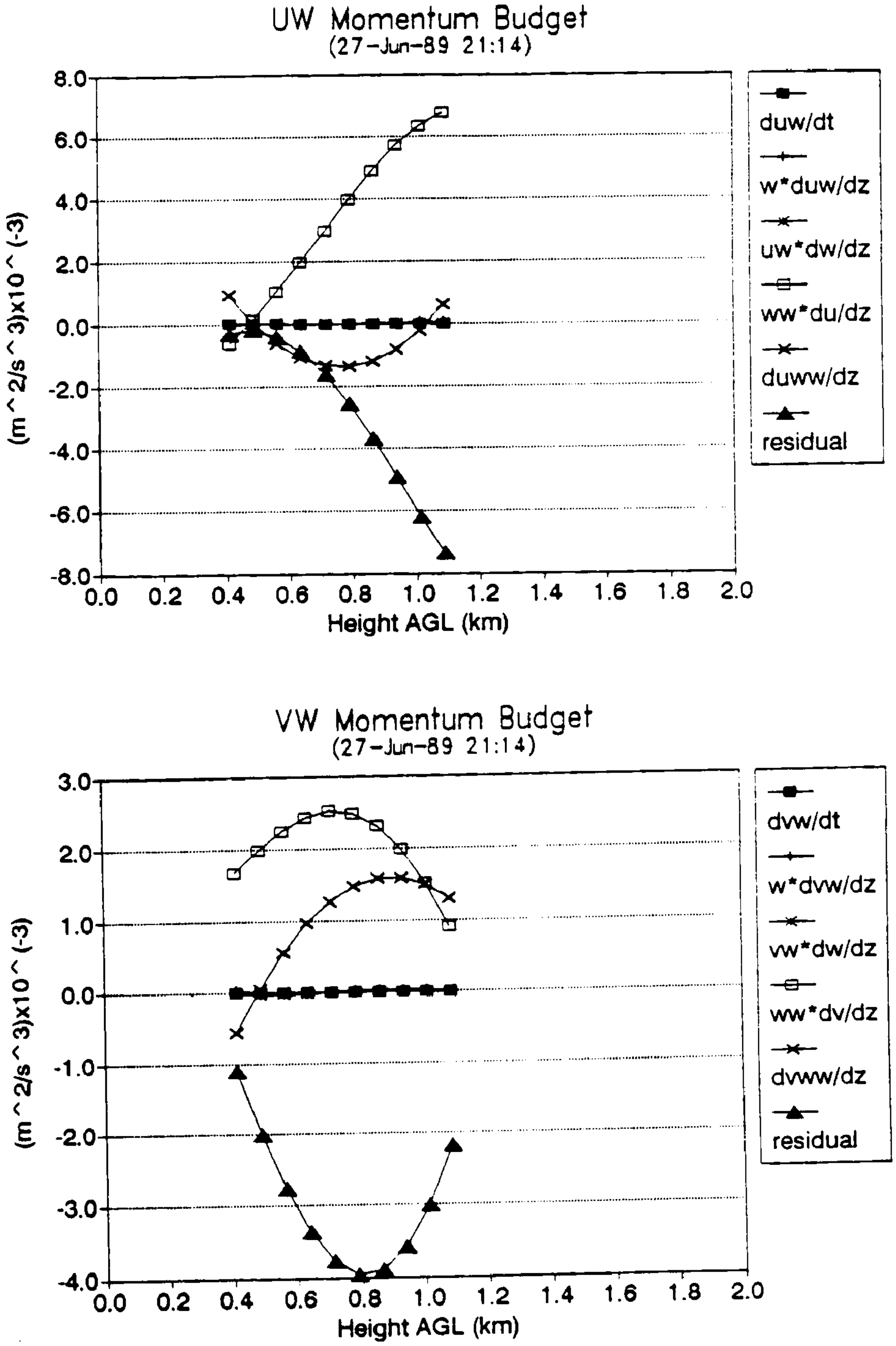

Fig. 40. As in Fig. 36 for 27Jun89 at 21:14 CDT.

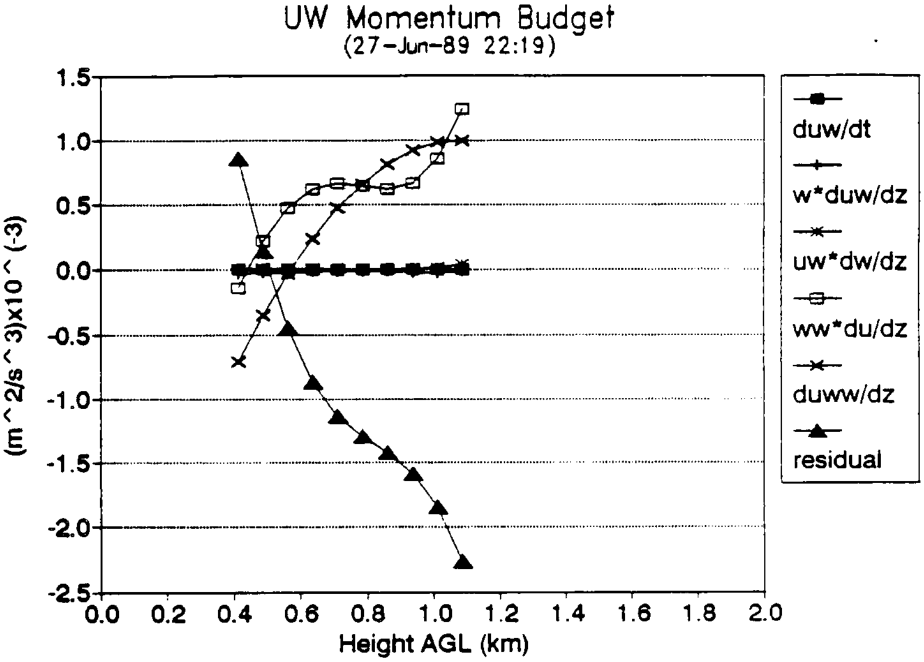

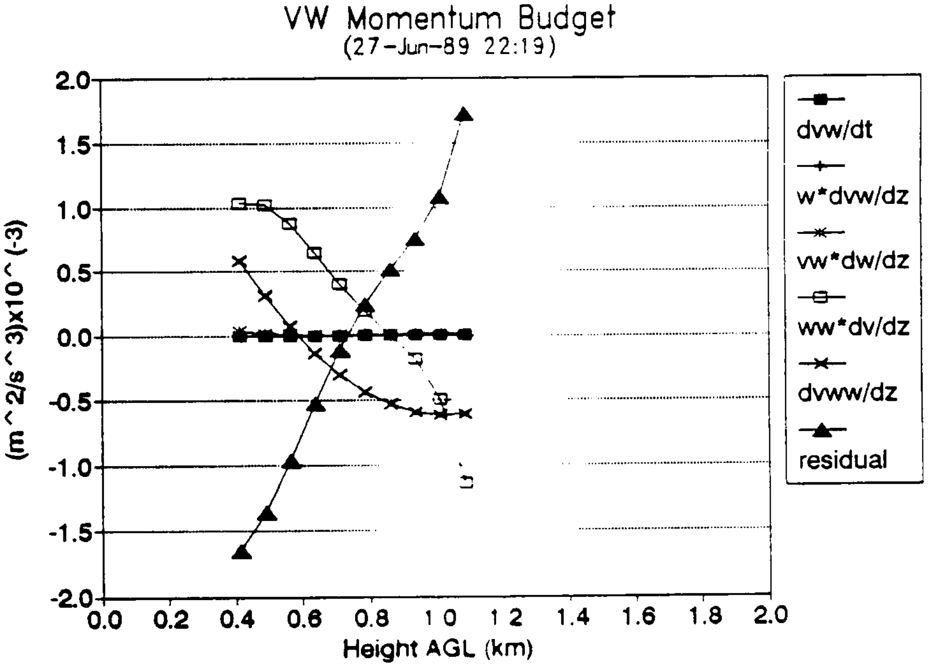

Fig. 41. As in Fig. 36 for 27Jun89 at 22:19 CDT.

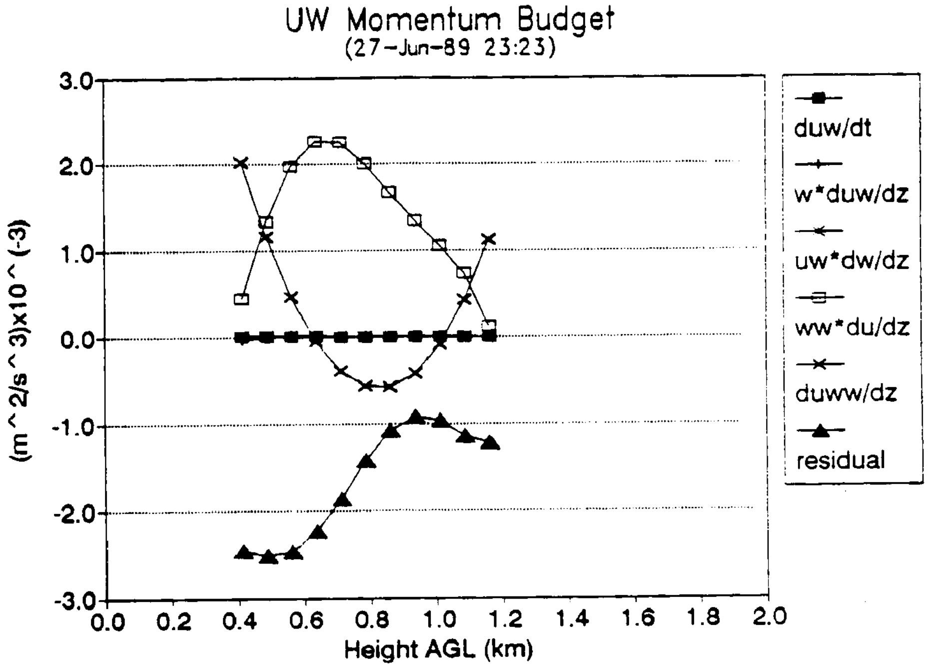

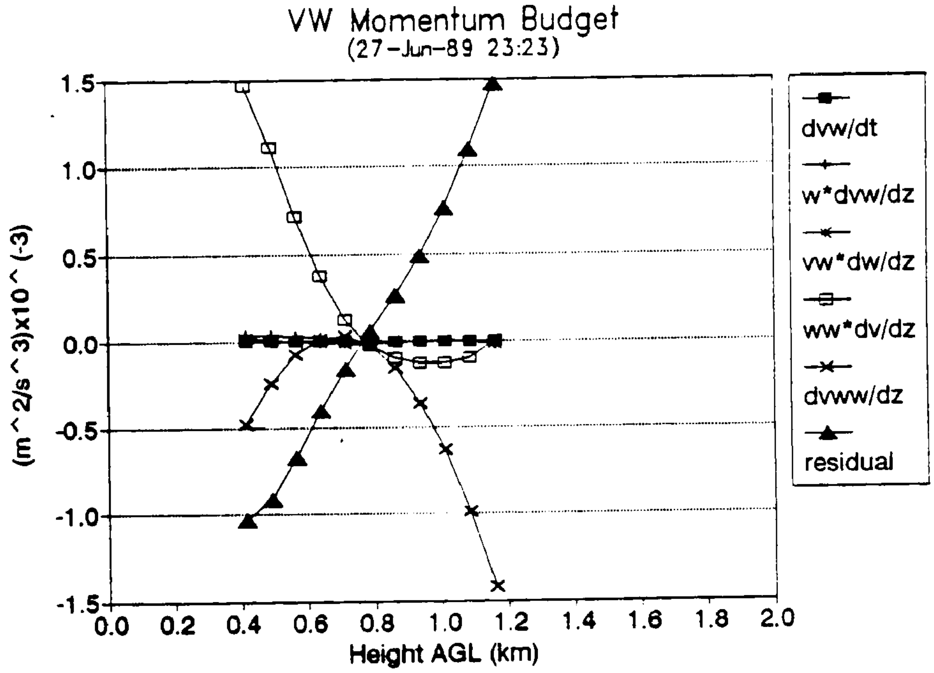

Fig. 42. As in Fig. 36 for 27Jun89 at 23:23 CDT.

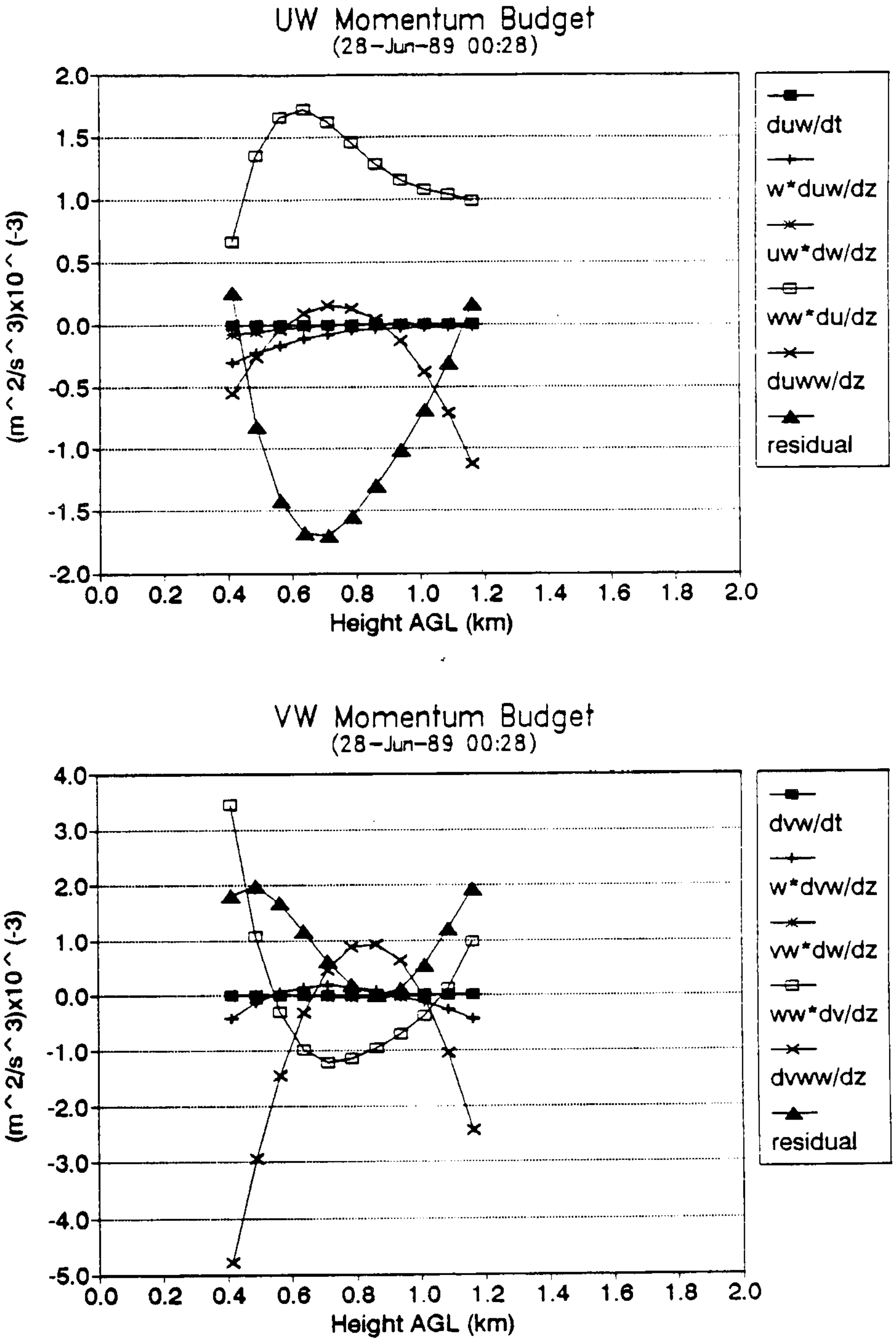

Fig. 43. As in Fig. 36 for 28Jun89 at 00:28 CDT.

became mostly negative at all levels. Peak magnitudes were in the range $\pm 6 \times 10^{-3}$ m^2s^{-3} early in the data (Fig. 36) and typically less than 2×10^{-3} m^2s^{-3} late in the period (Figs. 42 and 43).

6c. 3CPO 19Jun88

i. Evolution of Statistical Turbulence Profiles

The time series data from 3CPO in Figs. 44-49 covers the period from 10:54 CDT to 15:08 CDT on 19Jun88 and is therefore confined to the daytime PBL. Velocities (Fig. 45) were between 4 ms^{-1} and 7 ms^{-1}. They turned from the SSW to the SW and back to the SSW over the data period (Fig. 44). The velocity profiles exhibit significant curvature.

The horizontal momentum flux (Fig. 46) is slightly weaker than the NDTP data but still within the range ± 1 m^2s^{-2}. There was a slow changed in $\overline{u'w'}$ from positive at low levels and negative at higher levels to negative at all heights. The northward component of horizontal momentum flux ($\overline{v'w'}$) is initially negative below 1.3 km AGL and positive above this level. It slowly meanders becoming negative at all heights by the end of the data period.

The third moment terms $\overline{u'w'^2}$ and $\overline{v'w'^2}$ (Fig. 47) are somewhat noisy but the data fit picks up on the general trends. Basing the magnitudes on the best-fit curves, $\overline{u'w'^2}$ and $\overline{v'w'^2}$ range between ± 1.5 m^3s^{-3} peaking at ± 5 m^3s^{-3} between 13:42 CDT and 14:22 CDT. These statistics also change slowly with time.

Vertical velocities (Fig. 48) are negative at all levels except for a slight tendency for positive values at the highest data points. Peak values of -0.5 ms^{-1} occur between 700 and 800 m with smaller values above and below this level. The exceptions are the averaging periods of 13:42 CDT and 14:22 CDT. During these periods $\bar{w}$ is nearly zero at the lowest data levels and decreases nearly linearly with height. The only feature of the flow field which would seem to influence these averages is the directional change from the SSW back to the SW. The variance in

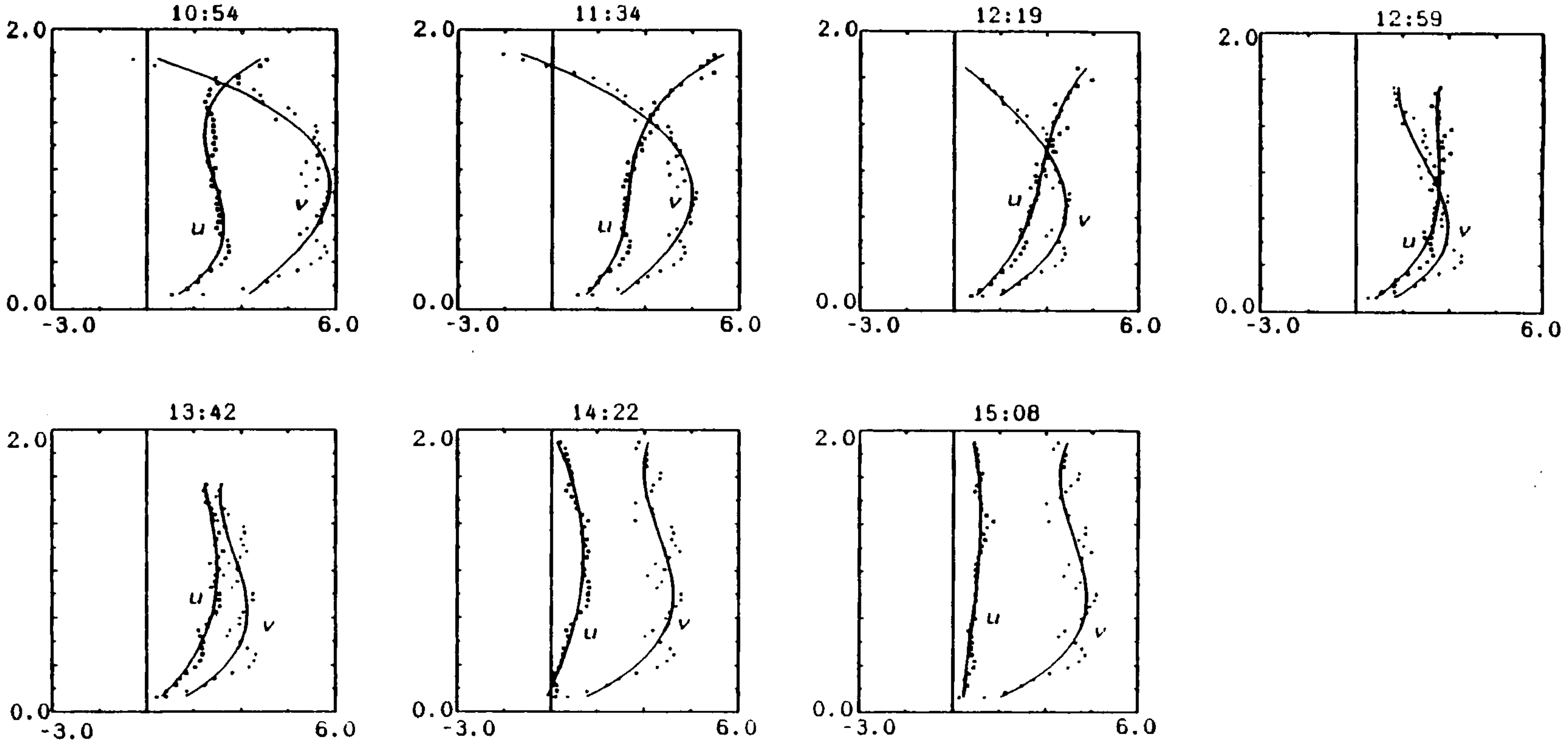

Fig. 44. Time series analysis of mean wind components for 19Jun89. Vertical scale is km and horizontal scale is ms^{-1}. All plots are from a 13 volume scan average (57 minutes).

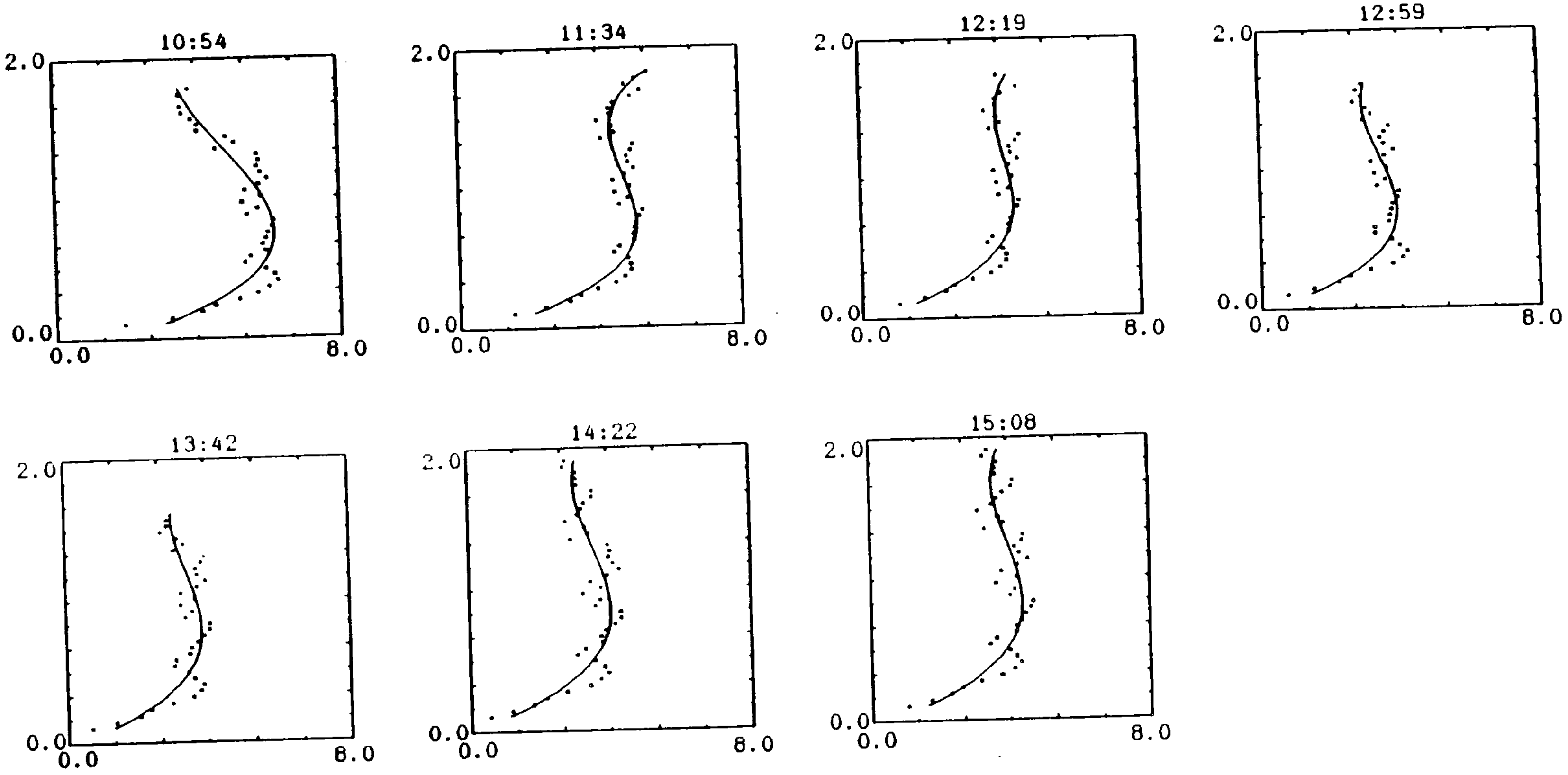

Fig. 45. As in Fig. 44 for wind speed. Horizontal scale is ms^{-1}.

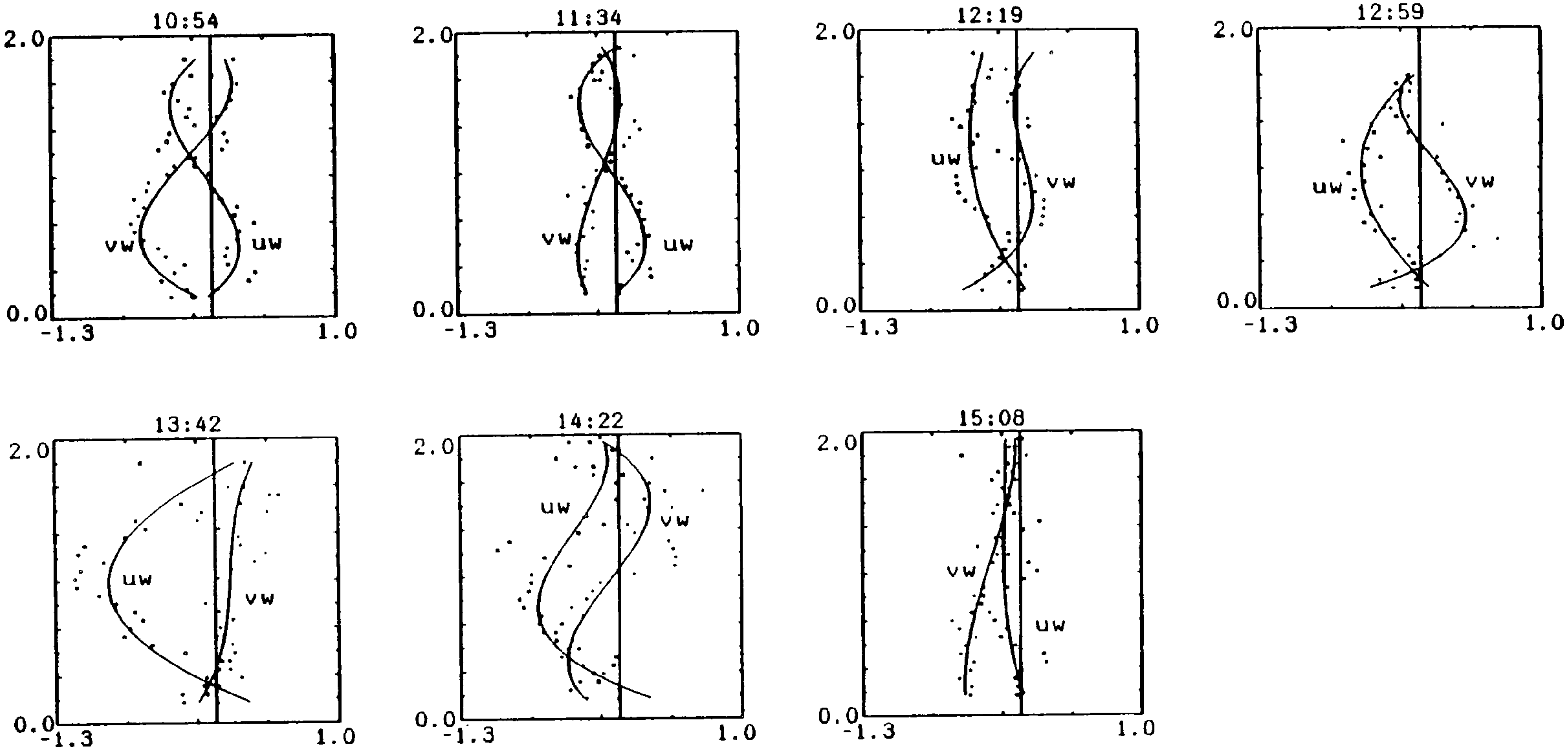

Fig. 46. As in Fig. 44 for $\overline{u'w'}$ and $\overline{v'w'}$. Horizontal scale is m^2s^{-2}.

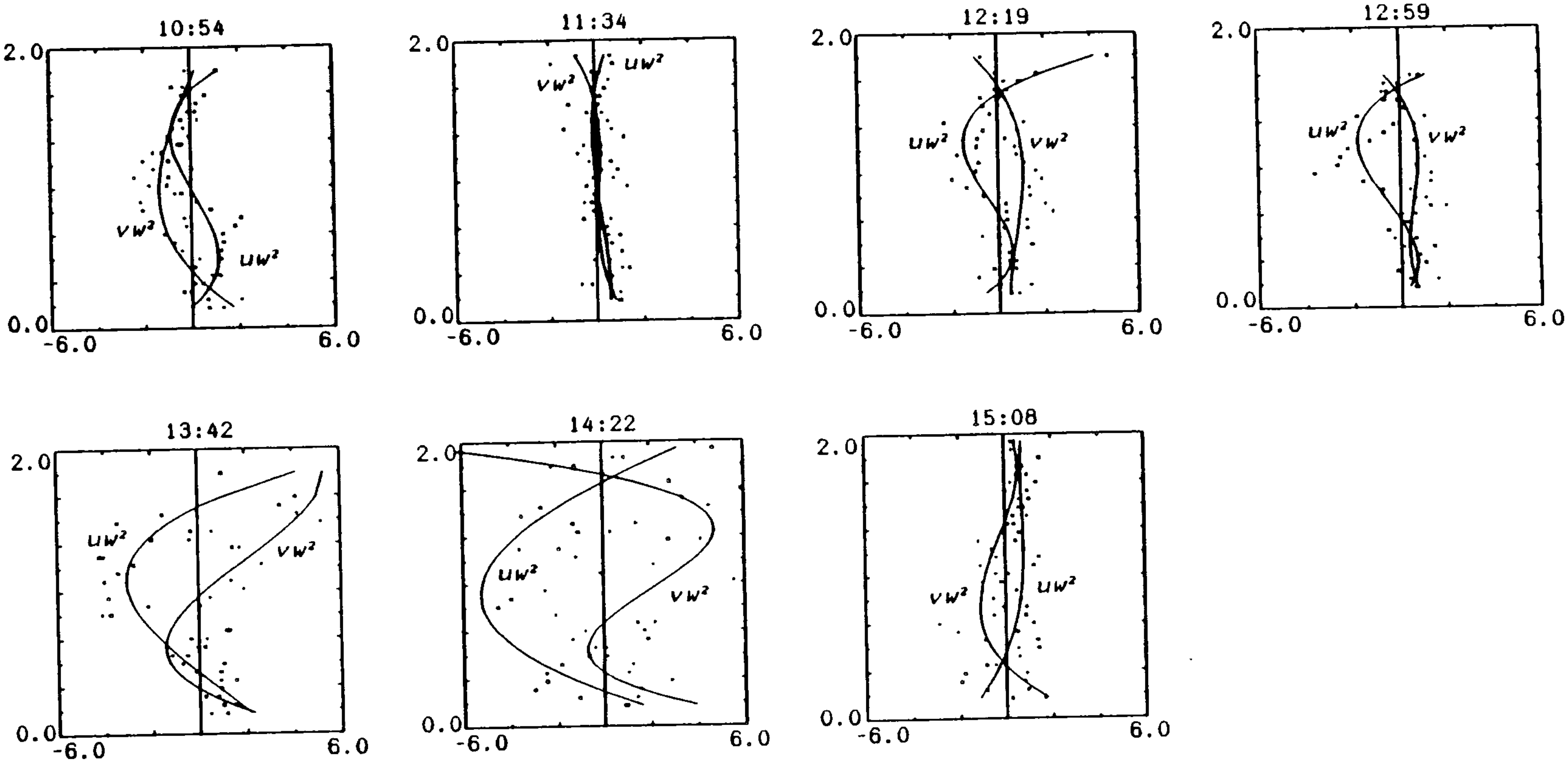

Fig. 47. As in Fig. 44 for $\overline{u'w'^2}$ and $\overline{v'w'^2}$. Horizontal scale is m^3s^{-3}.

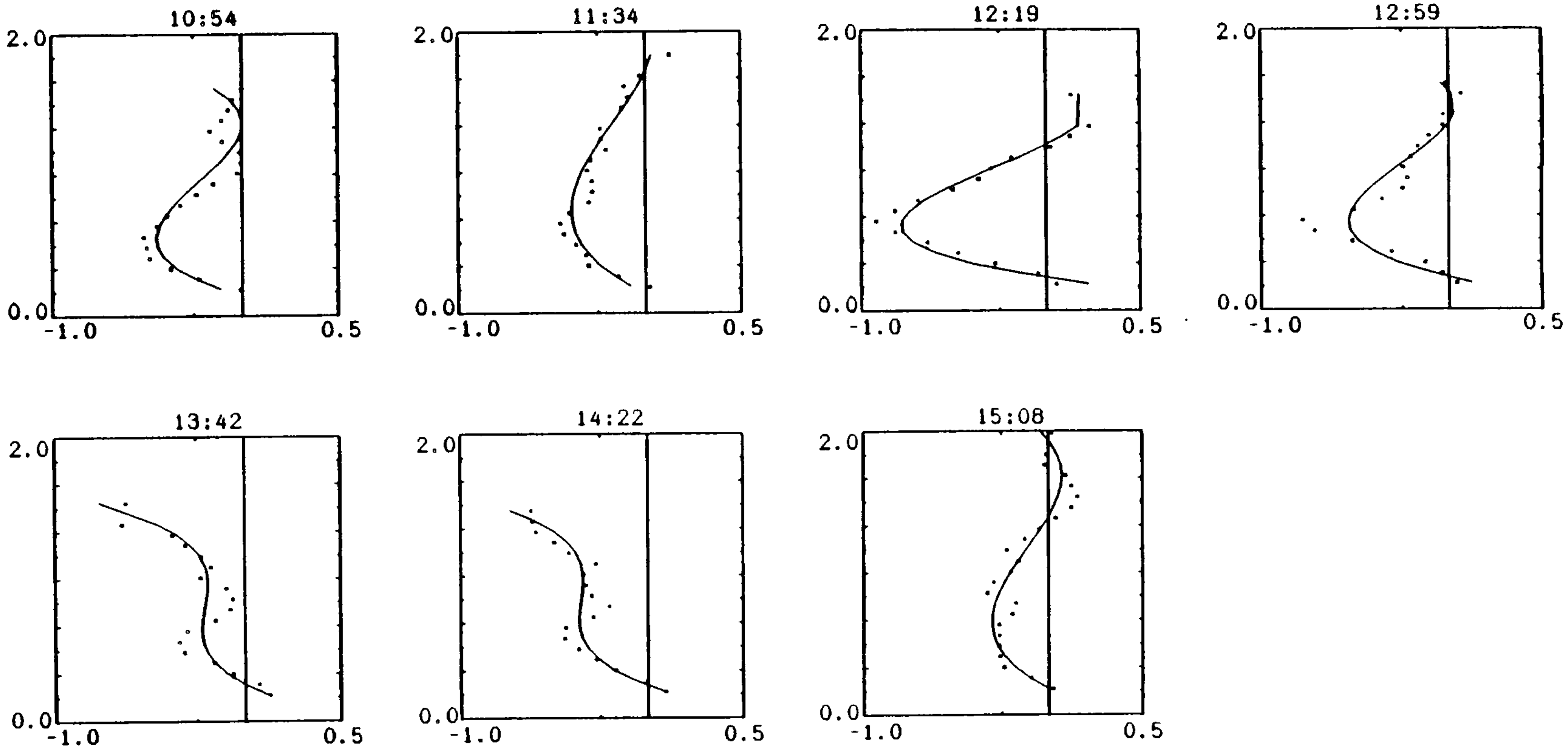

Fig. 48. As in Fig. 44 for vertical velocity. Horizontal scale is ms^{-1}. Negative motions are downward.

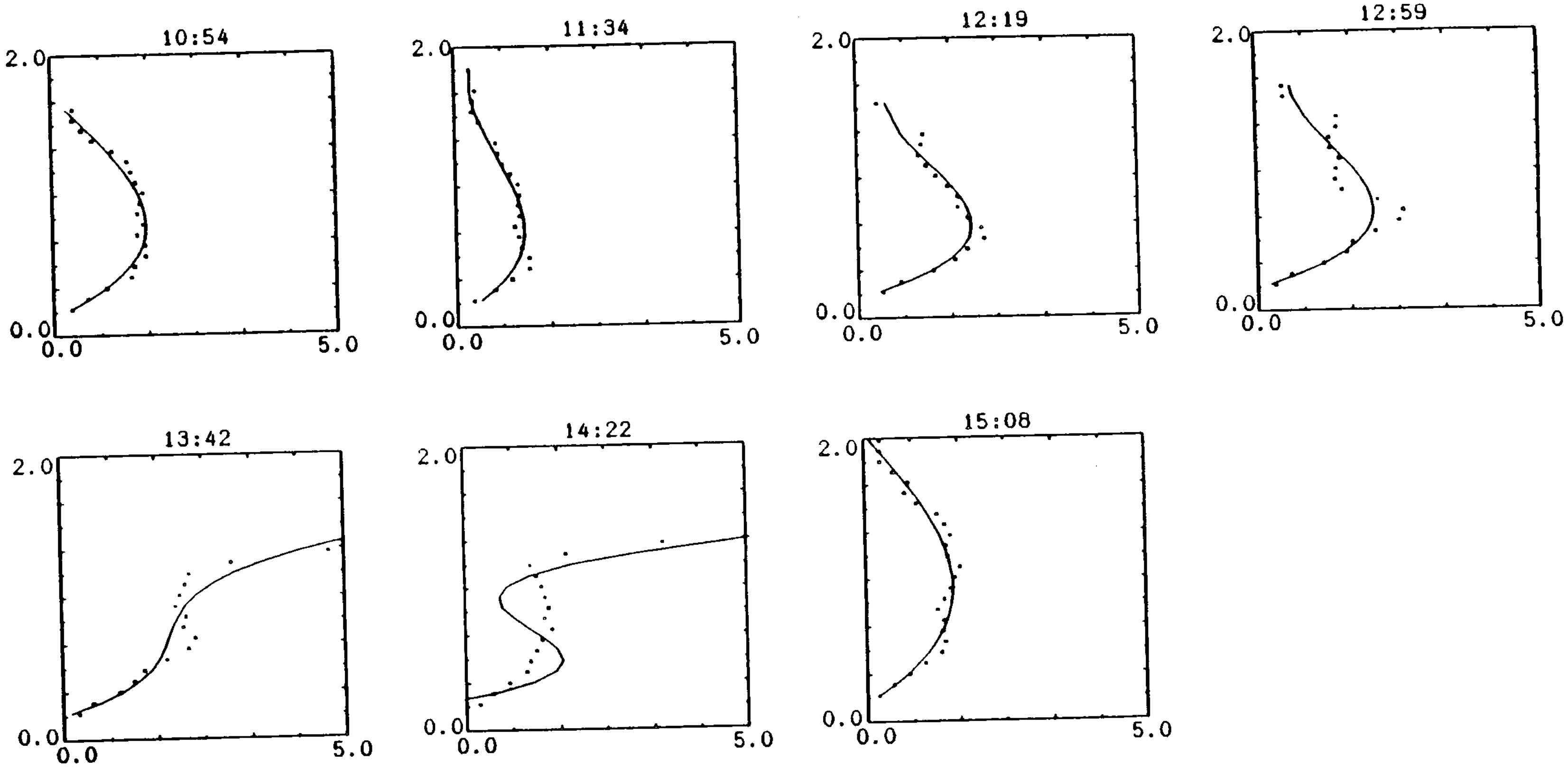

Fig. 49. As in Fig. 44 for vertical velocity variance. Horizontal scale is m^2s^{-2}.

$\bar{w}$ (Fig. 49) also changed in character during these periods exhibiting uniform or increasing values with height. Otherwise $\overline{w'^2}$ has a typical bell shape peaking at 1.5 m^2s^{-2} between 700 and 800 m.

ii. Evolution of Turbulence Momentum Budget

Figures 50-54 contain the solution to the terms in the momentum budget for 19Jun88. Due to difficulties in editing some of the data only five near one-hour averages (57 minutes) are presented which cover the central portions of the data are presented. As a consequence of initial data formats the averages are offset by 40 to 45 minutes for the 3CPO data so there is some overlap in these data.

The time change terms of horizontal momentum flux as in the previously discussed data sets are negligible over the entire period. Contributions from shear production and mean advection of momentum flux by $\bar{w}$ are very small, less than $\pm 0.5 \times 10^{-3}$ m^2s^{-3} (Fig. 51). This again leaves horizontal shear production and turbulent transport as the dominant terms in the momentum flux budgets.

Shear production and turbulent transport are comparable in magnitude over the data period. Typical magnitudes are within $\pm 5 \times 10^{-3}$ m^2s^{-3} except during the 14:22 CDT averaging period where values more than double this were observed for turbulent transport. In the uw budget shear production was initially negative at mid-levels and positive above and below these levels (Fig. 50). This changed to positive at all levels for the next two averaging periods (Figs. 51 and 52). Magnitudes then weakened at low levels and became negative at upper levels for the last two averages (Figs. 53 and 54). Shear production for the vw budget is positive at low levels and negative aloft for all averaging periods.

Turbulent transport in the uw budget is generally negative at mid- and low-levels and positive at higher levels with occasional positive values at the lowest levels. The vw component is more difficult to characterize and tends to fluctuate throughout the data period.

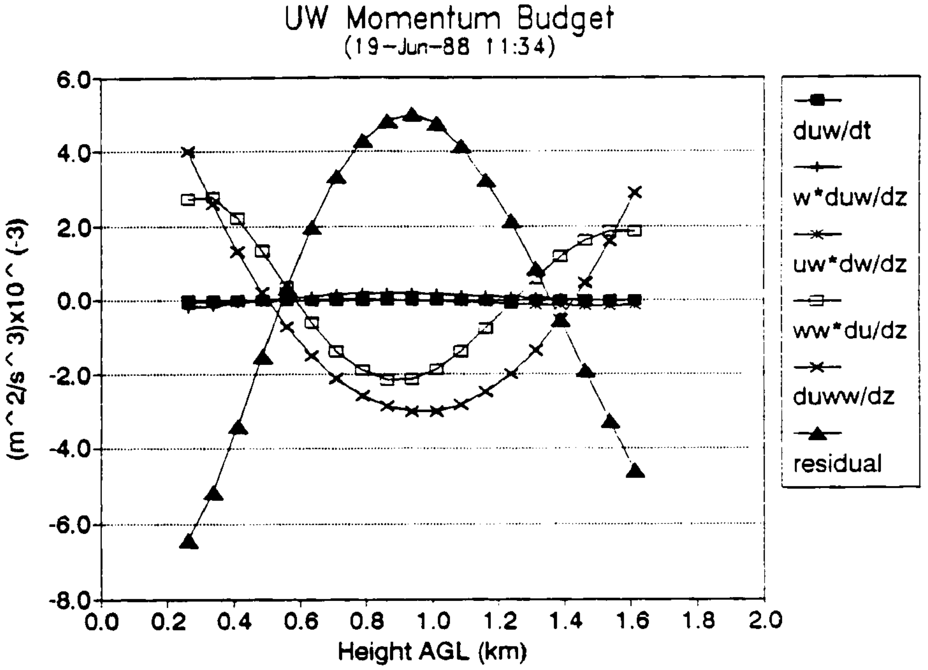

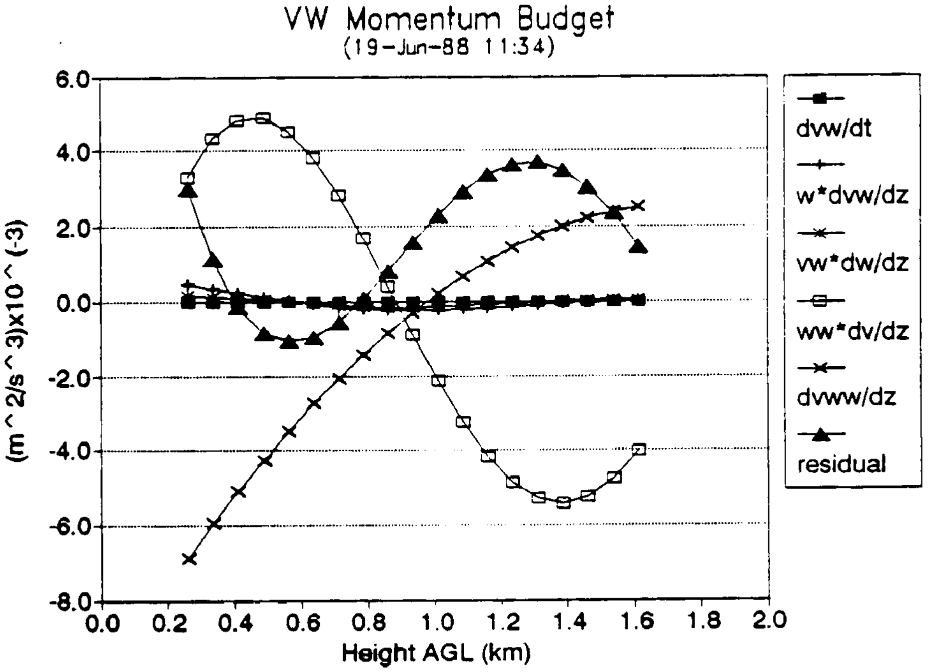

Fig. 50. Horizontal turbulent momentum flux budgets for 19Jun88 at 11:34 CDT. Terms are derived from the one hour average best-fit plots in Figs. 44-49. The residual is the sum of all the derived terms.

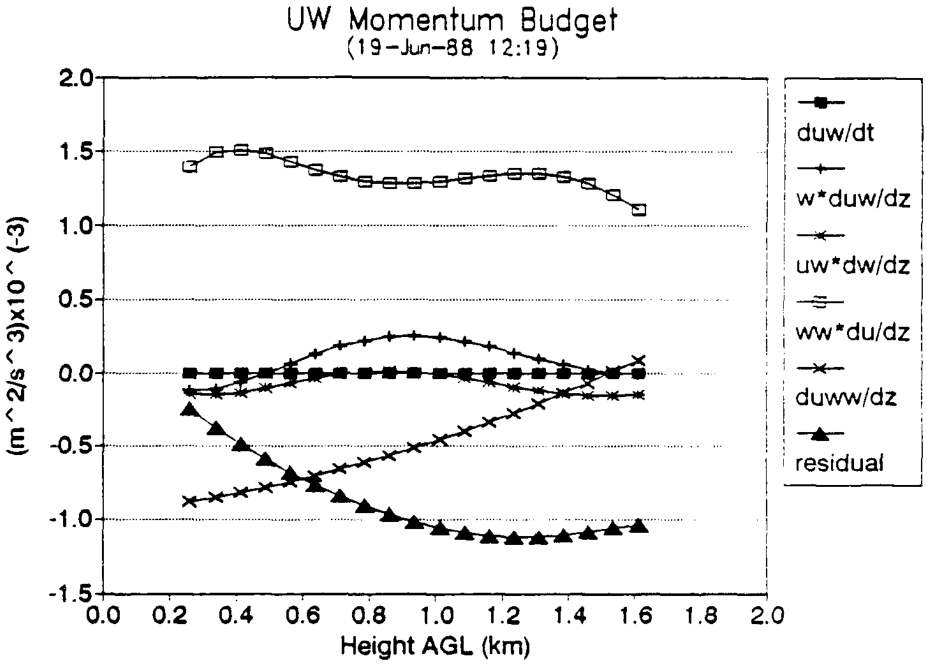

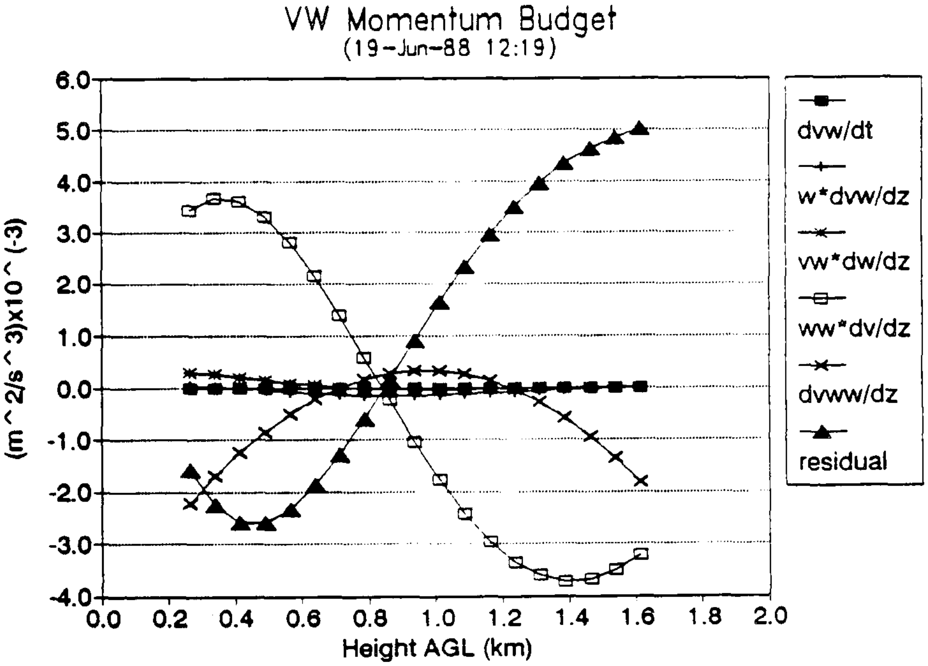

Fig. 51. As in Fig. 50 for 19Jun88 at 12:19 CDT.

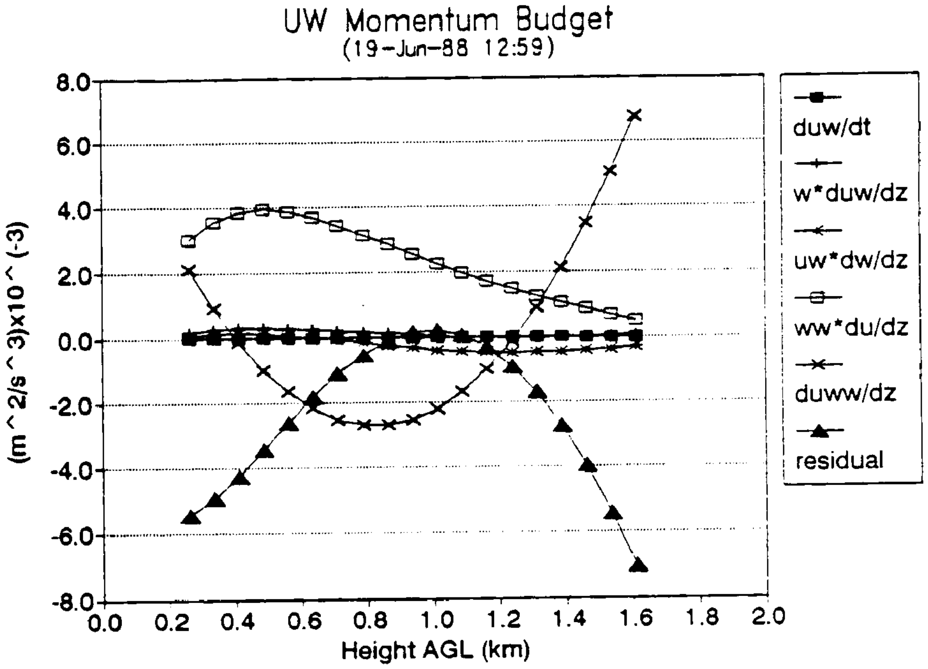

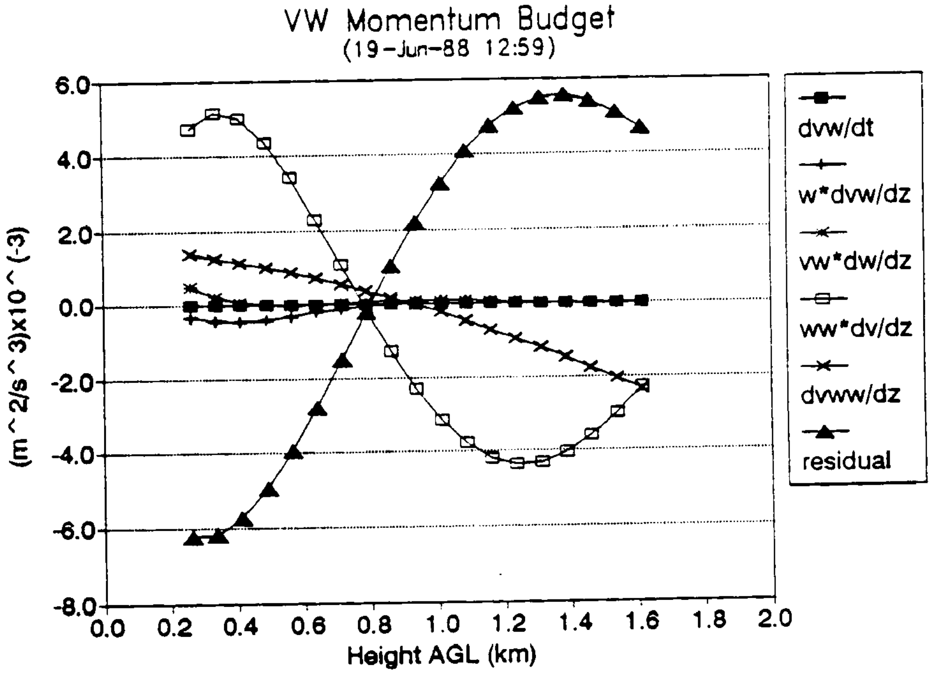

Fig. 52. As in Fig. 50 for 19Jun88 at 12:59 CDT.

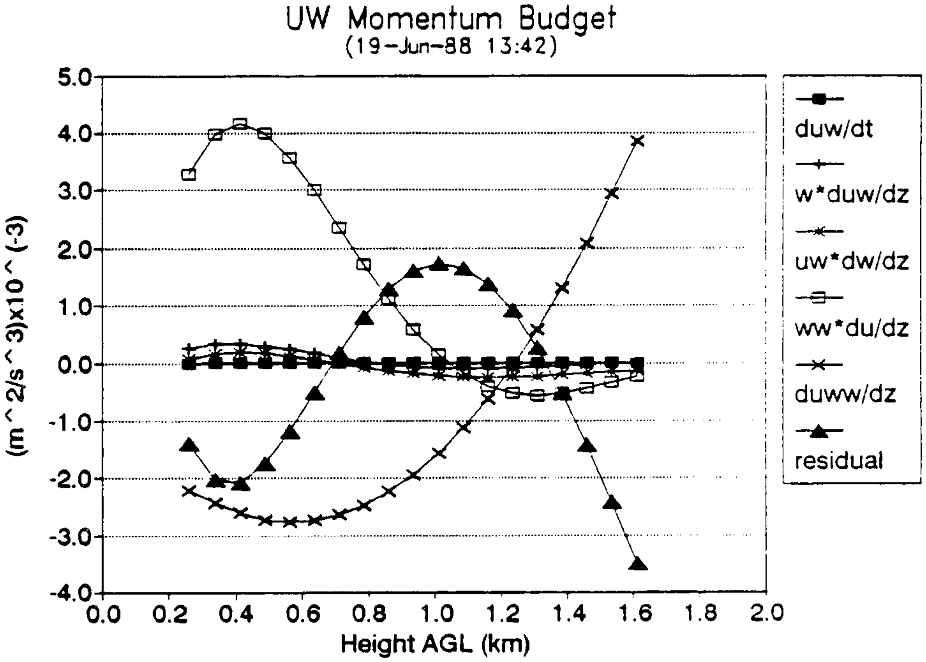

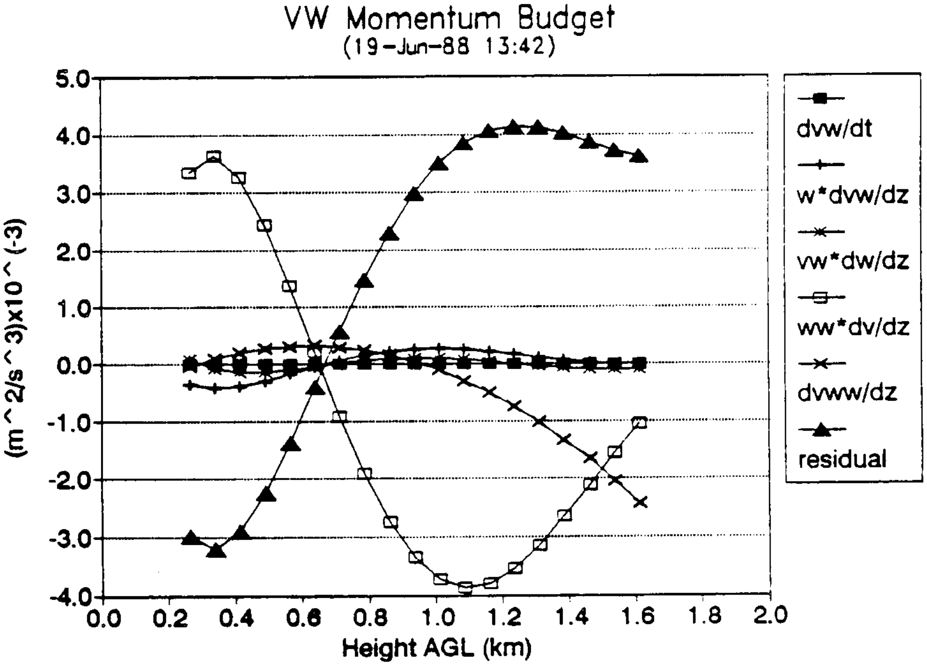

Fig. 53. As in Fig. 50 for 19Jun88 at 13:42 CDT.

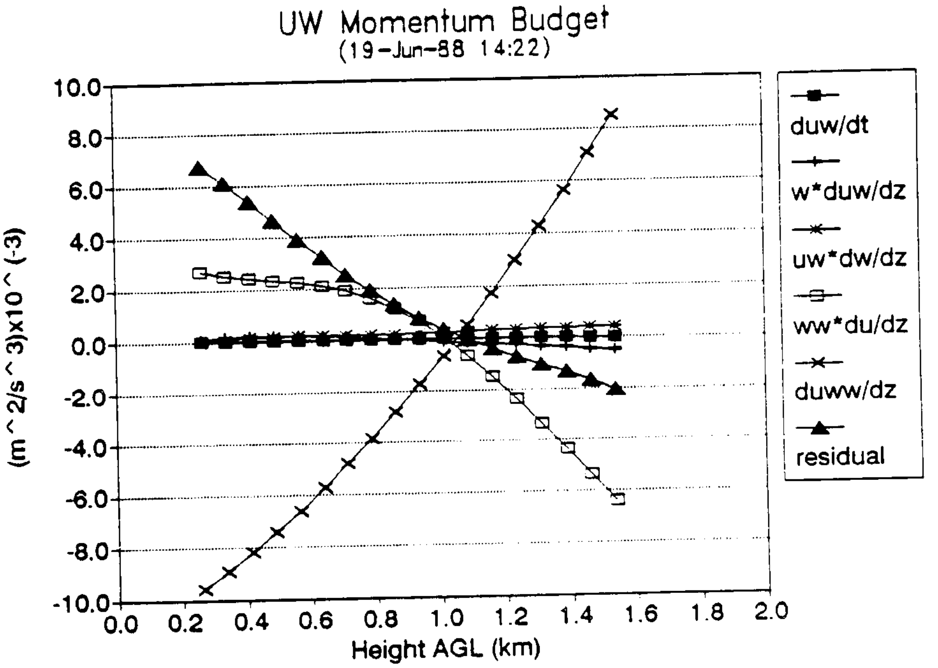

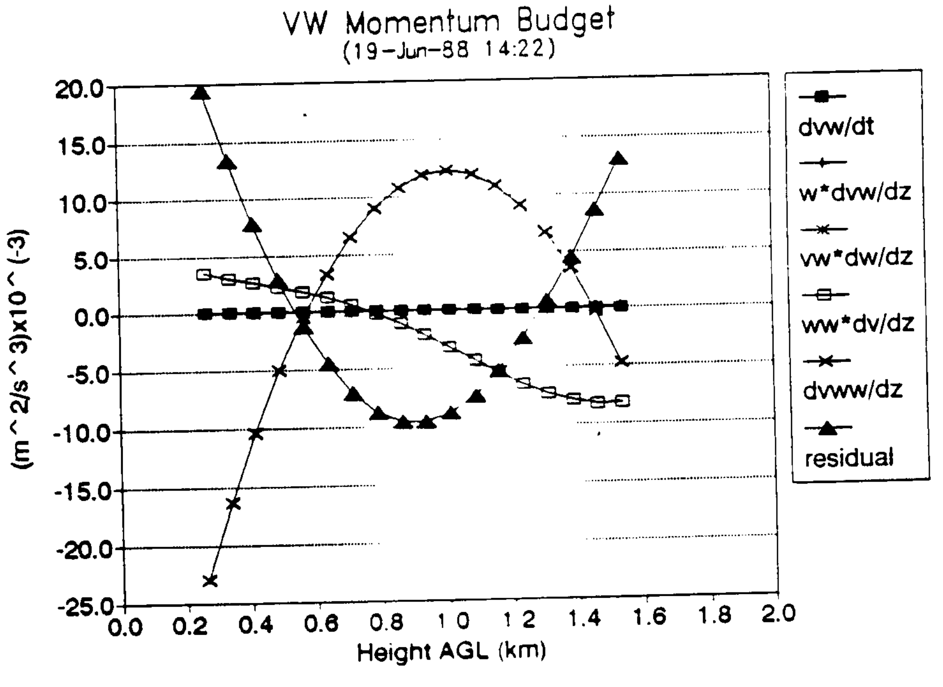

Fig. 54. As in Fig. 50 for 19Jun88 at 14:22 CDT.

6d. Intercomparison of Data Sets

Data from 1-2Jul89 had the largest magnitudes of turbulent transport of the three data sets. This might be anticipated since 1-2Jul89 was the hottest of the three days and was characterized by warm, moist advection. This was the only day during which turbulent transport dominated over shear production. During the night turbulent transport on 1-2Jul89 and 27-28Jun89 became secondary (although still of significant magnitude) to shear production.

27-28Jun89 was the most baroclinic with moderate temperature and pressure gradients over the area (see Fig. 12). 19Jun88 had the weakest synoptic forcing (Fig. 14) and was the most nearly undisturbed case. On both of these days shear production was of the same order or slightly larger than turbulent transport during convective daytime conditions.

In all cases the radar VAD analysis indicates significant turbulent transport of horizontal momentum flux under a variety of mesoscale environments. Even during nighttime, weakly forced conditions these terms were consistently of significant magnitude.

In order to illustrate the vertical structure of the derived momentum flux budgets a one hour period from 1Jul89 and 27Jun89 will be examined. The averaging period will be chosen such that the values of the momentum fluxes $\overline{u'w'}$ and $\overline{v'w'}$ are nearly all positive or all negative throughout the depth of the data. This will facilitate the identification of source and sink terms within the budget equations.

On 1Jul89 at 16:29 CDT $\overline{u'w'}$ is positive through most of the data and $\overline{v'w'}$ is negative (Fig. 17). Therefore negative values in Fig. 22 are sources for $\overline{u'w'}$ and sinks for $\overline{v'w'}$. For the uw budget then mean advection and shear production by $\bar{w}$ are weak sources below 1.4 km and sinks above this level. Horizontal shear production is a strong sink below 0.9 km and a significant source above this level.

Turbulent transport is a sink below 0.6 km and above 1.4 km. At mid-levels it is a source of uw momentum flux. The net budget (residual) then results in a sink below 0.7 km and above 1.5 km. In the mid-levels there is a strong production of uw momentum flux.

The vw budget has a different character with shear production being a dominant source through the depth of the data. All other terms are secondary except for turbulent transport which is a moderate sink below 0.6 km and a dominant sink above 1.2 km. This produces a net production of vw momentum flux below 1.4 km and a sink above this level.

On 27Jun89 at 16:57 CDT $\overline{u'w'}$ is positive at all levels. Below 1.2 km $\overline{v'w'}$ is negative and positive above (Fig. 32). The dominant terms in the momentum flux budgets are shear production and turbulent transport. Shear production is a source below 0.6 km for $\overline{u'w'}$ and a sink above this level. For $\overline{v'w'}$ shear production is a source below 1.2 km and a sink above this height. Turbulent transport is a source for $\overline{u'w'}$ between 0.5 km and 1.3 km and sink above and below this height interval. Below 0.8 km turbulent transport is a source for vw momentum flux. Above this level it is a sink until $\overline{v'w'}$ reverses sign at which point turbulent transport becomes a source again. Other terms are generally negligible contributors to the uw budget and minor to the vw budget. The contribution of these terms acts as a net source of $\overline{u'w'}$ below 0.9 km and a sink aloft. The net contribution for the vw budget is a source below 1.2 km and a sink above this height.

A general tendency in this analysis is for the individual terms of the momentum budgets to have large values at the extremes of the data. This would be expected since the surface layer and entrainment zone are layers across which large changes in the characteristics of the PBL are found. An important feature is evident in these data, namely that there is no apparent characteristic contribution to the momentum budgets by any of the terms in the budget as is often depicted in modeling studies. In other words, no term can be classified as being a general source or sink of horizontal momentum flux at any particular level when comparing independent data sets or averaging periods. Even in the most undisturbed case study on 19Jun88 this is also true (see Figs. 50-54). This could be the result an inappropriate averaging period (i.e. too short) although from earlier discussions this would appear to be a minor effect. It may also be the general nature of the turbulence in these case studies, exhibiting a continual state of flux which changes from one averaging period to the next independent of the length of the averaging period. In either case the momentum budget data are difficult to classify with respect to any general vertical behavior.

6e. Comparisons with Field and Modeling Statistics

A main objective of this study is to demonstrate the viability of this extended VAD technique. As discussed previously there are no supporting surface measurements from which to derive scaling parameters. Unfortunately many field data and modeling studies present scaled results. Most comparisons will then have to be qualitative except in those cases were data are presented in absolute terms. When results are presented in a budget perspective, as in this study, a comparison of the relative magnitude of terms will be possible whether or not the results are scaled.

Wyngaard (1984) presents stress budgets from the Minnesota data (Kaimal et. al. 1976) and AMTEX (Lenchow et. al. 1980). The top frame in Fig 55 is derived from 2.5 hours of data from 10Sep73 (2 consecutive averaging periods of 75 minutes each) and the lower frame in Fig. 55 is 1.25 hours (one average) from 15Sep73. Shear production in the top of Fig. 55 ranges from 2×10^{-3} m^2s^{-3} to near 10×10^{-3} m^2s^{-3} and is slightly greater than 1.5×10^{-3} m^2s^{-3} in the lower frame. These values are very similar to those found in the present study.

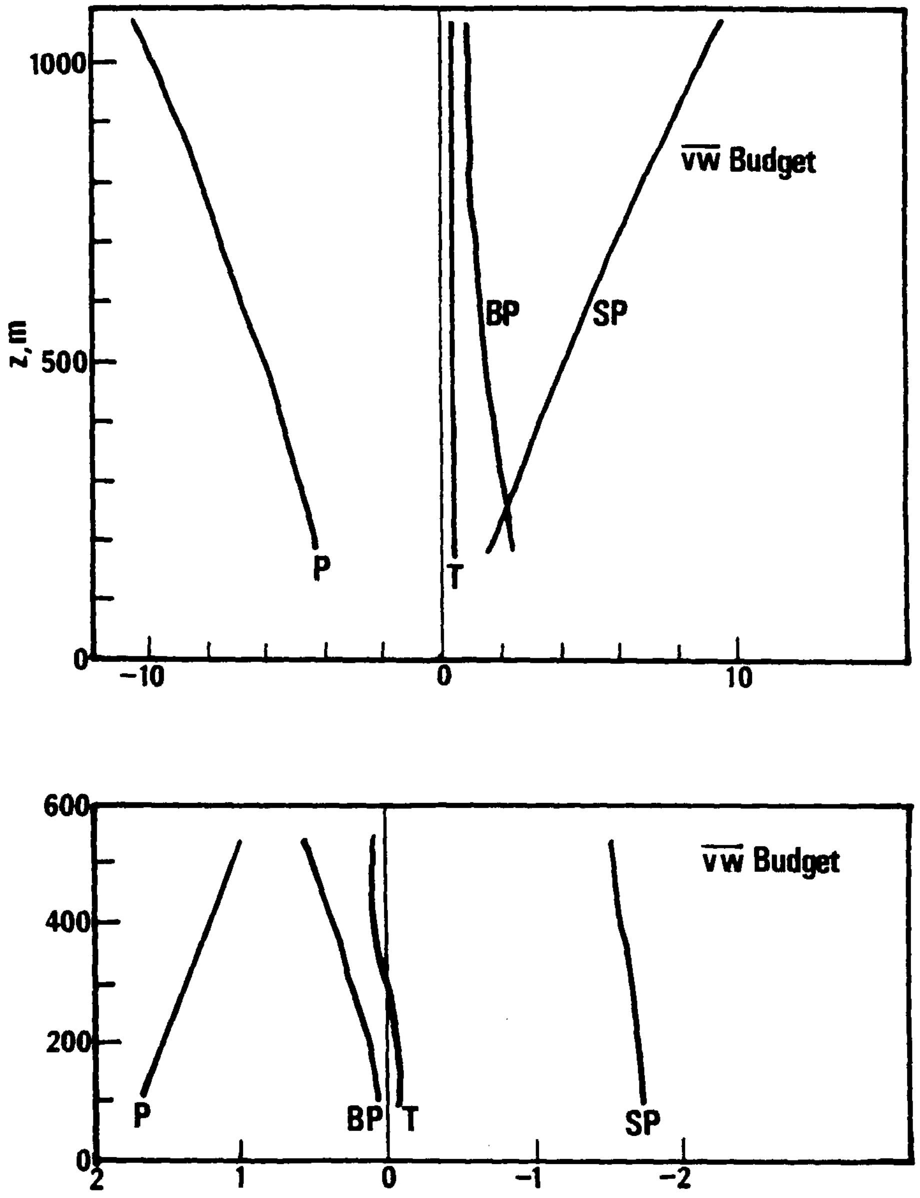

Fig. 55. Stress budgets from the 1973 Minnesota experiments. Horizontal scale is $m^2s^{-3} \times 10^{-3}$. Profiles are SP, shear production; BP, buoyant production; T, turbulent transport; P, pressure term. The top frame is from data periods 2A1 and 2A2 and the bottom frame is from period 5A1. Negative values in the top frame and positive values in the lower frame are losses. (after Wyngaard, 1983).

Turbulent transport on the other hand is extremely small in both cases, less than $\pm 0.2 \times 10^{-3}$ m^2s^{-3} which is closer to the nighttime values found in the radar data. The results from AMTEX are in Fig. 56. The shear production term also falls into the range of values observed in the radar data sets. The turbulent transport peaks near -0.5×10^{-3} m^2s^{-3} which again is smaller than most values observed by the radar.

The reason for the differences in the turbulent transport terms is not clear. The meteorological conditions may be a factor since the present study was conducted under hot, summer conditions, the Minnesota data were obtained in the fall, and AMTEX data were collected during wintertime cold air outbreaks over the East China Sea. They magnitude of surface fluxes may differ considerably under these conditions although even during September in Minnesota there should still be significant surface fluxes and cold air outbreaks over relatively warm water should induce significant convective activity during AMTEX. With appropriate scaling parameters additional insight would be possible.

Therry and Lacarrere (1980) present results from a third-order closure model for the Voves experiment. Figure 57 shows the momentum flux budget which indicates shear production and turbulent transport of nearly equal magnitude. This is similar to most of the radar data results. Absolute magnitudes of the data cannot be compared since the results from their model are scaled.

Briere (1987) modeled a sea-breeze circulation with a third-order closure model and obtained turbulent transport of stress on the order of 1×10^{-3} m^2s^{-3} near the surface. This is in the range of values observed during weakly convective conditions (late evening) in the present study. Considering that sea-breeze circulations are essentially density currents, in the absence of strong surface heating large values of turbulent transport should not be expected. The magnitude

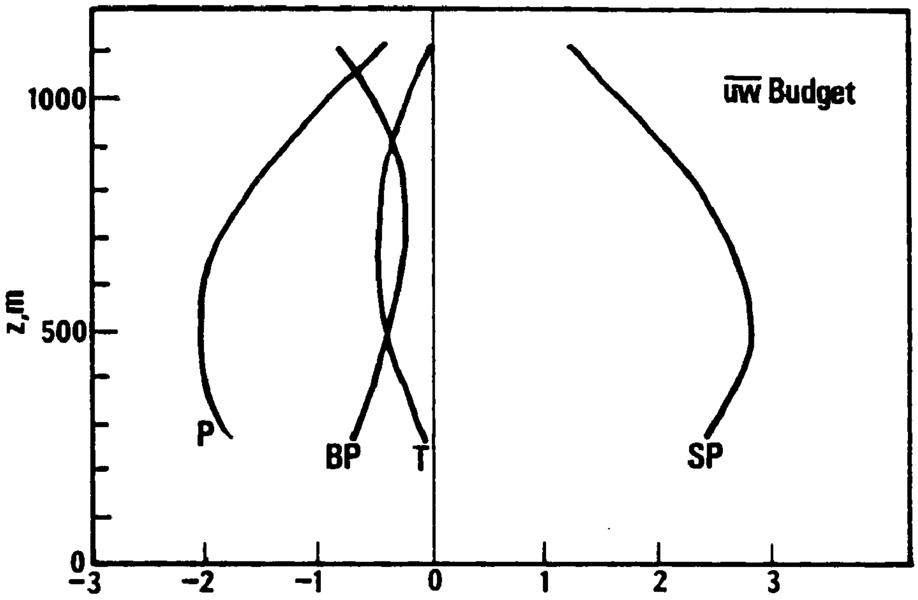

Fig. 56. Stress budgets computed from four days during AMTEX. Horizontal scale is $m^2s^{-3} \times 10^{-3}$. Notation is as in Fig. 55. Negative values are losses. (after Wyngaard, 1983).

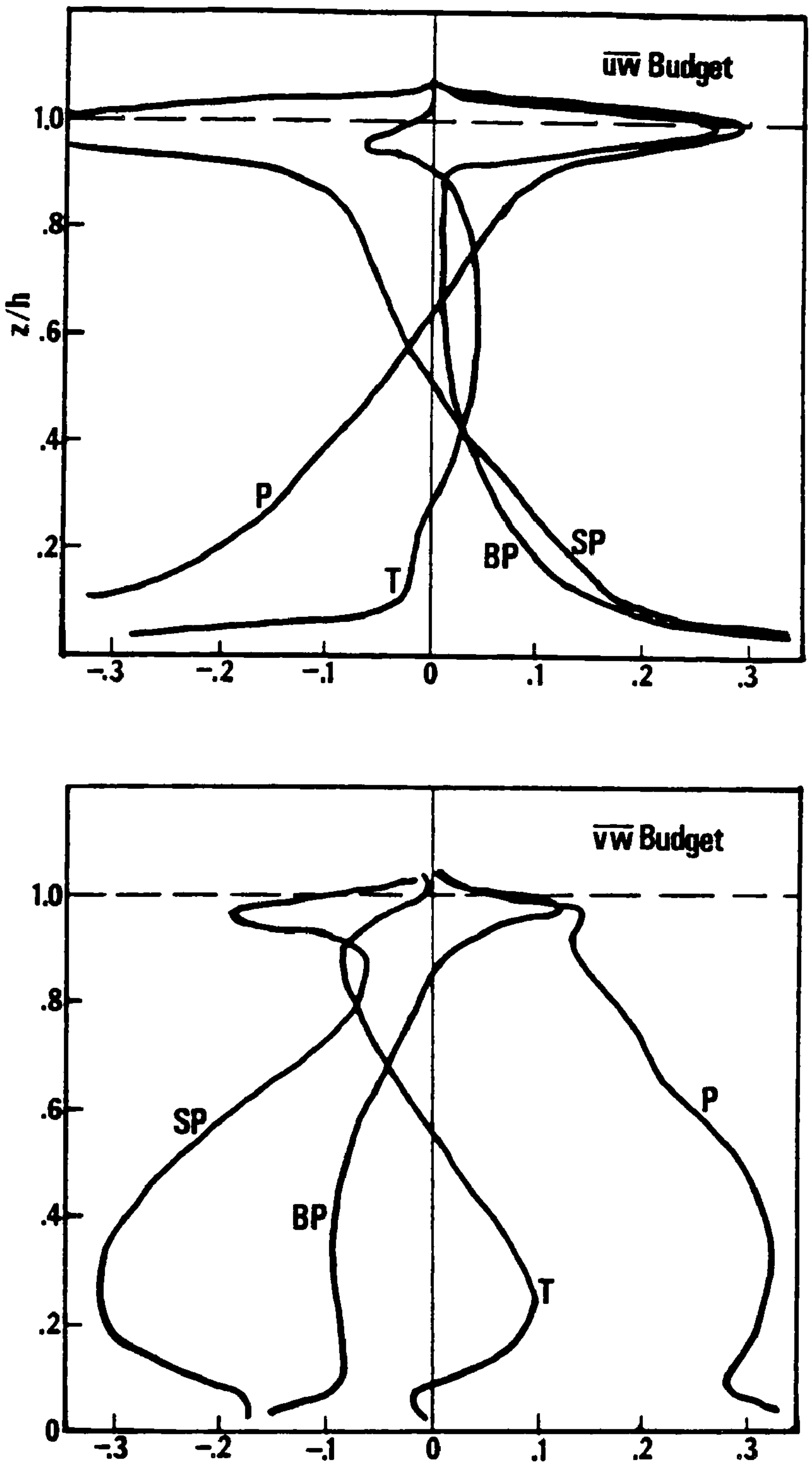

Fig. 57. Dimensionless stress budgets from numerical results for Volves experiment. Notation as in Fig. 55. (after Therry and Lacarrere, 1980.)

of these results would therefore appear to be in reasonable agreement with the radar VAD data.

Although available modeling and field data which address the horizontal momentum flux budget are rather sparse, the radar VAD statistics encompassed the results of existing data. The turbulent transport of horizontal momentum derived from the radar data however appear to be significantly larger than other data, especially the field data from Minnesota and AMTEX. The modeling work by Therry and Lacarrere (1980) indicate shear production and turbulent transport of the same order of magnitude, similar to the radar VAD results.

7. SUMMARY

A technique was developed to solve the turbulent momentum flux budget equation utilizing remote sensors. This was accomplished by theoretically extending the velocity azimuth display (VAD) technique to solve for third-moment turbulent velocity quantities from a single scanning Doppler radar. A primary motivation for this study was the lack of high resolution field data throughout the depth of the PBL, especially of higher-ordered statistics. The method outlined by Frisch (1990) of utilizing a least-squares fit to the radar radial velocity data was used in this study. This is viewed as an improvement over the method of Wilson (1970) which computes integrals for each quadrant of the VAD scan.

Three data sets were used as a test of this extended VAD technique. They were all characterized by hot, clear summertime convective boundary layers. Two of these cases were from the North Dakota Thunderstorm Project (NDTP) during the summer of 1989. The other case was from the Cloud Chemistry Cloud Physics Organization (3CPO) project during the summer of 1988.

Specific scanning strategies were used in order to improve the accuracy of derived statistics. The two data sets from NDTP used a four angle volume scan incorporating the elevation angles of 35.3°, 50.8°, 68.9° and 89.7°. The 35.3° scans were used to solve horizontal winds and associated statistics. Turbulence kinetic energy (TKE) can be obtained directly from the 35.3° scans and the vertical flux of TKE solved directly from the 50.8° sweeps (Frisch et. al. 1989). The 50.8° elevation is also used to solve for the horizontal momentum fluxes, $\overline{u'w'}$ and $\overline{v'w'}$. The turbulent transport of horizontal momentum flux, $\overline{u'w'^2}$ and $\overline{v'w'^2}$, requires data simultaneously from at least two elevation angles. The 68.9° were used in conjunction with the 50.8° sweeps for this purpose. The 89.7° scans were used for deriving accurate mean vertical velocities ($\bar{w}$)and associated vertical velocity statistics (e.g. $\overline{w'^2}$ and $\overline{w'^3}$).

The data set from 3CPO used a three angle volume scan identical to the four angle volume scan without the 68.9° scans. The only difference between the analysis is that the turbulent transport of the stresses is obtained from the 35.3° and 50.8° scans.

Data obtained during 1-2Jul89 from NDTP and was characterized by weakly baroclinic flow with modest warm advection into the region. A brief outflow from nearby convection was observed on this day as well as the development of a low-level nocturnal jet. Data were collected using the four angle volume scan continuously from 14:20 CDT 1Jul89 until 02:04 CDT 2Jul89. The 27-28Jun89 data set was slightly more baroclinic and contained the development of a nocturnal jet as well. Data collection was continuous from 16:24 CDT on 27Jun89 until 02:20 CDT on 28Jun89 using a four volume scan strategy. Data collection from 3CPO began at 10:14 CDT and ended at 16:54 CDT on 19Jun88 using continuous 3-angle VAD volume scans.

A large part of this research effort was devoted to the development of an appropriate VAD analysis program. The data were processed with this program and smoothed with a best-fit third-order polynomial curve using least-squares methods. From these processed data all terms in the momentum flux budget equations (2) and (3) were computed, excluding the buoyancy, pressure and eddy dissipation terms. These remaining terms were grouped together as a residual.

Based on a scale analysis of the momentum flux budgets (Wyngaard ,1983) the temporal changes in the stress, mean advection and shear production by $\bar{w}$ should be negligible. The radar supports this analysis for the temporal changes but the mean advection and shear production by $\bar{w}$ were not always negligible.

During the daytime and a convective outflow event on 1-2Jul89, values as large as 1.5×10^{-3} m^2s^{-3} were observed. During the night on 1-2Jul89 and for all of the other two data sets these terms were very small relative to other terms in the budget equations. Mean advection by $\bar{w}$ was a minor constituent in the vicinity of the nocturnal jet on 1-2Jul89.

The dominant terms in the momentum flux budgets from all three data sets derived from the radar VAD analysis were shear production and turbulent transport. Turbulent transport was the dominant term during the daytime during NDTP on 1-2Jul89. Shear production and turbulent transport were of the same order of magnitude during the daytime NDTP on 27-28Jun89 and 3CPO on 18Jun88. As the nocturnal boundary layer developed shear production became the dominant term in the momentum flux budget however turbulent transport was still significant.

The magnitudes of these radar derived turbulent momentum flux budget components were compared to other field data and modeling studies. With the few comparisons which were possible (due to the lack of existing data sets), the radar VAD data compared favorably. The shear production terms were within the range of values observed in other field data and modeling studies. Turbulent transport observed in the radar data were much larger than in the Minnesota or AMTEX data sets. Modeling results of the Voves experiment (Therry and Lacarrere, 1980) compared well with the radar data indicating shear production and turbulent transport terms of the same order of magnitude. Briere (1987) found magnitudes of turbulent transport within regions of a modeled sea-breeze circulation which were within the lower range of values observed by radar.

A number of factors could be responsible for the large values of the radar derived turbulent transport terms. Since neither the Minnesota, AMTEX or radar data sets were scaled, the specific meteorological conditions (eg. surface heat flux, etc.) could be a factor. Also the ground clutter in the radar data could induce artificially large values of turbulence statistics although this would be restricted to ranges nearest the clutter, not throughout the data. Insufficient measurement systems, considering some of these data sets were obtained nearly 20 years ago, could also be a factor. In support of the VAD measurements, Kropfli (1984) made comparisons of stress values computed using the VAD method with side by side X-band and K-band (0.8 mm) radars. The X-band measurements were also compared to a nearby instrumented tower. Both comparisons produced good results indicating the quality of the radar derived turbulence statistics. A similar study using the extended VAD technique presented in this study would be a valuable exercise in lieu of the small number of existing data sets.

Some important characteristics of atmospheric turbulence are illustrated by these radar measurements. These are primarily a result of the high temporal and spatial scales with which these radar data were obtained. A striking feature, which should not be unexpected, is the high degree of variability between averaging periods, especially in the vertical profiles of the momentum flux budget solutions. Turbulence is characterized by three- dimensional, random motions within a fluid and at any particular point is in a state of flux. The net budget of stress should balance over time, though there is no reason to expect the contribution of any given term to remain fixed at a given point in space. The radar data illustrate this point quite well. While the range in absolute magnitude of a given term was easily generalized over the depth of the PBL, the behavior at any given height within the PBL was typically quite variable. This has important consequences for the types of parameterizations derived for modeling studies which assume some general behavior in these profiles.

Another finding in this study is the significant contribution by turbulent transport term to the horizontal momentum flux budget. There were no situations in these data where turbulent transport was not of significant relative magnitude. In fact at times turbulent transport was the dominant term. Even during the nighttime when turbulent activity was greatly decreased this term was still a significant part of the momentum flux budget.

8. CONCLUSION

The extended Velocity Azimuth Display (VAD) technique presented in this study provides an important tool for study of the planetary boundary layer (PBL) using a single scanning Doppler radar. The resolution obtainable is better than most field methods and as good as numerical models. This theoretical extension of the VAD technique allows the solution of third-order turbulence statistics. Few studies to date have addressed the relative magnitude and importance of these higher-ordered statistics.

As a test of this extended VAD technique comparisons were made between solutions to the horizontal momentum flux budget computed using this extended VAD method (excluding buoyancy, pressure and eddy dissipation effects) and budgets obtained from other field and modeling studies. Shear production compared well between all data sets. The turbulent transport term from the VAD analysis was generally much greater relative to the other field and modeling data. While specific reasons for these differences were not clear, the results indicate that turbulent transport can be a significant and, at times, dominant term in the momentum flux budget.

It is important to obtain additional field data in order to understand the differences observed between the radar data sets and other existing field observations as they have significant consequences in the turbulent momentum flux budget. By using a radar with improved sensitivity and ground clutter rejection improvements in the uncertainty of the measurements obtained in this study can be made. Comparisons with *in situ* measurements, such as aircraft, would also prove valuable for determining relative errors between these different measurement systems. Used in conjunction with other supporting meteorological data (e.g. on-site surface data, supplemental soundings, temperature profiles, pressure measurements, etc.) this extended VAD technique could provide a nearly complete documentation of PBL turbulent processes.

REFERENCES

Andre, G. De Moor, P. Lacarrere, G. Therry and R. du Vachat, 1978: Modeling of the 24-Hour Evolution of the Mean and Turbulent Sturctures of the Planetary Boundary Layer, *J. Atmos. Sci.*, **35**, 1861-1883.

Briere, S., 1987: Energetics of Daytime Sea Breeze Circulation as Determined from a Two-Dimensional Third-Order Turbulence Closure Model, *J. Atmos. Sci.*, **44**, 1455-1474.

Browning, K.A. and R. Wexler, 1968: The Determination of Kinematic Properties of a Wind Field Using Doppler Radar, *J. Applied Meteor.*, **7**, 105-113.

Eberhard, W.L., R.E. Cupp and Kathleen Healy, 1989: Doppler Lidar Measurement of Profiles of Turbulence Momentum Flux, *J. Atmos. and Oceanic Technology*, Vol. **6**, No. 5, 809-819.

Frisch, A.S., 1990(in press): On the Measurement of Second Moments of Turbulent Wind Velocity with a Single Doppler Radar over non-Homogeneous Terrain, *Boundary-Layer Meteor.*

Frisch, A.S., B.E. Martner and J. Gibson, 1989: Measurement of the Vertical Flux of Turbulent Kinetic Energy with a Single Doppler Radar, *Boundary-Layer Meteor.*, **49**, 331-337.

Frisch, A.S. and T. Uttal, 1988: Single Doppler Radar Measurements of Planetary Boundary Layer Winds and Momentum Fluxes, *8th Symposium on Turbulence and Diffusion*, April 26-29, 1988, San Diego, Calif., Amer. Meteor. Soc., Boston, MA, pp. 172-175.

Frisch, A.S. and S.F. Clifford, 1974: A Study of Convection Capped by a Stable Layer Using Doppler Radar and Acoustic Echo Sounders, *J. Atmos. Sci.*, **31**, 1622-1628.

Holton, R.H., 1979: *An Introduction to Dynamic Meteorology*, Second Edition, Academic Press Inc., New York, New York.

Kaimal, J.C., J.C. Wyngaard, D.A. Haugen, O.R. Cote and Y. Izumi, 1976: Turbulence Structure in the Convective Boundary Layer, *J. Atmos. Sci.*, **33**, 2152-2169.

Kropfli, R.A., 1986: Single Doppler radar measurement of turbulence profiles in the convective boundary layer, *J. Atmos. and Oceanic Technology*, Vol. **3**, No. 2, 305-314.

Kropfli, R.A., 1984: Turbulence Measurements from Particulate Scatter in the Optically Clear Unstable Boundary Layer using Single Doppler Radar, *Proc. 22nd Conference on Radar Meteorology*, Sept. 10-13, Zurich, Switzerland, Amer. Meteor. Soc., Boston, MA, pp. 495-500.

Kropfli, R.A. and P.H. Hildebrand, 1980: Doppler Radar Measurements in the Planetary Boundary Layer during Phoenix, *Proc. 19th Conference on Radar Meteorology*, April 15-18, Miami, Fla., Amer. Meteor. Soc., Boston, MA, pp. 637-644.

Martner, B.E., A.S. Frisch and R.A. Kropfli, 1988: NOAA X- Band Radar Measurements in 3CPO, NOAA Tech. Memo. ERL WPL-153, NOAA\ERL\WPL, Boulder, CO, 58pp.

Stull, R.B., 1988: *An Introduction to Boundary Layer Meteorology*, Kluwer Academic Publishers, Dordrecht, The Netherlands, 666 pp.

Stull, R.B. and E.W. Eloranta, 1984: Boundary layer experiment - 1983. *Bull. Am. Meteor. Soc.*, **65**, 450-456.

Wilson, D.A., 1970: Doppler Radar Studies of Boundary Layer Wind Profile and Turbulence in Snow Conditions, *Proc. 14th Conference of Radar Meteorology*, Tuscon, AZ, Amer. Meteor. Soc., Boston, MA, pp. 191-196.

Wyngaard, J.C., 1983: The Mean Wind Structure of the Baroclinic Convective Boundary Layerl, Proc. First Sino-American Workshop on MOUNTAIN METEOROLOGY, Beijing, 18-23 May 1982, 371- 396.

APPENDIX A

This appendix contains the derivation of the momentum budget equations. First the general case is derived and then simplifications are presented. Parts of these derivations have been taken from Holton (1979) and Stull (1988).

Neglecting curvature terms the momentum equation in tensor notation is:

$$\frac{\partial u_i}{\partial t} + u_j \frac{\partial u_i}{\partial x_j} = -\delta_{i3} g - 2\varepsilon_{ijk}\Omega_j u_k - \frac{1}{\rho}\frac{\partial p}{\partial x_i} + \frac{1}{\rho}\frac{\partial \tau_{ij}}{\partial x_j} \qquad (10)$$

where the last term is the viscous dissipation term. For a Newtonian fluid:

$$\tau_{ij} = \mu\left(\frac{\partial u_i}{\partial x_j} + \frac{\partial u_j}{\partial x_i}\right) + \left(\mu_B - \frac{2}{3}\mu\right)\frac{\partial u_k}{\partial x_k}\delta_{ij}$$

Assuming μ_B is very small, dividing by ρ and differentiating with respect to x_j:

$$\frac{1}{\rho}\frac{\partial \tau_{ij}}{\partial x_j} = \frac{1}{\rho}\frac{\partial}{\partial x_j}\left[\mu\left(\frac{\partial u_i}{\partial x_j} + \frac{\partial u_j}{\partial x_i}\right) - \frac{2}{3}\mu\frac{\partial u_k}{\partial x_k}\delta_{ij}\right]$$

Rearranging differentiation order and assuming μ is independent of x, y and z:

$$\frac{1}{\rho}\frac{\partial \tau_{ij}}{\partial x_j} = \frac{\mu}{\rho}\left(\frac{\partial^2 u_i}{\partial {x_j}^2} + \frac{\partial}{\partial x_i}\frac{\partial u_j}{\partial x_j} - \frac{2}{3}\frac{\partial}{\partial x_i}\frac{\partial u_k}{\partial x_k}\right)$$

By assuming incompressibility and letting $\nu = \frac{\mu}{\rho}$, the above equation simplifies to:

$$\frac{1}{\rho}\frac{\partial \tau_{ij}}{\partial x_j} = \nu\frac{\partial^2 u_i}{\partial {x_j}^2}$$

Substituting this expression into (1) gives:

$$\frac{\partial u_i}{\partial t} + u_j \frac{\partial u_i}{\partial x_j} = -\delta_{i3} g - 2\varepsilon_{ijk}\Omega_j u_k - \frac{1}{\rho}\frac{\partial p}{\partial x_i} + \nu\frac{\partial^2 u_i}{\partial {x_j}^2} \qquad (11)$$

Making the Boussinesq approximation which neglects density perturbations except when multiplied by gravity, the substitutions $\rho = \bar{\rho}$ and g = g - $\left(\frac{\theta'_v}{\bar{\theta}_v}\right)$g can be made in (11). The coriolis term can be rewritten to give:

$$\frac{\partial u_i}{\partial t} + u_j \frac{\partial u_i}{\partial x_j} = -\delta_{i3}\left[g - \left(\frac{\theta'_v}{\bar{\theta}_v}\right)g\right] + f_c \varepsilon_{ij3} u_j - \frac{1}{\bar{\rho}}\frac{\partial p}{\partial x_i} + \nu \frac{\partial^2 u_i}{\partial {x_j}^2} \quad (12)$$

Writing the dependent variables (u and p) in terms of a mean and a perturbation from the mean ($u = \bar{u} + u'$ and $p = \bar{p} + p'$):

$$\frac{\partial(\bar{u}_i + u'_i)}{\partial t} + (\bar{u}_j + u'_j)\frac{\partial(\bar{u}_i + u'_i)}{\partial x_j} =$$

$$-\delta_{i3}\left[g - \left(\frac{\theta'_v}{\bar{\theta}_v}\right)g\right] + f_c \varepsilon_{ij3}(\bar{u}_j + u'_j)$$

$$- \frac{1}{\bar{\rho}}\frac{\partial(\bar{p} + p')}{\partial x_i} + \nu \frac{\partial^2(\bar{u}_i + u'_i)}{\partial {x_j}^2} \quad (13)$$

Expanding all terms produces an equation for the total wind:

$$\frac{\partial \bar{u}_i}{\partial t} + \frac{\partial u'_i}{\partial t} + \bar{u}_j \frac{\partial \bar{u}_i}{\partial x_j} + \bar{u}_j \frac{\partial u'_i}{\partial x_j} + u'_j \frac{\partial \bar{u}_i}{\partial x_j} + u'_j \frac{\partial u'_i}{\partial x_j} =$$

$$-\delta_{i3}\left[g - \left(\frac{\theta'_v}{\bar{\theta}_v}\right)g\right] + f_c \varepsilon_{ij3} \bar{u}_j + f_c \varepsilon_{ij3} u'_j$$

$$- \frac{1}{\bar{\rho}}\frac{\partial \bar{p}}{\partial x_i} - \frac{1}{\bar{\rho}}\frac{\partial p'}{\partial x_i} + \nu \frac{\partial^2 \bar{u}_i}{\partial {x_j}^2} + \nu \frac{\partial^2 u'_i}{\partial {x_j}^2} \quad (14)$$

After averaging this equation becomes:

$$\frac{\partial \bar{u}_i}{\partial t} + \bar{u}_j \frac{\partial \bar{u}_i}{\partial x_j} + \overline{u'_j \frac{\partial u'_i}{\partial x_j}} =$$

$$-\delta_{i3} g + f_c \varepsilon_{ij3} \bar{u}_j - \frac{1}{\bar{\rho}}\frac{\partial \bar{p}}{\partial x_i} + \nu \frac{\partial^2 \bar{u}_i}{\partial {x_j}^2} \quad (15)$$

The continuity equation for turbulent fluxes is $\left(\frac{\partial u'_j}{\partial x_j}\right) = 0$. Multiplying this by u'_i, averaging and adding the result to equation (15) to put the last term on the left hand side into flux form results in an equation for the mean wind:

$$\frac{\partial \bar{u}_i}{\partial t} + \bar{u}_j\frac{\partial \bar{u}_i}{\partial x_j} = -\delta_{i3}g + f_c\varepsilon_{ij3}\bar{u}_j - \frac{1}{\bar{\rho}}\frac{\partial \bar{p}}{\partial x_i} + \nu\frac{\partial^2 \bar{u}_i}{\partial {x_j}^2} - \frac{\partial(\overline{u'_i u'_j})}{\partial x_j} \tag{16}$$

Subtracting (16) from (14) yields a prognostic equation for the turbulent gust:

$$\frac{\partial u'_i}{\partial t} + \bar{u}_j\frac{\partial u'_i}{\partial x_j} + u'_j\frac{\partial \bar{u}_i}{\partial x_j} + u'_j\frac{\partial u'_i}{\partial x_j} = \delta_{i3}\left(\frac{\theta'_v}{\bar{\theta}_v}\right)g + f_c\varepsilon_{ij3}u'_j - \frac{1}{\bar{\rho}}\frac{\partial p'}{\partial x_i} + \nu\frac{\partial^2 u'_i}{\partial {x_j}^2} + \frac{\partial(u'_i u'_j)}{\partial x_j} \tag{17}$$

Multiplying the above equation by u'_k and Reynolds averaging gives:

$$\overline{u'_k\frac{\partial u'_i}{\partial t}} + \overline{u'_k\bar{u}_j\frac{\partial u'_i}{\partial x_j}} + \overline{u'_k u'_j\frac{\partial \bar{u}_i}{\partial x_j}} + \overline{u'_k u'_j\frac{\partial u'_i}{\partial x_j}} = \overline{u'_k\delta_{i3}\left(\frac{\theta'_v}{\bar{\theta}_v}\right)g} + f_c\varepsilon_{ij3}\overline{u'_j u'_k} - \overline{\frac{u'_k}{\bar{\rho}}\frac{\partial p'}{\partial x_i}} + \overline{u'_k\nu\frac{\partial^2 u'_i}{\partial {x_j}^2}} + \overline{u'_k\frac{\partial(u'_i u'_j)}{\partial x_j}} \tag{18}$$

Equation (18) can be rewritten interchanging all i's and k's.

$$\overline{u'_i\frac{\partial u'_k}{\partial t}} + \overline{u'_i\bar{u}_j\frac{\partial u'_k}{\partial x_j}} + \overline{u'_i u'_j\frac{\partial \bar{u}_k}{\partial x_j}} + \overline{u'_i u'_j\frac{\partial u'_k}{\partial x_j}} = \overline{u'_i\delta_{k3}\left(\frac{\theta'_v}{\bar{\theta}_v}\right)g} + f_c\varepsilon_{kj3}\overline{u'_j u'_i} - \overline{\frac{u'_i}{\bar{\rho}}\frac{\partial p'}{\partial x_k}} + \overline{u'_i\nu\frac{\partial^2 u'_k}{\partial {x_j}^2}} + \overline{u'_i\frac{\partial(u'_k u'_j)}{\partial x_j}} \tag{19}$$

Adding (18) and (19):

$$\frac{\partial(\overline{u'_i u'_k})}{\partial t} + \bar{u}_j\frac{\partial(\overline{u'_i u'_k})}{\partial x_j} + \overline{u'_k u'_j}\frac{\partial \bar{u}_i}{\partial x_j} + \overline{u'_i u'_j}\frac{\partial \bar{u}_k}{\partial x_j} + \overline{u'_j\frac{\partial(u'_i u'_k)}{\partial x_j}} = \overline{\delta_{k3}u'_i\left(\frac{\theta'_v}{\bar{\theta}_v}\right)g} + \overline{\delta_{i3}u'_k\left(\frac{\theta'_v}{\bar{\theta}_v}\right)g} + f_c\varepsilon_{kj3}\overline{u'_j u'_i} + f_c\varepsilon_{ij3}\overline{u'_j u'_k} - \overline{\frac{u'_i}{\bar{\rho}}\frac{\partial p'}{\partial x_k}} - \overline{\frac{u'_k}{\bar{\rho}}\frac{\partial p'}{\partial x_i}} + \overline{\nu u'_i\frac{\partial^2 u'_k}{\partial {x_j}^2}} + \overline{\nu u'_k\frac{\partial^2 u'_i}{\partial {x_j}^2}} \tag{20}$$

where the last term in (18) and (19) has been neglected relative to the other terms.

Further simplifications can be made to equation (20). Taking $u'_i u'_k$ times the turbulent continuity equation $\left(\frac{\partial u'_j}{\partial x_j}\right) = 0$, averaging the result and adding it to (20) allows the last term on the left-hand side of (20) to be put into flux form. Applying the product rule to the viscosity terms we get:

$$\overline{u'_i \frac{\partial^2 u'_k}{\partial x_j{}^2}} + \overline{u'_k \frac{\partial^2 u'_i}{\partial x_j{}^2}} = \frac{\partial^2(\overline{u'_i u'_k})}{\partial x_j{}^2} - 2\overline{\frac{\partial u'_i \partial u'_k}{\partial x_j{}^2}}$$

Substituting these changes into (20) gives a form for the momentum flux budget:

$$\begin{aligned} \frac{\partial(\overline{u'_i u'_k})}{\partial t} + \bar{u}_j \frac{\partial(\overline{u'_i u'_k})}{\partial x_j} &= -\overline{u'_i u'_j}\frac{\partial \bar{u}_k}{\partial x_j} - \overline{u'_k u'_j}\frac{\partial \bar{u}_i}{\partial x_j} - \frac{\partial(\overline{u'_i u'_j u'_k})}{\partial x_j} \\ &+ \left[\frac{g}{\bar{\theta}_v}\right]\left(\delta_{k3}\overline{u'_i\theta'_v} + \delta_{i3}\overline{u'_k\theta'_v}\right) + f_c\left(\varepsilon_{kj3}\overline{u'_i u'_j} + \varepsilon_{ij3}\overline{u'_j u'_k}\right) \\ &- \overline{\frac{u'_i}{\bar{\rho}}\frac{\partial p'}{\partial x_k}} - \overline{\frac{u'_k}{\bar{\rho}}\frac{\partial p'}{\partial x_i}} + \nu\frac{\partial^2(\overline{u'_i u'_k})}{\partial x_j{}^2} - 2\nu\overline{\frac{\partial u'_i \partial u'_k}{\partial x_j{}^2}} \end{aligned} \tag{21}$$

Typically the coriolis terms and the molecular diffusion term are smaller than the rest and can be neglected. The viscous dissipation term is often written as $2\varepsilon_{u_i u_k}$ to give the final form of the momentum flux budget as:

$$\begin{aligned} \frac{\partial(\overline{u'_i u'_k})}{\partial t} + \bar{u}_j \frac{\partial(\overline{u'_i u'_k})}{\partial x_j} &= -\overline{u'_i u'_j}\frac{\partial \bar{u}_k}{\partial x_j} - \overline{u'_k u'_j}\frac{\partial \bar{u}_i}{\partial x_j} - \frac{\partial(\overline{u'_i u'_j u'_k})}{\partial x_j} \\ &+ \left[\frac{g}{\bar{\theta}_v}\right]\left(\delta_{k3}\overline{u'_i\theta'_v} + \delta_{i3}\overline{u'_k\theta'_v}\right) - \overline{\frac{u'_i}{\bar{\rho}}\frac{\partial p'}{\partial x_k}} - \overline{\frac{u'_k}{\bar{\rho}}\frac{\partial p'}{\partial x_i}} - 2\varepsilon_{u_i u_k} \end{aligned} \tag{22}$$

The equations for $\overline{u'w'}$ (i=1, k=3) and $\overline{v'w'}$ (i=2, k=3) from (22) are:

$$\begin{aligned} &\frac{\partial \overline{u'w'}}{\partial t} + \bar{u}\frac{\partial \overline{u'w'}}{\partial x} + \bar{v}\frac{\partial \overline{u'w'}}{\partial y} + \bar{w}\frac{\partial \overline{u'w'}}{\partial z} = \\ &- \overline{u'u'}\frac{\partial \bar{w}}{\partial x} - \overline{u'v'}\frac{\partial \bar{w}}{\partial y} - \overline{u'w'}\frac{\partial \bar{w}}{\partial z} - \overline{w'u'}\frac{\partial \bar{u}}{\partial x} - \overline{w'v'}\frac{\partial \bar{u}}{\partial y} - \overline{w'w'}\frac{\partial \bar{u}}{\partial z} \\ &- \frac{\partial(\overline{u'u'w'})}{\partial x} - \frac{\partial(\overline{u'v'w'})}{\partial y} - \frac{\partial(\overline{u'w'w'})}{\partial z} \\ &+ \left[\frac{g}{\bar{\theta}_v}\right](\overline{u'\theta'_v}) - \overline{\frac{u'}{\bar{\rho}}\frac{\partial p'}{\partial z}} - \overline{\frac{w'}{\bar{\rho}}\frac{\partial p'}{\partial x}} - 2\varepsilon_{uw} \end{aligned} \tag{23}$$

$$\frac{\partial\overline{v'w'}}{\partial t} + \bar{u}\frac{\partial\overline{v'w'}}{\partial x} + \bar{v}\frac{\partial\overline{v'w'}}{\partial y} + \bar{w}\frac{\partial\overline{v'w'}}{\partial z} =$$

$$- \overline{v'u'}\frac{\partial\bar{w}}{\partial x} - \overline{v'v'}\frac{\partial\bar{w}}{\partial y} - \overline{v'w'}\frac{\partial\bar{w}}{\partial z} - \overline{w'u'}\frac{\partial\bar{v}}{\partial x} - \overline{w'v'}\frac{\partial\bar{v}}{\partial y} - \overline{w'w'}\frac{\partial\bar{v}}{\partial z}$$

$$- \frac{\partial(\overline{v'u'w'})}{\partial x} - \frac{\partial(\overline{v'v'w'})}{\partial y} - \frac{\partial(\overline{v'w'w'})}{\partial z}$$

$$+ \left[\frac{g}{\bar{\theta}_v}\right](\overline{v'\theta'_v}) - \overline{\frac{v'}{\bar{\rho}}\frac{\partial p'}{\partial z}} - \overline{\frac{w'}{\bar{\rho}}\frac{\partial p'}{\partial y}} - 2\varepsilon_{vw} \qquad (24)$$

Many of these terms can be neglected based on a scale analysis using observations of these quantities or by making appropriate assumptions. Neglecting subsidence and assuming horizontal homogeneity are common steps in simplifying these equations. With the scanning procedures used in collecting the data used for this study the subsidence can easily be determined and will therefore be left in the equations in order to test this assumption. Also with appropriate scanning procedures the horizontal gradients of the fluxes can be estimated (Frish,1990) however this will not be addressed in this study. By assuming horizontal homogeneity equations (24) and (25) are:

$$\frac{\partial\overline{u'w'}}{\partial t} + \bar{w}\frac{\partial\overline{u'w'}}{\partial z} = - \overline{u'w'}\frac{\partial\bar{w}}{\partial z} - \overline{w'w'}\frac{\partial\bar{u}}{\partial z} - \frac{\partial(\overline{u'w'w'})}{\partial z}$$

$$+ \left[\frac{g}{\bar{\theta}_v}\right](\overline{u'\theta'_v}) - \overline{\frac{u'}{\bar{\rho}}\frac{\partial p'}{\partial z}} - 2\varepsilon_{uw} \qquad (25)$$

$$\frac{\partial\overline{v'w'}}{\partial t} + \bar{w}\frac{\partial\overline{v'w'}}{\partial z} = - \overline{v'w'}\frac{\partial\bar{w}}{\partial z} - \overline{w'w'}\frac{\partial\bar{v}}{\partial z} - \frac{\partial(\overline{v'w'w'})}{\partial z}$$

$$+ \left[\frac{g}{\bar{\theta}_v}\right](\overline{v'\theta'_v}) - \overline{\frac{v'}{\bar{\rho}}\frac{\partial p'}{\partial z}} - 2\varepsilon_{vw} \qquad (26)$$